Mechanistic and statistical models to understand CXCL12/CXCR4/CXCR7 in breast cancer

By

Sei-Won Laura Chang

A dissertation submitted in partial fulfillment
of the requirements for the degree of
Doctor of Philosophy
(Chemical Engineering)
in the University of Michigan
2015

Doctoral Committee:

Professor Jennifer J. Linderman, Chair
Associate Professor Lola Eniola-Adefeso
Associate Professor Gary D. Luker
Assistant Professor Sunitha Nagrath

Acknowledgements

I am incredibly grateful to have the support of numerous smart and caring mentors. To my advisor, Jennifer Linderman, thank you for teaching me how to assess problems, think critically, and argue wisely. Jennifer is a phenomenal motivator and her ability to push students beyond where they think they can go is just one reason why she is such a great advisor.

To Gary Luker, my co-mentor in every way except in the official paperwork, thank you for letting me join the Luker lab family. Collaborating with Gary has spoiled me for all future collaborations – he is incredibly kind, accessible and always willing to lend an ear.

Thanks to my committee members Lola Eniola-Adefeso and Sunitha Nagrath for all of your helpful insight. Lola taught me undergraduate heat and mass transfer, my favorite class, which brought me along this path of research. Sunitha, thank you for letting me join your group meetings at the beginning of my PhD, when I knew nothing about cancer biology and was desperately trying to learn.

Many thanks to Kathy Luker for always being willing to teach me new things. Kathy is incredibly generous and creative, both in and out of the laboratory. Her ability to describe complex concepts in a way that anyone can understand is second to none. Thanks to Shu Takayama, your sharp insight has been invaluable to the direction of my work. To Steve Cavnar, we shared high school chemistry, undergraduate ChE, and now our doctorates. Thank you for all of your support and help. To the rest of the Luker lab, thank you for welcoming me into your lab. Please let me come back for another round of Luker Lab Olympics.

Thanks to my fellow labmembers: To my academic brothers, Mohammad Fallahi-Sichani and Nicholas Cilfone, for your patience and setting the bar high; to Danielle Trakimas, Elsje Pienaar and Cordelia Ziraldo, for always being available to help and for your friendship. Thanks also to Denise Kirschner, Paul Wolberg, Simeone Marino, Fred Gong, Hayley Warsinski, Madhuresh Sumit, Phil Spinosa, and Amy Oberlin.

To Joerg Lahann, my first research mentor, thank you for encouraging me to go to graduate school and giving me so many great opportunities. Thanks to Mark Burns, for your enthusiastic support of all of the outreach and departmental activities that I helped plan. Thanks to Susan Hamlin, who has been incredibly helpful for so many things related to graduate student life.

I feel extremely fortunate to have a close group of peers that started our PhDs together. Thanks to all of you, especially Youngri Kim and Sahar Rahmani.

To my family, Mom, Dad, Grandma, Leigha, James, aunts and uncles, and my in-laws, Rose and Rong: thank you for feeding me, listening to me, and for your unending support. Lastly, to my husband, George, I could never have predicted that we would end up working in such similar areas. Everything is more fun when we're together.

Table of Contents

List of Tables

List of Figures

Chapter 1 Introduction

1.1 Motivation

The distinguishing characteristic between malignant and benign tumors is the ability to invade and metastasize. This hallmark of cancer appropriates chemotaxis, cell migration in response to chemokine gradients, to direct cancer cells to specific sites. In this thesis, we focus on the most highly chemotactic proponent in cancer, the CXCL12/CXCR4 signaling axis. In this work, we construct mechanistic and statistical models to better understand how to target this pathway in breast cancer.

1.2 The CXCL12/CXCR4/CXCR7 pathway in cancer

1.2.1 CXCL12/CXCR4: a strong proponent of metastasis

The CXCL12/CXCR4 pathway is perhaps the best example of how chemokine signaling has been co-opted by cancer. CXCR4 is a seven-transmembrane G-protein coupled receptor (GPCR) that is constitutively expressed on cells of the immune and central nervous systems, including hematopoietic progenitor cells, neutrophils, B cells, naïve T cells, microglia and neurons [1-5]. All of these cells migrate in gradients of CXCL12, the only known ligand for CXCR4. More than 75% of all cancers, including breast, prostate, and brain, exhibit CXCR4 overexpression, whereas the receptor is typically low or absent in normal tissue [6]. High CXCR4 gene expression in primary tumors is correlated with metastasis and worse survival outcomes in numerous cancer types [7-15]. CXCR4 is also a cancer stem cell marker, suggesting that blocking CXCR4 activity may be one strategy to target cancer subpopulations refractory to treatment [16-20]. Not only is CXCR4 upregulated on cancer cells of primary tumors, but CXCR4 is also expressed on cancer cells in metastatic lesions [21]. CXCL12 is constitutively expressed in organs of first metastasis; such as the lung, liver, and bone; suggesting that cancer cells hijack

chemotaxis mechanisms for more efficient invasion, migration and dissemination of cancer [20-26].

In Chapters 2 and 3, we use statistical and mechanistic models to understand how CXCL12 can play a role in the tumor environment. Tumor stroma produce chemokines and other factors that support growth, proliferation, and alteration of cancer cells [27-29]. In breast cancer, carcinoma-associated fibroblasts have been shown to produce CXCL12, whereas the expression is absent in fibroblasts of normal breast tissue [22]. As a result, CXCL12 gradients produced by tumor stroma can stimulate tumor angiogenesis by recruiting circulating endothelial progenitor cells to the primary site and may promote directional movement of cancer cells towards blood vessels or the invasive tumor edge [24]. Although CXCL12 is often discussed as a single protein, the CXCL12 gene undergoes alternative splicing to produce six distinct CXCL12 isoforms: α, β, γ, δ, ε, ϕ [30]. Recent studies suggest that CXCL12 isoforms can have different outcomes in experimental assays of cell migration [31-33]. In Chapter 2, we investigate the expression of CXCL12 isoforms to clinical and molecular staging parameters, as well as patient survival outcomes. In Chapter 3, we model CXCL12 isoforms using a mechanistic approach to study how their molecular properties affect gradient formation and cell responses.

1.2.2 Role of CXCR7

Until 2005, CXCR4 was the only known receptor for CXCL12. Since then, it has been established that the atypical chemokine receptor, CXCR7 (also known as ACKR3), can also bind to and signal via CXCL12 [34]. CXCR7 is a seven-transmembrane receptor that is unable to signal through G proteins. Instead, CXCR7 primarily signals via β-arrestin1/2 [35, 36]. Due to its high affinity for CXCL12, CXCR7 plays a large role in internalizing and degrading extracellular CXCL12 [35].

CXCR7 is associated with malignancy in cancer. Although not expressed on normal breast epithelia or vasculature, CXCR7 is expressed on malignant cells of about 30% of primary breast tumors and is highly expressed on tumor-associated vasculature of nearly all breast tumors [37, 38]. Independent of CXCR4 expression, the presence of CXCR7+

cancer cells has been shown to promote tumor growth and metastasis in breast and lung cancers [38]. In vitro and in vivo studies demonstrate an enhancement of CXCR4 chemotaxis when CXCR7 levels are elevated [32, 37, 39]. This may be in part due to role CXCR7 plays in reducing CXCL12 levels in extracellular space [37]. These data suggest that by scavenging CXCL12, CXCR7+ cells may enhance the chemotaxis of CXCR4+ cells by creating gradients directing migration out of the tumor and/or by maintaining CXCL12 concentrations below receptor saturation levels. How might CXCR7 affect CXCL12/CXCR4 signaling? We take two approaches to look at this. In Chapter 3, we model CXCR7 as a scavenger of extracellular ligand and demonstrate how it can shift responses in cells only expressing the CXCR4 receptor. In Chapter 4, we probe how co-expression of CXCR7 with CXCR4 may alter CXCR4 signaling. Both chapters aim to understand how these two receptors should be targeted to mitigate malignant CXCL12/CXCR4 signaling.

1.2.3 Signaling

Upon binding CXCL12, CXCR4 can trigger a number of intracellular signaling pathways with diverse cellular responses. Via Gαi, CXCL12 binding to CXCR4 results in calcium flux, cAMP inhibition, and activation of the AKT, MAPK, and PI3K pathways [23, 40]. Independently of G proteins, CXCR4 can also signal by forming a complex with β-arrestin1/2. Traditionally, β-arrestin1/2 has been thought to serve primarily as a desensitizer to GPCR signaling; however, it is now accepted that association with β-arrestin1/2 results in signaling beyond internalization and trafficking [41]. Via β-arrestin1/2, CXCR4 scaffolds with MEK to promote ERK activation [23, 42-44]. In addition to its scavenging ability, CXCR7 can also signal through β-arrestin1/2. CXCR7 signaling via β-arrestin1/2 can elicit Akt, MAPK, and JAK/STAT3 pathways, although whether this is by direct modification or by heterodimerization with CXCR4 is unclear [45, 46].

1.2.4 Targeting CXCR4/CXCR7

Several compounds have been developed to target CXCL12/CXCR4 signaling. A CXCR4 antagonist, AMD3100 (also called Plerixafor or Mozobil), is FDA-approved to mobilize hematopoetic stem cells for collection and autologous stem cell transplantation

in patients with non-Hodgkins lymphoma and multiple myeloma [47-55]. Currently, AMD3100 is only approved for short-term use, but has recently been shown to be safe at low-doses for at least six months to alleviate panleukopenia in WHIM syndrome [50, 56]. In acute myeloid leukemia (AML), immature white blood cells (blasts) occupy the bone marrow and interrupt the production of normal blood cells. It is thought that the CXCL12-rich bone marrow microenvironment provides a protective effect to the AML blasts. A Phase 1 and 2 clinical trial demonstrated that after mobilization, AML blasts collected from the blood display increased surface CXCR4 [49].

For cancers with solid tumors, the benefits of blocking CXCL12/CXCR4 signaling have been mixed. Some CXCR4 drugs have been shown to impede tumor growth, whereas others are not as effective [57-61]. CTCE-9908, the CXCL12 analog approved for osteosarcoma, has been shown to prevent metastasis in prostate and breast cancers in mouse models [62, 63], but has not yet been tested in humans.

One potential targeting strategy is to inhibit CXCR7 function in conjunction with CXCR4. AMD3100 is not a potential candidate for such duel inhibition, as it is an allosteric agonist of CXCR7 at pharmacologic levels [64]. Efforts to develop CXCR7-specific agents are currently underway [45, 65]. The CXCR7 antagonist CCX771 has been used to demonstrate the role of CXCR7 in cancer. CCX771 blocks human brain microvascular endothelial cell migration and inhibits transendothelial migration of CXCR4+ cells in CXCL12 gradients in mouse models [45, 66].

1.2.5 CXCL12 isoforms and glycosaminoglycans

In vivo chemokine gradients are influenced by the presence of negatively-charged glycosaminoglycan (GAG) groups, such as heparin sulfates, that reside on cell surfaces and the extracellular matrix. GAG interaction can restrain chemokines on cell surfaces and may influence gradient formation [67]. GAGs may also facilitate the receptor binding process by increasing local chemokine availability [68]. The six CXCL12 isoforms differ in the number of BBXB domains, which are positively charged, resulting in differences in affinity to GAGs due to the negative-positive charge interaction [31, 69]. However, most experimental studies demonstrating the role of CXCL12 in cancer and chemotaxis

focus on the α isoform or do not discriminate between isoforms [30]. CXCL12 isoforms have physiological differences in tissue expression, and may also differ in tumor-specific expression [30, 70]. In Chapter 2, we present the first study examining the expression of all six CXCL12 isoforms breast cancer.

1.2.6 Receptor organization on the plasma membrane

During chemotaxis, cells appear to distribute their receptors asymmetrically across their length to maximize gradient sensing [71]. Spatial reorganization of receptors and other cell membrane-bound molecules may be used to amplify signaling in other cellular processes. Macropinocytosis, a process where the cell membrane folds over itself to entrap and ingest extracellular fluid, is highly dependent on the organization of the cellular membrane [72, 73]. In Chapter 5, we use 3D modeling tools to understand how diffusion on the cell membrane is restricted during macropinocytosis.

1.3 Methods

1.3.1 Gene expression profiling techniques

Gene expression profiling techniques allow us to extract correlations between CXCL12/CXCR4/CXCR7 gene level expression and patient outcomes. The rapid cost decrease of whole genome sequencing has produced an enormous amount of data to mine. In fact, not only are there thousands of publicly available datasets, but several websites that collect and allow facile search of this massive amount of data [74-76]. Microarray technology is the most common method of profiling gene expression. A DNA microarray organizes probes to specific DNA sequences on a solid surface (either chip or microscopic beads). The current standard microarray can probe for nearly 40,000 genes. These microarrays rely on the a priori knowledge of DNA sequence to develop the probes of the array. Therefore, current microarrays are not specific enough to detect small differences between proteins, such as the CXCL12 isoforms. RNAseq, a next-generation sequence method, alleviates this issue (Figure 1.2). Instead of relying on probes, RNAseq relies on a digital method to determine gene expression levels. In RNAseq, cDNA (converted by reverse transcriptase of patient mRNA) is digested into small pieces, or RNAseq “reads”. An algorithm aligns the reads to the genome, and the number of reads

specific to a particular isoform are counted to determine relative abundance of one isoform to another [77].

1.3.2 In silico models of cancer

Increasingly, mathematical and computational models are used to untangle the complex behaviors of biological systems. The major types of models for cancer can be classified as continuous models and discrete models. Continuous models use ordinary and partial differential equations (ODEs and PDEs, respectively) to describe the changes in cell density or tumor invasion [78-81]. These deterministic models tend to describe the tumor as a continuous medium and predict cell population dynamics without an emphasis on the underlying mechanisms [82, 83]. On the other hand, agent-based models (ABM) are discrete models where the biological system is described as a collection of individual agents in an environment. Typically, the agents in these models are the cells in the system, which reside on a lattice environment. Cell interactions with other cells and their environment are governed by a set of rules. Commonly, ABMs incorporate stochasticity by implementing probabilities for these interactions. ABMs focus on determining the effect of these individual interactions on the emergent behavior of the system [84, 85].

1.3.3 Multi-scale models

We and others have constructed hybrid ABMs that combine the advantages of both continuous and discrete models in order to provide a mechanistic examination of processes occurring at multiple biological scales [83, 86-97]. In these multi-scale models, cellular behavior is typically modeled in an ABM framework and ODE/PDEs describe molecular processes. For example, on the tissue scale, cells may be able to move, grow, proliferate, change states and die. Each cell on the lattice can have a set of ODEs describing intracellular signaling pathways. When cells secrete or internalize chemokines and other molecules on the lattice, PDEs are used to calculate molecular diffusion and update the levels of molecules at each lattice space. These models have been successfully used to investigate the role of molecular scale processes on the overall dynamics of the tissue scale.

Most ABMs that include the role of chemotaxis for cellular migration base the direction of movement solely on the chemokine concentrations in the neighborhood, without any information about receptor dynamics [94, 98, 99]. Furthermore, many hybrid ABMs that do incorporate intracellular signaling pathways for chemotaxis do not incorporate the role of receptor dynamics. Yet, receptor desensitization is universal among chemokine receptors and required for cells to chemotax [100].

1.3.4 Uncertainty and sensitivity analysis

In mathematical and computational models of biological systems, parameter values are often estimated from experiments under different conditions, extrapolated from literature and/or fit to the model itself. Due to this uncertainty in the accuracy of the inputs, uncertainty and sensitivity analyses (U/SA) are crucial to the examination of complex models. Uncertainty analysis explores the uncertainty in the model derived from the uncertainty in parameter inputs. Sensitivity analysis investigates the contribution of each individual parameter to the uncertainty of the model results [101, 102]. Several approaches have been developed to perform U/SA. Of particular interest is Latin hypercube sampling (LHS) coupled with partial rank correlation coefficients (PRCC), which has been used to carry out U/SA in both deterministic and stochastic models [80, 88, 103].

LHS is a popular sampling technique because it can provide a large amount of uncertainty data with a relatively small sample size and is greater than one order of magnitude more efficient than random sampling methods [101, 103]. Rather than varying one parameter at a time, in LHS, all parameters are varied simultaneously, providing an unbiased examination of each parameter, regardless of which might turn out to be most important. LHS is a stratified non-replacement sampling strategy where each parameter range is divided into N equal probability intervals. Each probability interval is sampled only once and is repeated for each parameter. Simulations are then run using M combinations of parameter values and produces M model outputs [101-103]. PRCC can then be calculated to determine how well the variability of a parameter correlates to a selected model output. PRCC values are between -1 and 1, which are associated with a

perfectly negative or perfectly positive correlation between the parameter and model outcome.

1.4 Thesis summary

In this thesis, we focus on multiple scales of biology. In Chapter 2, we correlate CXCL12 isoform gene expression levels to patient population outcomes. In Chapter 3, we link the molecular scale to the tissue scale to explain how events such as ligand-receptor binding and internalization shape gradients and affect cell movement within tumors. In Chapter 4, we model CXCR4/CXCR7 signaling in more depth to understand how targeting CXCR7 in the context of mitigating CXCR4 signaling may result in unintended effects. In Chapter 5, we construct a 3D model of macropinocytosis to understand how plasma membrane bound molecules reorganize during such complex events.

1.5 Figures

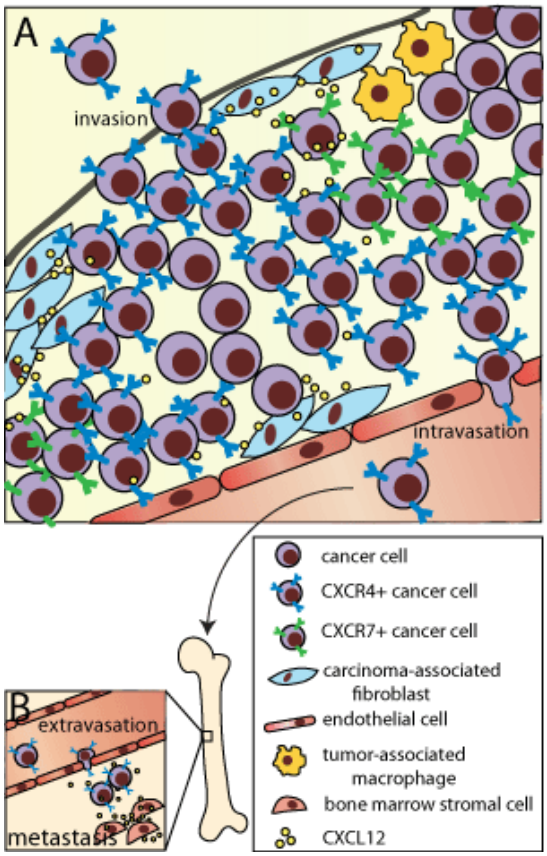

Figure 1.1 Effects of CXCL12 gradients on cancer progression.

(A) The primary breast tumor microenvironment. CXCR4+ and CXCR7+ cancer cells may respond to gradients of CXCL12 produced by carcinoma-associated fibroblasts. (B) Distant metastatic site. CXCL12 gradients produced by bone marrow stromal cells can provide a homing mechanism for cancer cells to metastasize.

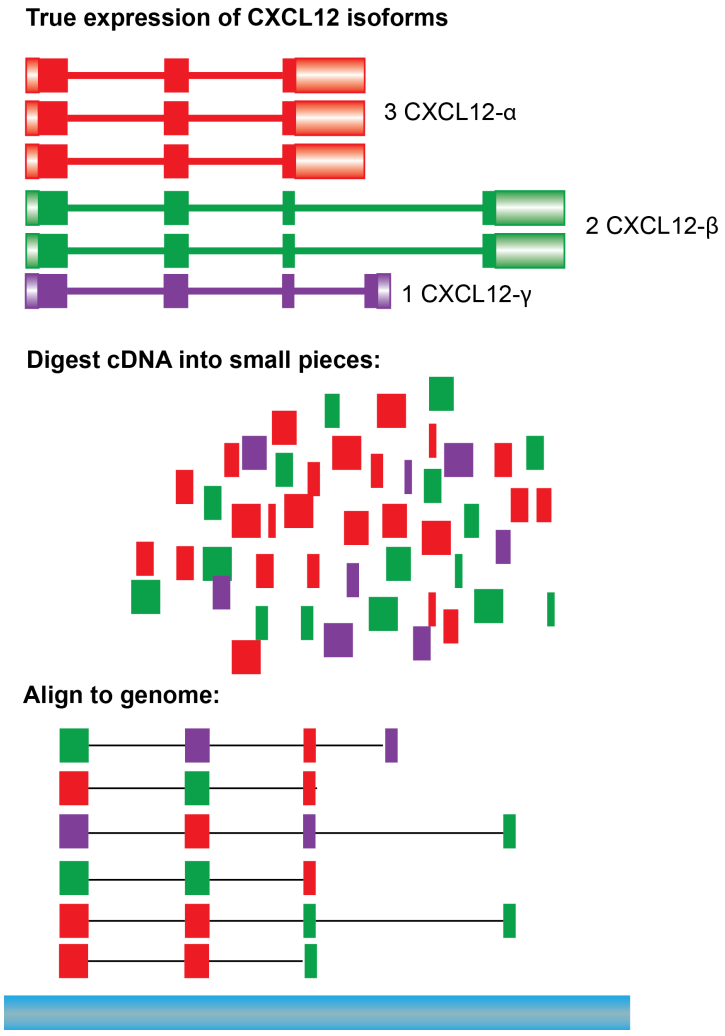

Figure 1.2 Algorithm for calculating relative gene expression in RNAseq

Contrary to microarrays, probing gene expression using RNAseq is not dependent on the a priori creation of probes specific to genes of interest. Instead, the RNAseq algorithm accepts randomly spliced parts of the patient's genome, and aligns it to a map of the genome. Then, the algorithm counts regions specific to each protein of interest. In the case of CXCL12 isoforms, the C-terminus of CXCL12-β and -γ are unique to those isoforms, however the exon closest to the N-terminus is not. Therefore, RNAseq would count the total number of unique regions of CXCL12-β and -γ, and then deduce that the remaining counts of the shared exon is correlated to the expression of CXCL12-α.

1.6 References

1. Aiuti A, Webb IJ, Bleul C, Springer T, Gutierrez-Ramos JC. The chemokine SDF-1 is a chemoattractant for human CD34+ hematopoietic progenitor cells and provides a new mechanism to explain the mobilization of CD34+ progenitors to peripheral blood. The Journal of experimental medicine. 1997;185(1):111-20. Epub 1997/01/06. PubMed PMID: 8996247; PubMed Central PMCID: PMC2196104.
2. Forster R, Kremmer E, Schubel A, Breitfeld D, Kleinschmidt A, Nerl C, et al. Intracellular and surface expression of the HIV-1 coreceptor CXCR4/fusin on various leukocyte subsets: rapid internalization and recycling upon activation. J Immunol. 1998;160(3):1522-31. Epub 1998/05/07. PubMed PMID: 9570576.
3. Tanabe S, Heesen M, Yoshizawa I, Berman MA, Luo Y, Bleul CC, et al. Functional expression of the CXC-chemokine receptor-4/fusin on mouse microglial cells and astrocytes. J Immunol. 1997;159(2):905-11. Epub 1997/07/15. PubMed PMID: 9218610.
4. Lavi E, Strizki JM, Ulrich AM, Zhang W, Fu L, Wang Q, et al. CXCR-4 (Fusin), a co-receptor for the type 1 human immunodeficiency virus (HIV-1), is expressed in the human brain in a variety of cell types, including microglia and neurons. The American journal of pathology. 1997;151(4):1035-42. Epub 1997/11/05. PubMed PMID: 9327737; PubMed Central PMCID: PMC1858037.
5. Zou YR, Kottmann AH, Kuroda M, Taniuchi I, Littman DR. Function of the chemokine receptor CXCR4 in haematopoiesis and in cerebellar development. Nature. 1998;393(6685):595-9. Epub 1998/06/20. doi: 10.1038/31269. PubMed PMID: 9634238.
6. Cojoc M, Peitzsch C, Trautmann F, Polishchuk L, Telegeev GD, Dubrovska A. Emerging targets in cancer management: role of the CXCL12/CXCR4 axis. OncoTargets and therapy. 2013;6:1347-61. Epub 2013/10/15. doi: 10.2147/OTT.S36109. PubMed PMID: 24124379; PubMed Central PMCID: PMC3794844.
7. Salvucci O, Bouchard A, Baccarelli A, Deschenes J, Sauter G, Simon R, et al. The role of CXCR4 receptor expression in breast cancer: a large tissue microarray study. Breast cancer research and treatment. 2006;97(3):275-83. Epub 2005/12/14. doi: 10.1007/s10549-005-9121-8. PubMed PMID: 16344916.
8. Hassan S, Ferrario C, Saragovi U, Quenneville L, Gaboury L, Baccarelli A, et al. The influence of tumor-host interactions in the stromal cell-derived factor-1/CXCR4 ligand/receptor axis in determining metastatic risk in breast cancer. The American journal of pathology. 2009;175(1):66-73. Epub 2009/06/06. doi: 10.2353/ajpath.2009.080948. PubMed PMID: 19497995; PubMed Central PMCID: PMC2708795.
9. Chu QD, Panu L, Holm NT, Li BD, Johnson LW, Zhang S. High chemokine receptor CXCR4 level in triple negative breast cancer specimens predicts poor clinical outcome. The Journal of surgical research. 2010;159(2):689-95. Epub 2009/06/09. doi: 10.1016/j.jss.2008.09.020. PubMed PMID: 19500800.
10. Holm NT, Byrnes K, Li BD, Turnage RH, Abreo F, Mathis JM, et al. Elevated levels of chemokine receptor CXCR4 in HER-2 negative breast cancer specimens predict recurrence. The Journal of surgical research. 2007;141(1):53-9. Epub 2007/06/19. doi: 10.1016/j.jss.2007.03.015. PubMed PMID: 17574038.
11. Chu QD, Holm NT, Madumere P, Johnson LW, Abreo F, Li BD. Chemokine receptor CXCR4 overexpression predicts recurrence for hormone receptor-positive, node-negative breast cancer patients. Surgery. 2011;149(2):193-9. Epub 2010/07/06. doi: 10.1016/j.surg.2010.05.016. PubMed PMID: 20598333.
12. Zhao H, Guo L, Zhao H, Zhao J, Weng H, Zhao B. CXCR4 over-expression and survival in cancer: A system review and meta-analysis. Oncotarget. 2014. Epub 2015/02/12. PubMed PMID: 25669980.
13. Wang L, Wang Z, Liu X, Liu F. High-level C-X-C chemokine receptor type 4 expression correlates with brain-specific metastasis following complete resection of non-small cell lung cancer. Oncology letters. 2014;7(6):1871-6. Epub 2014/06/17. doi: 10.3892/ol.2014.1979. PubMed PMID: 24932250; PubMed Central PMCID: PMC4049707.
14. An H, Xu L, Zhu Y, Lv T, Liu W, Liu Y, et al. High CXC chemokine receptor 4 expression is an adverse prognostic factor in patients with clear-cell renal cell carcinoma. British journal of cancer. 2014;110(9):2261-8. Epub 2014/04/10. doi: 10.1038/bjc.2014.179. PubMed PMID: 24714746; PubMed Central PMCID: PMC4007240.

15. Wyler L, Napoli CU, Ingold B, Sulser T, Heikenwalder M, Schraml P, et al. Brain metastasis in renal cancer patients: metastatic pattern, tumour-associated macrophages and chemokine/chemoreceptor expression. British journal of cancer. 2014;110(3):686-94. Epub 2013/12/12. doi: 10.1038/bjc.2013.755. PubMed PMID: 24327013; PubMed Central PMCID: PMC3915122.
16. Balkwill F. Cancer and the chemokine network. Nature reviews Cancer. 2004;4(7):540-50. Epub 2004/07/02. doi: 10.1038/nrc1388. PubMed PMID: 15229479.
17. Dontu G, Abdallah WM, Foley JM, Jackson KW, Clarke MF, Kawamura MJ, et al. In vitro propagation and transcriptional profiling of human mammary stem/progenitor cells. Genes & development. 2003;17(10):1253-70. Epub 2003/05/21. doi: 10.1101/gad.1061803. PubMed PMID: 12756227; PubMed Central PMCID: PMC196056.
18. Dubrovska A, Elliott J, Salamone RJ, Telegeev GD, Stakhovsky AE, Schepotin IB, et al. CXCR4 expression in prostate cancer progenitor cells. PloS one. 2012;7(2):e31226. Epub 2012/02/24. doi: 10.1371/journal.pone.0031226. PubMed PMID: 22359577; PubMed Central PMCID: PMC3281066.
19. Hermann PC, Huber SL, Herrler T, Aicher A, Ellwart JW, Guba M, et al. Distinct populations of cancer stem cells determine tumor growth and metastatic activity in human pancreatic cancer. Cell stem cell. 2007;1(3):313-23. Epub 2008/03/29. doi: 10.1016/j.stem.2007.06.002. PubMed PMID: 18371365.
20. Huang M, Li Y, Zhang H, Nan F. Breast cancer stromal fibroblasts promote the generation of CD44+CD24- cells through SDF-1/CXCR4 interaction. Journal of experimental & clinical cancer research : CR. 2010;29:80. Epub 2010/06/24. doi: 10.1186/1756-9966-29-80. PubMed PMID: 20569497; PubMed Central PMCID: PMC2911413.
21. Muller A, Homey B, Soto H, Ge N, Catron D, Buchanan ME, et al. Involvement of chemokine receptors in breast cancer metastasis. Nature. 2001;410(6824):50-6. Epub 2001/03/10. doi: 10.1038/35065016. PubMed PMID: 11242036.
22. Orimo A, Gupta PB, Sgroi DC, Arenzana-Seisdedos F, Delaunay T, Naeem R, et al. Stromal fibroblasts present in invasive human breast carcinomas promote tumor growth and angiogenesis through elevated SDF-1/CXCL12 secretion. Cell. 2005;121(3):335-48. Epub 2005/05/11. doi: 10.1016/j.cell.2005.02.034. PubMed PMID: 15882617.
23. Teicher BA, Fricker SP. CXCL12 (SDF-1)/CXCR4 pathway in cancer. Clinical cancer research : an official journal of the American Association for Cancer Research. 2010;16(11):2927-31. Epub 2010/05/21. doi: 10.1158/1078-0432.CCR-09-2329. PubMed PMID: 20484021.
24. Roussos ET, Condeelis JS, Patsialou A. Chemotaxis in cancer. Nature reviews Cancer. 2011;11(8):573-87. Epub 2011/07/23. doi: 10.1038/nrc3078. PubMed PMID: 21779009; PubMed Central PMCID: PMC4030706.
25. Gassmann P, Haier J, Schluter K, Domikowsky B, Wendel C, Wiesner U, et al. CXCR4 regulates the early extravasation of metastatic tumor cells in vivo. Neoplasia. 2009;11(7):651-61. Epub 2009/07/02. PubMed PMID: 19568410; PubMed Central PMCID: PMC2697351.
26. Hernandez L, Magalhaes MA, Coniglio SJ, Condeelis JS, Segall JE. Opposing roles of CXCR4 and CXCR7 in breast cancer metastasis. Breast cancer research : BCR. 2011;13(6):R128. Epub 2011/12/14. doi: 10.1186/bcr3074. PubMed PMID: 22152016; PubMed Central PMCID: PMC3326570.
27. Basanta D, Scott JG, Fishman MN, Ayala G, Hayward SW, Anderson AR. Investigating prostate cancer tumour-stroma interactions: clinical and biological insights from an evolutionary game. British journal of cancer. 2012;106(1):174-81. Epub 2011/12/03. doi: 10.1038/bjc.2011.517. PubMed PMID: 22134510; PubMed Central PMCID: PMC3251863.
28. Buijs JT, Stayrook KR, Guise TA. TGF-beta in the Bone Microenvironment: Role in Breast Cancer Metastases. Cancer microenvironment : official journal of the International Cancer Microenvironment Society. 2011;4(3):261-81. Epub 2011/07/13. doi: 10.1007/s12307-011-0075-6. PubMed PMID: 21748439; PubMed Central PMCID: PMC3234330.
29. Eck SM, Cote AL, Winkelman WD, Brinckerhoff CE. CXCR4 and matrix metalloproteinase-1 are elevated in breast carcinoma-associated fibroblasts and in normal mammary fibroblasts exposed to factors secreted by breast cancer cells. Molecular cancer research : MCR. 2009;7(7):1033-44. Epub 2009/07/09. doi: 10.1158/1541-7786.MCR-09-0015. PubMed PMID: 19584257; PubMed Central PMCID: PMC2743167.
30. Yu L, Cecil J, Peng SB, Schrementi J, Kovacevic S, Paul D, et al. Identification and expression of novel isoforms of human stromal cell-derived factor 1. Gene. 2006;374:174-9. Epub 2006/04/22. doi: 10.1016/j.gene.2006.02.001. PubMed PMID: 16626895.

31. Rueda P, Balabanian K, Lagane B, Staropoli I, Chow K, Levoye A, et al. The CXCL12gamma chemokine displays unprecedented structural and functional properties that make it a paradigm of chemoattractant proteins. PloS one. 2008;3(7):e2543. Epub 2008/07/24. doi: 10.1371/journal.pone.0002543. PubMed PMID: 18648536; PubMed Central PMCID: PMC2481281.
32. Cavnar SP, Ray P, Moudgil P, Chang SL, Luker KE, Linderman JJ, et al. Microfluidic source-sink model reveals effects of biophysically distinct CXCL12 isoforms in breast cancer chemotaxis. Integrative biology : quantitative biosciences from nano to macro. 2014. Epub 2014/03/29. doi: 10.1039/c4ib00015c. PubMed PMID: 24675873.
33. Altenburg JD, Jin Q, Alkhatib B, Alkhatib G. The potent anti-HIV activity of CXCL12gamma correlates with efficient CXCR4 binding and internalization. Journal of virology. 2010;84(5):2563-72. Epub 2009/12/18. doi: 10.1128/JVI.00342-09. PubMed PMID: 20015992; PubMed Central PMCID: PMC2820898.
34. Balabanian K, Lagane B, Infantino S, Chow KY, Harriague J, Moepps B, et al. The chemokine SDF-1/CXCL12 binds to and signals through the orphan receptor RDC1 in T lymphocytes. The Journal of biological chemistry. 2005;280(42):35760-6. Epub 2005/08/19. doi: 10.1074/jbc.M508234200. PubMed PMID: 16107333.
35. Luker KE, Steele JM, Mihalko LA, Ray P, Luker GD. Constitutive and chemokine-dependent internalization and recycling of CXCR7 in breast cancer cells to degrade chemokine ligands. Oncogene. 2010;29(32):4599-610. Epub 2010/06/10. doi: 10.1038/onc.2010.212. PubMed PMID: 20531309; PubMed Central PMCID: PMC3164491.
36. Rajagopal S, Kim J, Ahn S, Craig S, Lam CM, Gerard NP, et al. Beta-arrestin- but not G protein-mediated signaling by the "decoy" receptor CXCR7. Proceedings of the National Academy of Sciences of the United States of America. 2010;107(2):628-32. Epub 2009/12/19. doi: 10.1073/pnas.0912852107. PubMed PMID: 20018651; PubMed Central PMCID: PMC2818968.
37. Luker KE, Lewin SA, Mihalko LA, Schmidt BT, Winkler JS, Coggins NL, et al. Scavenging of CXCL12 by CXCR7 promotes tumor growth and metastasis of CXCR4-positive breast cancer cells. Oncogene. 2012;31(45):4750-8. Epub 2012/01/24. doi: 10.1038/onc.2011.633. PubMed PMID: 22266857; PubMed Central PMCID: PMC3337948.
38. Miao Z, Luker KE, Summers BC, Berahovich R, Bhojani MS, Rehemtulla A, et al. CXCR7 (RDC1) promotes breast and lung tumor growth in vivo and is expressed on tumor-associated vasculature. Proceedings of the National Academy of Sciences of the United States of America. 2007;104(40):15735-40. Epub 2007/09/28. doi: 10.1073/pnas.0610444104. PubMed PMID: 17898181; PubMed Central PMCID: PMC1994579.
39. Torisawa YS, Mosadegh B, Bersano-Begey T, Steele JM, Luker KE, Luker GD, et al. Microfluidic platform for chemotaxis in gradients formed by CXCL12 source-sink cells. Integrative biology : quantitative biosciences from nano to macro. 2010;2(11-12):680-6. Epub 2010/09/28. doi: 10.1039/c0ib00041h. PubMed PMID: 20871938.
40. Rubin JB. Chemokine signaling in cancer: one hump or two? Seminars in cancer biology. 2009;19(2):116-22. Epub 2008/11/11. doi: 10.1016/j.semcancer.2008.10.001. PubMed PMID: 18992347; PubMed Central PMCID: PMC2694237.
41. Rajagopal S, Rajagopal K, Lefkowitz RJ. Teaching old receptors new tricks: biasing seven-transmembrane receptors. Nature reviews Drug discovery. 2010;9(5):373-86. Epub 2010/05/01. doi: 10.1038/nrd3024. PubMed PMID: 20431569; PubMed Central PMCID: PMC2902265.
42. Lagane B, Chow KY, Balabanian K, Levoye A, Harriague J, Planchenault T, et al. CXCR4 dimerization and beta-arrestin-mediated signaling account for the enhanced chemotaxis to CXCL12 in WHIM syndrome. Blood. 2008;112(1):34-44. Epub 2008/04/26. doi: 10.1182/blood-2007-07-102103. PubMed PMID: 18436740.
43. Luker KE, Gupta M, Luker GD. Imaging CXCR4 signaling with firefly luciferase complementation. Analytical chemistry. 2008;80(14):5565-73. Epub 2008/06/07. doi: 10.1021/ac8005457. PubMed PMID: 18533683.
44. Sun Y, Cheng Z, Ma L, Pei G. Beta-arrestin2 is critically involved in CXCR4-mediated chemotaxis, and this is mediated by its enhancement of p38 MAPK activation. The Journal of biological chemistry. 2002;277(51):49212-9. Epub 2002/10/09. doi: 10.1074/jbc.M207294200. PubMed PMID: 12370187.
45. Zabel BA, Wang Y, Lewen S, Berahovich RD, Penfold ME, Zhang P, et al. Elucidation of CXCR7-mediated signaling events and inhibition of CXCR4-mediated tumor cell transendothelial migration by

CXCR7 ligands. J Immunol. 2009;183(5):3204-11. Epub 2009/07/31. doi: 10.4049/jimmunol.0900269. PubMed PMID: 19641136.
46. Wurth R, Bajetto A, Harrison JK, Barbieri F, Florio T. CXCL12 modulation of CXCR4 and CXCR7 activity in human glioblastoma stem-like cells and regulation of the tumor microenvironment. Frontiers in cellular neuroscience. 2014;8:144. Epub 2014/06/07. doi: 10.3389/fncel.2014.00144. PubMed PMID: 24904289; PubMed Central PMCID: PMC4036438.
47. Liles WC, Broxmeyer HE, Rodger E, Wood B, Hubel K, Cooper S, et al. Mobilization of hematopoietic progenitor cells in healthy volunteers by AMD3100, a CXCR4 antagonist. Blood. 2003;102(8):2728-30. Epub 2003/07/12. doi: 10.1182/blood-2003-02-0663. PubMed PMID: 12855591.
48. Roccaro AM, Sacco A, Jimenez C, Maiso P, Moschetta M, Mishima Y, et al. C1013G/CXCR4 acts as a driver mutation of tumor progression and modulator of drug resistance in lymphoplasmacytic lymphoma. Blood. 2014;123(26):4120-31. Epub 2014/04/09. doi: 10.1182/blood-2014-03-564583. PubMed PMID: 24711662.
49. Uy GL, Rettig MP, Motabi IH, McFarland K, Trinkaus KM, Hladnik LM, et al. A phase 1/2 study of chemosensitization with the CXCR4 antagonist plerixafor in relapsed or refractory acute myeloid leukemia. Blood. 2012;119(17):3917-24. Epub 2012/02/07. doi: 10.1182/blood-2011-10-383406. PubMed PMID: 22308295; PubMed Central PMCID: PMC3350358.
50. Dale DC, Bolyard AA, Kelley ML, Westrup EC, Makaryan V, Aprikyan A, et al. The CXCR4 antagonist plerixafor is a potential therapy for myelokathexis, WHIM syndrome. Blood. 2011;118(18):4963-6. Epub 2011/08/13. doi: 10.1182/blood-2011-06-360586. PubMed PMID: 21835955; PubMed Central PMCID: PMC3673761.
51. Girbl T, Lunzer V, Greil R, Namberger K, Hartmann TN. The CXCR4 and adhesion molecule expression of CD34+ hematopoietic cells mobilized by "on-demand" addition of plerixafor to granulocyte-colony-stimulating factor. Transfusion. 2014;54(9):2325-35. Epub 2014/03/29. doi: 10.1111/trf.12632. PubMed PMID: 24673458; PubMed Central PMCID: PMC4215600.
52. Lanza F, Lemoli RM, Olivieri A, Laszlo D, Martino M, Specchia G, et al. Factors affecting successful mobilization with plerixafor: an Italian prospective survey in 215 patients with multiple myeloma and lymphoma. Transfusion. 2014;54(2):331-9. Epub 2013/06/21. doi: 10.1111/trf.12265. PubMed PMID: 23781769.
53. Nademanee AP, DiPersio JF, Maziarz RT, Stadtmauer EA, Micallef IN, Stiff PJ, et al. Plerixafor plus granulocyte colony-stimulating factor versus placebo plus granulocyte colony-stimulating factor for mobilization of CD34(+) hematopoietic stem cells in patients with multiple myeloma and low peripheral blood CD34(+) cell count: results of a subset analysis of a randomized trial. Biology of blood and marrow transplantation : journal of the American Society for Blood and Marrow Transplantation. 2012;18(10):1564-72. Epub 2012/06/12. doi: 10.1016/j.bbmt.2012.05.017. PubMed PMID: 22683613.
54. Broxmeyer HE, Orschell CM, Clapp DW, Hangoc G, Cooper S, Plett PA, et al. Rapid mobilization of murine and human hematopoietic stem and progenitor cells with AMD3100, a CXCR4 antagonist. The Journal of experimental medicine. 2005;201(8):1307-18. Epub 2005/04/20. doi: 10.1084/jem.20041385. PubMed PMID: 15837815; PubMed Central PMCID: PMC2213145.
55. Hendrix CW, Collier AC, Lederman MM, Schols D, Pollard RB, Brown S, et al. Safety, pharmacokinetics, and antiviral activity of AMD3100, a selective CXCR4 receptor inhibitor, in HIV-1 infection. J Acquir Immune Defic Syndr. 2004;37(2):1253-62. Epub 2004/09/24. PubMed PMID: 15385732.
56. McDermott DH, Liu Q, Ulrick J, Kwatemaa N, Anaya-O'Brien S, Penzak SR, et al. The CXCR4 antagonist plerixafor corrects panleukopenia in patients with WHIM syndrome. Blood. 2011;118(18):4957-62. Epub 2011/09/06. doi: 10.1182/blood-2011-07-368084. PubMed PMID: 21890643; PubMed Central PMCID: PMC3208300.
57. Rubin JB, Kung AL, Klein RS, Chan JA, Sun Y, Schmidt K, et al. A small-molecule antagonist of CXCR4 inhibits intracranial growth of primary brain tumors. Proceedings of the National Academy of Sciences of the United States of America. 2003;100(23):13513-8. Epub 2003/11/05. doi: 10.1073/pnas.2235846100. PubMed PMID: 14595012; PubMed Central PMCID: PMC263845.
58. Porvasnik S, Sakamoto N, Kusmartsev S, Eruslanov E, Kim WJ, Cao W, et al. Effects of CXCR4 antagonist CTCE-9908 on prostate tumor growth. The Prostate. 2009;69(13):1460-9. Epub 2009/07/10. doi: 10.1002/pros.21008. PubMed PMID: 19588526.
59. Kozin SV, Kamoun WS, Huang Y, Dawson MR, Jain RK, Duda DG. Recruitment of myeloid but not endothelial precursor cells facilitates tumor regrowth after local irradiation. Cancer research.

2010;70(14):5679-85. Epub 2010/07/16. doi: 10.1158/0008-5472.CAN-09-4446. PubMed PMID: 20631066; PubMed Central PMCID: PMC2918387.
60. Kioi M, Vogel H, Schultz G, Hoffman RM, Harsh GR, Brown JM. Inhibition of vasculogenesis, but not angiogenesis, prevents the recurrence of glioblastoma after irradiation in mice. The Journal of clinical investigation. 2010;120(3):694-705. Epub 2010/02/25. doi: 10.1172/JCI40283. PubMed PMID: 20179352; PubMed Central PMCID: PMC2827954.
61. Redjal N, Chan JA, Segal RA, Kung AL. CXCR4 inhibition synergizes with cytotoxic chemotherapy in gliomas. Clinical cancer research : an official journal of the American Association for Cancer Research. 2006;12(22):6765-71. Epub 2006/11/24. doi: 10.1158/1078-0432.CCR-06-1372. PubMed PMID: 17121897.
62. Wong D, Kandagatla P, Korz W, Chinni SR. Targeting CXCR4 with CTCE-9908 inhibits prostate tumor metastasis. BMC urology. 2014;14:12. Epub 2014/01/30. doi: 10.1186/1471-2490-14-12. PubMed PMID: 24472670; PubMed Central PMCID: PMC3912255.
63. Richert MM, Vaidya KS, Mills CN, Wong D, Korz W, Hurst DR, et al. Inhibition of CXCR4 by CTCE-9908 inhibits breast cancer metastasis to lung and bone. Oncology reports. 2009;21(3):761-7. Epub 2009/02/13. PubMed PMID: 19212637.
64. Kalatskaya I, Berchiche YA, Gravel S, Limberg BJ, Rosenbaum JS, Heveker N. AMD3100 is a CXCR7 ligand with allosteric agonist properties. Molecular pharmacology. 2009;75(5):1240-7. Epub 2009/03/04. doi: 10.1124/mol.108.053389. PubMed PMID: 19255243.
65. Yoshikawa Y, Oishi S, Kubo T, Tanahara N, Fujii N, Furuya T. Optimized method of G-protein-coupled receptor homology modeling: its application to the discovery of novel CXCR7 ligands. Journal of medicinal chemistry. 2013;56(11):4236-51. Epub 2013/05/10. doi: 10.1021/jm400307y. PubMed PMID: 23656360.
66. Liu Y, Carson-Walter E, Walter KA. Chemokine receptor CXCR7 is a functional receptor for CXCL12 in brain endothelial cells. PloS one. 2014;9(8):e103938. Epub 2014/08/02. doi: 10.1371/journal.pone.0103938. PubMed PMID: 25084358; PubMed Central PMCID: PMC4118981.
67. Proudfoot AE, Handel TM, Johnson Z, Lau EK, LiWang P, Clark-Lewis I, et al. Glycosaminoglycan binding and oligomerization are essential for the in vivo activity of certain chemokines. Proceedings of the National Academy of Sciences of the United States of America. 2003;100(4):1885-90. Epub 2003/02/07. doi: 10.1073/pnas.0334864100. PubMed PMID: 12571364; PubMed Central PMCID: PMC149928.
68. Altenburg JD, Broxmeyer HE, Jin Q, Cooper S, Basu S, Alkhatib G. A naturally occurring splice variant of CXCL12/stromal cell-derived factor 1 is a potent human immunodeficiency virus type 1 inhibitor with weak chemotaxis and cell survival activities. Journal of virology. 2007;81(15):8140-8. Epub 2007/05/18. doi: 10.1128/JVI.00268-07. PubMed PMID: 17507482; PubMed Central PMCID: PMC1951332.
69. Laguri C, Sadir R, Rueda P, Baleux F, Gans P, Arenzana-Seisdedos F, et al. The novel CXCL12gamma isoform encodes an unstructured cationic domain which regulates bioactivity and interaction with both glycosaminoglycans and CXCR4. PloS one. 2007;2(10):e1110. Epub 2007/11/01. doi: 10.1371/journal.pone.0001110. PubMed PMID: 17971873; PubMed Central PMCID: PMC2040504.
70. Gahan JC, Gosalbez M, Yates T, Young EE, Escudero DO, Chi A, et al. Chemokine and chemokine receptor expression in kidney tumors: molecular profiling of histological subtypes and association with metastasis. The Journal of urology. 2012;187(3):827-33. Epub 2012/01/17. doi: 10.1016/j.juro.2011.10.150. PubMed PMID: 22245330.
71. Rappel WJ, Levine H. Receptor noise limitations on chemotactic sensing. Proceedings of the National Academy of Sciences of the United States of America. 2008;105(49):19270-5. Epub 2008/12/10. doi: 10.1073/pnas.0804702105. PubMed PMID: 19064934; PubMed Central PMCID: PMC2614751.
72. Mercer J, Helenius A. Virus entry by macropinocytosis. Nature cell biology. 2009;11(5):510-20. Epub 2009/05/01. doi: 10.1038/ncb0509-510. PubMed PMID: 19404330.
73. Swanson JA. Shaping cups into phagosomes and macropinosomes. Nature reviews Molecular cell biology. 2008;9(8):639-49. Epub 2008/07/10. doi: 10.1038/nrm2447. PubMed PMID: 18612320; PubMed Central PMCID: PMC2851551.
74. Ma CX, Ellis MJ. The Cancer Genome Atlas: clinical applications for breast cancer. Oncology (Williston Park). 2013;27(12):1263-9, 74-9. Epub 2014/03/15. PubMed PMID: 24624545.

75. Rhodes DR, Yu J, Shanker K, Deshpande N, Varambally R, Ghosh D, et al. ONCOMINE: a cancer microarray database and integrated data-mining platform. Neoplasia. 2004;6(1):1-6. Epub 2004/04/08. PubMed PMID: 15068665; PubMed Central PMCID: PMC1635162.
76. Gao J, Aksoy BA, Dogrusoz U, Dresdner G, Gross B, Sumer SO, et al. Integrative analysis of complex cancer genomics and clinical profiles using the cBioPortal. Science signaling. 2013;6(269):pl1. Epub 2013/04/04. doi: 10.1126/scisignal.2004088. PubMed PMID: 23550210; PubMed Central PMCID: PMC4160307.
77. Liotta L, Petricoin E. Molecular profiling of human cancer. Nat Rev Genet. 2000;1(1):48-56. Epub 2001/03/27. doi: 10.1038/35049567. PubMed PMID: 11262874.
78. Frances N, Claret L, Bruno R, Iliadis A. Tumor growth modeling from clinical trials reveals synergistic anticancer effect of the capecitabine and docetaxel combination in metastatic breast cancer. Cancer chemotherapy and pharmacology. 2011;68(6):1413-9. Epub 2011/04/09. doi: 10.1007/s00280-011-1628-6. PubMed PMID: 21476101.
79. Gatenby RA, Gawlinski ET. A reaction-diffusion model of cancer invasion. Cancer research. 1996;56(24):5745-53. Epub 1996/12/15. PubMed PMID: 8971186.
80. Kim Y, Wallace J, Li F, Ostrowski M, Friedman A. Transformed epithelial cells and fibroblasts/myofibroblasts interaction in breast tumor: a mathematical model and experiments. Journal of mathematical biology. 2010;61(3):401-21. Epub 2009/11/11. doi: 10.1007/s00285-009-0307-2. PubMed PMID: 19902212.
81. Zhu X, Zhou X, Lewis MT, Xia L, Wong S. Cancer stem cell, niche and EGFR decide tumor development and treatment response: A bio-computational simulation study. J Theor Biol. 2011;269(1):138-49. Epub 2010/10/26. doi: 10.1016/j.jtbi.2010.10.016. PubMed PMID: 20969880; PubMed Central PMCID: PMC3153880.
82. Anderson AR, Quaranta V. Integrative mathematical oncology. Nature reviews Cancer. 2008;8(3):227-34. Epub 2008/02/15. doi: 10.1038/nrc2329. PubMed PMID: 18273038.
83. Deisboeck TS, Wang Z, Macklin P, Cristini V. Multiscale cancer modeling. Annual review of biomedical engineering. 2011;13:127-55. Epub 2011/05/03. doi: 10.1146/annurev-bioeng-071910-124729. PubMed PMID: 21529163; PubMed Central PMCID: PMC3883359.
84. Bauer AL, Beauchemin CA, Perelson AS. Agent-based modeling of host-pathogen systems: The successes and challenges. Information sciences. 2009;179(10):1379-89. Epub 2010/02/18. PubMed PMID: 20161146; PubMed Central PMCID: PMC2731970.
85. Hwang M, Garbey M, Berceli SA, Tran-Son-Tay R. Rule-Based Simulation of Multi-Cellular Biological Systems-A Review of Modeling Techniques. Cell Mol Bioeng. 2009;2(3):285-94. Epub 2009/09/01. doi: 10.1007/s12195-009-0078-2. PubMed PMID: 21369345; PubMed Central PMCID: PMC3045734.
86. Athale CA, Deisboeck TS. The effects of EGF-receptor density on multiscale tumor growth patterns. J Theor Biol. 2006;238(4):771-9. Epub 2005/08/30. doi: 10.1016/j.jtbi.2005.06.029. PubMed PMID: 16126230.
87. Chakrabarti A, Verbridge S, Stroock AD, Fischbach C, Varner JD. Multiscale models of breast cancer progression. Annals of biomedical engineering. 2012;40(11):2488-500. Epub 2012/09/26. doi: 10.1007/s10439-012-0655-8. PubMed PMID: 23008097; PubMed Central PMCID: PMC3868441.
88. Fallahi-Sichani M, El-Kebir M, Marino S, Kirschner DE, Linderman JJ. Multiscale computational modeling reveals a critical role for TNF-alpha receptor 1 dynamics in tuberculosis granuloma formation. J Immunol. 2011;186(6):3472-83. Epub 2011/02/16. doi: 10.4049/jimmunol.1003299. PubMed PMID: 21321109; PubMed Central PMCID: PMC3127549.
89. Qutub AA, Mac Gabhann F, Karagiannis ED, Vempati P, Popel AS. Multiscale models of angiogenesis. IEEE engineering in medicine and biology magazine : the quarterly magazine of the Engineering in Medicine & Biology Society. 2009;28(2):14-31. Epub 2009/04/08. doi: 10.1109/MEMB.2009.931791. PubMed PMID: 19349248; PubMed Central PMCID: PMC3077679.
90. Walpole J, Papin JA, Peirce SM. Multiscale computational models of complex biological systems. Annual review of biomedical engineering. 2013;15:137-54. Epub 2013/05/07. doi: 10.1146/annurev-bioeng-071811-150104. PubMed PMID: 23642247; PubMed Central PMCID: PMC3970111.
91. Wang Z, Bordas V, Deisboeck TS. Discovering Molecular Targets in Cancer with Multiscale Modeling. Drug development research. 2011;72(1):45-52. Epub 2011/05/17. doi: 10.1002/ddr.20401. PubMed PMID: 21572568; PubMed Central PMCID: PMC3092304.

92. Wang Z, Bordas V, Sagotsky J, Deisboeck TS. Identifying therapeutic targets in a combined EGFR-TGFbetaR signalling cascade using a multiscale agent-based cancer model. Mathematical medicine and biology : a journal of the IMA. 2012;29(1):95-108. Epub 2010/12/15. doi: 10.1093/imammb/dqq023. PubMed PMID: 21147846; PubMed Central PMCID: PMC3499073.
93. Wang Z, Zhang L, Sagotsky J, Deisboeck TS. Simulating non-small cell lung cancer with a multiscale agent-based model. Theoretical biology & medical modelling. 2007;4:50. Epub 2007/12/25. doi: 10.1186/1742-4682-4-50. PubMed PMID: 18154660; PubMed Central PMCID: PMC2259313.
94. Zhang L, Strouthos CG, Wang Z, Deisboeck TS. Simulating Brain Tumor Heterogeneity with a Multiscale Agent-Based Model: Linking Molecular Signatures, Phenotypes and Expansion Rate. Mathematical and computer modelling. 2009;49(1-2):307-19. Epub 2010/01/05. doi: 10.1016/j.mcm.2008.05.011. PubMed PMID: 20047002; PubMed Central PMCID: PMC2653254.
95. Hashambhoy YL, Chappell JC, Peirce SM, Bautch VL, Mac Gabhann F. Computational modeling of interacting VEGF and soluble VEGF receptor concentration gradients. Frontiers in physiology. 2011;2:62. Epub 2011/10/19. doi: 10.3389/fphys.2011.00062. PubMed PMID: 22007175; PubMed Central PMCID: PMC3185289.
96. Hayenga HN, Thorne BC, Peirce SM, Humphrey JD. Ensuring congruency in multiscale modeling: towards linking agent based and continuum biomechanical models of arterial adaptation. Annals of biomedical engineering. 2011;39(11):2669-82. Epub 2011/08/03. doi: 10.1007/s10439-011-0363-9. PubMed PMID: 21809144; PubMed Central PMCID: PMC3207323.
97. Thorne BC, Hayenga HN, Humphrey JD, Peirce SM. Toward a multi-scale computational model of arterial adaptation in hypertension: verification of a multi-cell agent based model. Frontiers in physiology. 2011;2:20. Epub 2011/07/02. doi: 10.3389/fphys.2011.00020. PubMed PMID: 21720536; PubMed Central PMCID: PMC3118494.
98. Mansury Y, Kimura M, Lobo J, Deisboeck TS. Emerging patterns in tumor systems: simulating the dynamics of multicellular clusters with an agent-based spatial agglomeration model. J Theor Biol. 2002;219(3):343-70. Epub 2002/11/07. PubMed PMID: 12419662.
99. Vital-Lopez FG, Armaou A, Hutnik M, Maranas CD. Modeling the Effect of Chemotaxis on Glioblastoma Tumor Progression. Aiche J. 2011;57(3):778-92. doi: Doi 10.1002/Aic.12296. PubMed PMID: ISI:000287104700019.
100. Lin F, Butcher EC. Modeling the role of homologous receptor desensitization in cell gradient sensing. J Immunol. 2008;181(12):8335-43. Epub 2008/12/04. PubMed PMID: 19050250; PubMed Central PMCID: PMC2596625.
101. Helton JC, Johnson JD, Sallaberry CJ, Storlie CB. Survey of sampling-based methods for uncertainty and sensitivity analysis. Reliab Eng Syst Safe. 2006;91(10-11):1175-209. doi: Doi 10.1016/J.Ress.2005.11.017. PubMed PMID: ISI:000241350400009.
102. Marino S, Hogue IB, Ray CJ, Kirschner DE. A methodology for performing global uncertainty and sensitivity analysis in systems biology. J Theor Biol. 2008;254(1):178-96. Epub 2008/06/24. doi: 10.1016/j.jtbi.2008.04.011. PubMed PMID: 18572196; PubMed Central PMCID: PMC2570191.
103. Kinzer-Ursem TL, Linderman JJ. Both ligand- and cell-specific parameters control ligand agonism in a kinetic model of g protein-coupled receptor signaling. PLoS computational biology. 2007;3(1):e6. Epub 2007/01/16. doi: 10.1371/journal.pcbi.0030006. PubMed PMID: 17222056; PubMed Central PMCID: PMC1769407.

Chapter 2

A comprehensive analysis of CXCL12 isoforms in breast cancer

2.1 Abstract

CXCL12-CXCR4-CXCR7 signaling promotes tumor growth and metastasis in breast cancer. Alternative splicing of CXCL12 produces isoforms with distinct structural and biochemical properties, but little is known about isoform-specific differences in breast cancer subtypes and patient outcomes. We investigated global expression profiles of the six CXCL12 isoforms, CXCR4, and CXCR7, in The Cancer Genome Atlas (TCGA) breast cancer cohort using next generation RNA sequencing in 948 breast cancer and benign samples, and seven breast cancer cell lines. We compared expression levels with several clinical parameters, as well as metastasis, recurrence, and overall survival. CXCL12-α, β, and γ are highly co-expressed, with low expression correlating with more aggressive subtypes, higher stage disease, and worse clinical outcomes. CXCL12-δ did not correlate with other isoforms, but was prognostic for overall survival and showed the same trend for metastasis and recurrence free survival. Effects of CXCL12-δ remained independently prognostic when taking into account expression of CXCL12, CXCR4, and CXCR7. These results were also reflected when comparing CXCL12-α, -β, and -γ in breast cancer cell lines. We summarized expression of all CXCL12 isoforms in an important chemokine signaling pathway in breast cancer in a large clinical cohort and common breast cancer cell lines, establishing differences among isoforms in multiple clinical, pathologic, and molecular subgroups. We identified for the first time the clinical importance of a previously unstudied isoform, CXCL12-δ.

2.2 Introduction

Nearly all human genes undergo alternative splicing, substantially increasing diversity in protein structure and function [1]. Genome-wide analyses of several different cancers demonstrate extensive perturbations in splicing during tumor initiation and metastasis [2,3]. Alternatively spliced proteins regulate fundamental processes in cancer, including apoptosis, metabolism, and metastasis, suggesting that dysregulated splicing is critical to malignancy [4-6]. As prominent examples of alternative splicing in cancer, a switch from pyruvate kinase M1 (PKM1) to the M2 isoform drives anabolic metabolism in malignant cells, and a novel splice variant of the transmembrane protein CD44 promotes metastasis [5,7-9]. Isoforms of these and other genes preferentially expressed in malignant versus normal tissues provide potential biomarkers for detection of cancer and may contribute to drug resistance of cancer cells. Identifying changes in protein isoform expression in cancer will improve understanding of key signaling pathways in tumorigenesis and point to novel therapeutic targets to improve cancer therapy [10,11].

Chemokine CXCL12 and its chemokine receptors CXCR4 and CXCR7 (recently renamed as ACKR3) comprise a signaling axis strongly linked to tumor growth and metastasis in breast cancer and more than 20 other malignancies [12,13]. CXCL12 binding to CXCR4 activates pathways including phosphatidylinositol-3 kinase and mitogen activated protein kinases (MAPK) to promote growth, survival, and chemotaxis of breast cancer cells. High levels of CXCL12 are expressed in common sites of breast cancer metastasis such as lung, liver, bone, and brain [14]. CXCR4 commonly is upregulated on breast cancer cells, and numerous studies have demonstrated both gene and protein overexpression of CXCR4 on cancer cells in primary breast tumors [15-18]. The anatomic distribution of CXCL12 and studies in mouse models of cancer suggest that gradients of this chemokine drive local invasion and subsequent homing of CXCR4+ breast cancer cells to secondary sites [18,19]. CXCR7 also is expressed by breast cancer cells and stromal cells, such as endothelium on tumor vasculature, in primary breast cancers [20]. CXCR7 functions as a scavenger receptor for CXCL12, functioning in part to decrease amounts of this chemokine in the extracellular space and establish

chemotactic gradients [21,22]. CXCR7 also promotes survival and invasion of malignant cells [23].

Although six different isoforms of human CXCL12 (α, β, γ, δ, ε, and φ) have been described, most studies of CXCL12 focus only on the α isoform or do not distinguish among isoforms [24]. CXCL12 may be secreted by malignant cells in primary breast cancers in addition to carcinoma-associated fibroblasts and/or mesenchymal stem cells in the tumor microenvironment [17,25,26]. Fibroblasts isolated from primary breast tumors secrete CXCL12 at higher levels than fibroblasts from normal mammary tissue despite no genetic mutations in stroma [27,28]. These findings suggest that cancer cells stimulate adjacent fibroblasts to produce higher levels of total CXCL12 in breast tumors than normal mammary tissue [28]. However, while these data demonstrate that carcinoma-associated fibroblasts are characterized by increased CXCL12, it remains unclear to what extent total CXCL12 in breast cancers differs from normal tissue and affects prognosis. Based on expression of CXCL12-α and -β in two different breast cancer microarray datasets and immunohistochemistry of primary breast tumors, Mirisola and colleagues reported that higher expression levels of CXCL12-α and -β correlate with better disease-free survival [29]. However, a separate high throughput analysis of CXCL12 expression concluded that higher CXCL12 levels correlate with increased metastasis and local recurrence in breast cancer [17]. Determining effects of high versus low CXCL12 on prognosis and disease progression in breast cancer is essential to direct optimal use of therapeutic antibodies and other agents being developed for CXCL12-targeted cancer therapy [30].

Prior genetic analyses of mRNA for CXCL12 isoforms have used microarrays, which frequently lack probes to detect specific isoforms of these genes. However, next-generation sequencing overcomes this limitation. Using bioinformatics analysis of publicly available data sets from The Cancer Genome Atlas (TCGA), we investigated expression of CXCL12 isoforms, as well as CXCR4 and CXCR7 in breast cancer. We then correlated patterns of expression with important molecular phenotypes, clinical parameters, and outcomes in these patients. These analyses revealed distinct differences

in expression for various isoforms of these genes. We show that low levels of expression of CXCL12 correlate with worse prognosis in breast cancer with isoform-specific differences among α, β, γ, and δ isoforms. These data demonstrate the impact of CXCL12 isoforms in breast cancer and underscore the need to better understand functional differences among these molecules in disease progression and therapy.

2.3 Methods

2.3.1 Study Design and RNA Sequencing

Publicly available RNA next-generation sequencing and clinical data (844 breast cancer and 104 benign breast samples) were retrieved from The Cancer Genome Atlas (TCGA) for breast cancer [31]. Additional clinical data such as PAM50 clustering and clinical follow-up for the TCGA were obtained from the UCSC Cancer Genomics Browser [32]. RNA sequencing data for seven breast cancer cell lines (two samples each) were obtained from the Illumina iDEA database (www.illumina.com). Three of these cell lines have been shown to have metastatic potential (BT20, MDA-MB-231, and MDA-MB-468), and four cell lines have been shown to have no metastatic potential (BT474, MCF7, T47D, and ZR-75-1) [33-35]. RNA sequencing reads were aligned to the genome with Tophat [36] using Genome Reference Consortium Human Build 37 (GRCh37 or hg19) (www.ncbi.nlm.nih.gov) as the reference genome.

Seven hundred eighty-five of the cancer samples had clinical data from TCGA, and 832 had data from UCSC Cancer Genome Browser. Her2 status was not included as a column, so we calculated it based on the immunohistochemistry (IHC) data column. For cases with equivocal IHC, we then used the in-situ hybridization (ISH) data column.

Normalization was performed using Fragments per Kilobase per Million (FPKM), and isoform expression values were generated using Cufflinks with Ensembl version 69 as the reference transcriptome [37]. Cufflinks calculates isoform expression levels using a statistical model in which the probability of observing a given fragment is a linear function of the transcript abundance. Gene level expression is the sum of transcript level

expression, as each read is assigned to a single transcript. Tophat was chosen because it is the standard sequence aligner used by Cufflinks [38].

2.3.2 Statistical and Bioinformatics Analysis

Correlation coefficients were generated using Spearman's correlation. Hierarchical clustering was performed on the covariance matrices to generate heat maps. Expression levels of the isoforms and at the gene level were compared across clinical and pathologic groups such as cancer vs. normal, tumor stage, histology, hormone receptor status, and PAM50 cluster [39]. Means between groups were compared using Analysis of Variance (ANOVA). Expression was divided into high versus low expression using the median expression value. Kaplan Meier curves were generated for the high and low expression groups and compared using the Log-rank test for metastasis free survival (MFS), recurrence free survival (RFS), and overall survival (OS). Hazard ratios (HR) were generated using univariate Cox regression. Multi-gene analysis was performed using Cox regression with expression of each gene/isoform as a covariate. Comparison of expression between metastatic versus non-metastatic cell lines was performed using Student's T-test. Statistics and plots were generated using the R statistical computing software and GraphPad Prism.

2.4 Results

2.4.1 Differential expression of CXCL12 isoforms, CXCR4, and CXCR7 in breast cancer versus normal breast tissue

Studies of isoforms of CXCL12 in cancer and other diseases have been limited by the lack of isoform-specific probes on microarrays and antibodies for immunohistochemistry. As a result, studies have focused predominantly on only the α and β isoforms of CXCL12. To overcome limitations of microarrays and antibodies, we investigated expression levels of all isoforms of CXCL12 and receptors CXCR4 and CXCR7 in breast cancer using the TCGA RNA sequencing dataset. The clinical and pathologic characteristics of the tumor samples and patients in this dataset are shown in Table 1.

The Cufflinks analysis program assigns each read to individual isoforms such that the sum of expression levels for a specific isoform is equal to the gene level of expression.

Based on this analysis, we determined that the most common isoform of CXCL12 in breast cancer is α (65%), followed by β (27%) > γ (5%) > δ (2%). We detected only very low levels of expression for CXCL12-ε (0.1%) and –φ (0.2%), and therefore refrained from statistical inference using these isoforms.

To establish for the first time correlations among CXCL12 isoforms, CXCR4, and CXCR7, we examined the Spearman's covariance matrix with hierarchal clustering for breast cancer and normal tissue, respectively (Figure 2.1A, 2.1B). In breast cancer, CXCL12 α and β were highly correlated (correlation coefficient of 0.91), and these two isoforms also correlated highly with gene-level expression of CXCL12 (correlation coefficients of 0.99 and 0.95 for CXCL12 α and β, respectively) (Figure 2.1A). By comparison, the γ, ε, and φ isoforms of CXCL12 correlated moderately with expression of α, β, and gene-level expression (correlation coefficients of 0.44 to 0.59). Interestingly, the δ isoform, which is not well characterized in the literature, correlated very poorly with the other CXCL12 isoforms (correlation coefficients of -0.11 to 0.27) and in cancer samples, clustered with CXCR4 and CXCR7 rather than with the other CXCL12 isoforms. CXCR4 and CXCR7 displayed a weak, positive correlation with gene-level expression of CXCL12 and its α and β isoforms, but did not correlate with each other. These same general correlations were present in normal samples (Figure 2.1B). However, in normal samples, CXCR7 tended to correlate inversely with CXCR4, and CXCR7 also exhibited modest to strong correlations with CXCL12-α, β, and overall gene-level expression of this chemokine.

We next investigated levels of expression for various chemokine and receptor isoforms in cancer and normal tissues. While previous publications report discordant results for CXCL12 in breast cancer versus normal breast, our analysis showed significant downregulation of CXCL12-α, β, and γ in cancer (Figure 2.1C). Expression of CXCL12-δ also decreased in cancer as compared with normal, although differences were not significant. Similarly, CXCR7 was downregulated in cancer. CXCR4 demonstrated the opposite pattern with upregulation in cancer, consistent with prior literature [15,17,18].

2.4.2 Variations among CXCL12 isoforms, CXCR4, and CXCR7 with clinical and molecular staging parameters

Within cancer samples, CXCL12-α, β, and γ varied significantly with tumor stage (Figure 2.2A). For these isoforms of CXCL12, lower stage tumors had higher levels of expression with the highest amounts of each isoform present in stage I primary breast tumors. We observed a similar trend for gene-level expression of CXCL12. We also compared differences in expression of various isoforms with histologic classifications of breast cancer. Invasive ductal and invasive lobular carcinomas comprise the majority of the TCGA data set, and most of the mixed histology samples contain features of both invasive ductal and lobular cancer. Gene-level expression of CXCL12, as well as α, β, and γ isoforms, showed significant variations across different histologic groups (Figure 2.2B). Amounts of total CXCL12 and these three isoforms were highest in invasive lobular cancer with a rank order of invasive lobular > mixed > invasive ductal carcinoma. We note that lowest levels of expression for CXCL12 and the α, β, and γ isoforms occurred in less common histologic types of breast cancer, medullary and mucinous. Other isoforms of CXCL12 did not vary significantly with tumor stage or histologic type, and we also did not identify significant correlations with gene-level CXCR4 or CXCR7.

In clinical oncology, breast cancers are categorized based on hormone receptors (estrogen [ER] and progesterone [PR]) and amplification of the oncogene Her2. These categories determine prognosis and treatment options [40]. We analyzed expression of CXCL12, CXCR4, and CXCR7 and individual isoforms in tumors positive for both ER and PR, Her2 only, and all three receptors (triple positive), as well as primary cancers lacking expression of these three receptors (triple negative). Gene-level expression of CXCL12 and the α and β isoforms each varied significantly across these subtypes with highest amounts in ER/PR positive and triple positive cancers (Figure 2.3A). By comparison, levels of overall CXCL12, CXCL12-α, and CXCL12-β decreased in triple negative cancer and to an even greater extent in Her2 positive tumors. Other isoforms of CXCL12 did not vary significantly with receptor status. CXCR7 varied with receptor status in a pattern comparable to CXCL12 (Figure 2.3A). Levels of CXCR7 were highest in ER/PR positive and triple positive tumors with lower expression in triple negative and Her2

positive cancers. Interestingly, we identified a distinct pattern of expression for CXCR4, which was elevated in triple negative breast cancer relative to the other groups [41].

More recently, breast cancers have been classified into intrinsic molecular subtypes (Normal-like, Luminal A, Luminal B, Her2-enriched, and Basal-like) defined by a 50 gene panel referred to as PAM50. Intrinsic subtypes add prognostic and predictive information to standard metrics used to categorize breast cancer. When analyzed across intrinsic subtypes, CXCL12 and its α, β, and γ isoforms varied significantly (Figure 2.3B). Expression was highest in the Normal-like cluster, which is consistent with our data in Figure 2.1A showing upregulation of these isoforms in normal samples. Luminal A had the next highest expression with Luminal B, Her2-enriched, and Basal clusters exhibiting lower expression. We also identified significant variations of receptors with intrinsic subtypes of breast cancer. CXCR4 showed differential expression among clusters with lowest levels in Luminal A and Luminal B subtypes and highest expression in Basal cancers. By comparison, levels of CXCR7 were highest in Luminal A and Luminal B subtypes.

CXCL12 and its α, β, and γ isoforms vary significantly with race. We identified higher expression in whites than Asians or African-Americans (Figure 2.7A). Gene-level CXCL12 and the α isoform also changed significantly by age group with levels peaking in the 50-60 year age group relative to younger or older patients (Figure 2.7B). CXCL12-β and -γ showed a similar pattern across age groups, although differences were not significant. We did not identify significant correlations for race or age groups for CXCR4 or CXCR7.

2.4.3 CXCL12 isoforms correlate with patient outcomes

We next examined the correlation of gene and isoform expression with important clinical outcomes in breast cancer: metastasis, recurrence, and overall survival. Kaplan-Meier curves for high versus low expression of gene-level CXCL12 demonstrated that low-expression of gene-level CXCL12 corresponded with a significantly worse MFS (p-value < 0.008, HR=2.2), but not RFS or OS (Figure 2.4A-C). Similarly, low expression of CXCL12-α corresponded with significantly worse MFS (p-value < 0.033, HR=1.9) but

not RFS or OS (Figure 2.4D-F). Unlike CXCL12-α, low levels of both CXCL12-β and -γ correlated with significantly worse MFS (β isoform p-value < 0.0015, HR=2.6; γ isoform p-value < 0.011, HR=2.2) and RFS (β isoform p-value < 0.028, HR=2.1; γ isoform p-value < 0.024, HR=2.1), but not OS (Figure 2.4G-L).

CXCL12-δ, the isoform that does not correlate with expression patterns of other isoforms in breast cancer or normal breast tissue, had a different association with outcomes. Low expression of the δ isoform also showed trends for reduced MFS and RFS (Figure 2.4M,N), although not statistically significant (MFS, p-value < 0.16, HR=1.5; RFS, p-value < 0.077, HR=1.7). Notably, low CXCL12 δ was the only CXCL12 isoform correlated with worse OS (p-value < 0.0035, HR=1.8) (Figure 2.4O).

CXCL12, CXCR4, and CXCR7 do not operate independently, but as important components in a complex network. We examined the expression levels of CXCL12- δ, the least understood isoform in the context of the expression of the other genes in the pathway. Low CXCL12- δ is independently prognostic for OS even after taking into account CXCL12, CXCR4, and CXCR7 expression (p-value < 0.004, HR=0.56), and shows the same trend in MFS and RFS (Figure 2.5A-C) multi-gene analysis.

2.4.4 CXCL12 isoforms correlate with metastatic potential in breast cancer cell lines

By nature, clinical samples such as the TCGA contain a mix of cell types, including tumor cells, normal breast tissue and vasculature, making it difficult to identify the cell type(s) producing each transcript. To overcome this limitation, we examined RNAseq data in seven breast cancer cell lines for CXCL12 isoforms. Surprisingly, we find isoform expression shows a different trend than in the TCGA samples, with γ showing the highest expression proportion (42%), followed by α (33%) > β (24%). We detected only very low levels of expression for CXCL12-δ (0.5%), ε (0.1%) and –φ (0.2%).

We compared CXCL12 isoform expression levels between cell lines with metastatic potential and those without metastatic potential (Figure 2.6), and found that CXCL12 and its α, β isoforms were expressed significantly lower in samples with metastatic potential,

which is in agreement with the trends of isoform expression in clinical samples. The same trend was seen with CXCL12- γ, though not statistically significant.

2.5 Discussion

While alternative splicing formerly appeared to be limited to a small number of genes, studies now demonstrate that almost all human genes undergo alternative splicing to create protein diversity [42]. Variants generated by loss of splicing fidelity or regulated transitions between isoforms drive cancer and many other human diseases, generating a large number of novel transcripts and proteins expressed predominantly or uniquely in cancer. For example, up to 36 different isoforms of the Wilms tumor gene 1 (WT1) have been identified with specific variants specifically upregulated in acute and chronic myeloid leukemias, suggesting key functions in cancer initiation and/or progression [43,44]. Similarly, isoforms of vascular endothelial growth factor (VEGF) exhibit distinct functional activities in tumor angiogenesis that vary based on anatomic site, emphasizing the importance of tumor environments on isoforms [45-47]. In addition to conferring unique functions to cancer cells and tumor environments, alternative splicing offers a rich source of potential prognostic and predictive biomarkers. Biomarkers and targeted therapies based on alternative splicing may have a higher likelihood for success than conventional approaches centered on a whole gene or protein. Collectively, these studies highlight the clinical relevance of identifying disease-associated changes in alternative splicing.

Prior research has established central functions of CXCL12 in cancer growth and metastasis, but very few studies have investigated isoforms of CXCL12 in cancer. In renal cell carcinoma, an analysis limited to CXCL12-α and -β revealed that only the β isoform correlated with tumor grade and infiltration of CD8 T cells [48]. CXCL12-β also was upregulated in bladder cancer, a disease in which expression of this isoform predicted metastasis and disease-specific mortality [49]. This study of bladder cancer also showed that amounts of CXCL12-α did not change between normal and malignant tissue, while CXCL12-γ was undetectable. Neither these studies nor any others have

investigated the other three CXCL12 isoforms (δ, ε, or φ) in cancer due to the lack of antibodies against these isoforms and limitations in high throughput technology.

Next-Gen sequencing allows our study to fill notable gaps in knowledge about the CXCL12/CXCR4/CXCR7 pathway by providing the first characterization of expression levels of all known alternative splicing variants of CXCL12 in breast cancer or any other malignancy. We found that primary human breast cancers express four different isoforms of CXCL12 in rank order of α > β > γ > δ, while ε and φ essentially were undetectable in the TCGA breast cancer samples. Expression of CXCL12 isoforms varied significantly across many different clinical and molecular categories of breast cancer, including stage, histologic type, intrinsic molecular subtype, and hormone receptor status. Changes in abundance of transcripts typically occurred in parallel for each CXCL12 isoform as would be expected for an mRNA regulated by the same common promoter elements. We also discovered lower levels of CXCL12 transcripts in subtypes of breast cancer regarded as more aggressive, such as triple-negative and Her2 amplified, and with progression to higher stage. These findings corresponded with Kaplan-Meier analyses, where low expression of CXCL12 and specific isoforms was associated with worse outcomes. We identified isoform-specific effects on MFS, RFS, and OS with low levels of CXCL12- α, -β and -γ significantly correlated with worse MFS and RFS. Most notably, we note that low levels of CXCL12-δ associated with worse OS and showed the same trend for RFS and MFS, despite the fact that CXCL12- δ expression does not correlate with expression of the other isoforms. This relationship is robust, and persists even after taking into account CXCL12, CXCR4, and CXCR7 expression in multi-gene analysis, indicating the independent prognostic significance of CXCL12- δ. These data provide the first evidence that CXCL12-δ is expressed in human cancer and correlate with a patient outcome.

Expression levels of CXCL12 in breast cancer cell lines generally mirror conclusions from the clinical samples that lower levels of CXCL12 correlate with worse prognosis. We found that breast cancer cell lines without metastatic potential (in mouse models) had higher levels of CXCL12 expression than cell lines that metastasize more widely.

Studies of CXCL12 in breast cancer focus on secretion of this chemokine by stromal cells in primary and metastatic sites, frequently overlooking effects of CXCL12 produced by cancer cells. However, epigenetic silencing of the CXCL12 promoter has been reported in breast cancer cells with greater metastatic potential, and re-expressing CXCL12 limits metastatic disease in mouse xenograft models [25]. Our analysis of cell lines may inform likely sources of various CXCL12 isoforms in tumor microenvironments. Breast cancer cells express CXCL12-α, β, and γ with very minimal expression of δ, which could indicate that stromal cells are the predominant source of the δ isoform in primary breast cancers. We also note that CXCL12-γ is higher than α and β in our panel of breast cancer cell lines, which is opposite the pattern in primary tumors. Differences between data from cell lines versus tumors may reflect dynamic regulation of CXCL12 isoforms *in vivo,* greater contributions of stromal cells to overall expression of CXCL12-α and β in breast tumors, or simply genomic changes as the original cancer samples were transformed into immortalized cell lines. In addition, CXCL12 levels within the tumor microenvironment may be affected by post-translational modification, such as cleavage by CD26 or matrix-metalloproteinase-2.[50,51]

Isoform-specific differences in expression and breast cancer outcomes suggest distinct functions of individual splice variants of CXCL12 on disease progression. Recent studies have begun to identify unique biochemical properties of CXCL12 isoforms, particularly α, β, and γ. While all isoforms share the same core structure, CXCL12-β, γ, δ, ε, and φ differ by inclusion of exons that add 4, 40, 51, 1 or 11 additional amino acids, respectively, to the carboxy-terminus of the molecule [24]. Particularly for CXCL12-γ, the added carboxy-terminal amino acids are enriched with basic residues that enhance binding to heparan sulfates and other negatively-charged extracellular matrix molecules [52]. By comparison, CXCL12-β and to a greater extent γ have reduced binding affinities for receptors CXCR4 and CXCR7. Biochemical differences in binding to receptors and extracellular matrix molecules translate to different functional outcomes. In mouse models, CXCL12-γ promotes chemotaxis of immune cells and endothelial progenitors to a significantly greater extent than other isoforms [53,54]. Greater binding to heparan sulfates and extracellular matrix molecules also limits proteolytic degradation of

CXCL12 [55]. These studies highlight functional differences among CXCL12 isoforms in receptor binding, chemotaxis, and stability that could alter outcomes in breast cancer. Our data also support further studies analyzing functional differences among CXCL12 isoforms, especially for CXCL12-δ.

Correlation between gene transcript data and protein expression is dependent on the gene and tissue type. However, mRNA expression is generally a good proxy for protein expression and is frequently used as biomarkers.[56-58] Gene expression also forms the basis of the PAM50 molecular subtyping of breast cancer as well as Oncotype Dx, a widely used predictive model for chemotherapy response in breast cancer.[59-62] Specifically for CXCL12- α, β, and γ, mRNA levels as measured by quantitative RT-PCR correlate with protein levels as measured by ELISA.[63] We also recognize that this study has limitations based on the data publicly available through the TCGA. While the data set contains transcript data for a large number of patients, the median follow-up time is relatively short, and therefore the number of metastasis and recurrence events is small, thus limiting our statistical power. This likely accounts for why the p-values for CXCL12- δ MFS and RFS do not reach significance. We also do not know the full treatment history for all patients, such as exact chemotherapy and radiation regimens, and there is likely significant heterogeneity in treatments given the multi-institutional nature of the data. Even with these limitations, we were able to identify significant differences in outcomes for isoforms of CXCL12.

In summary, our data reveal new associations of CXCL12, CXCR4, and CXCR7 gene expression with molecular, histologic, and clinical categories of human breast cancer. In addition, we have identified isoform-specific differences in CXCL12 for outcomes in breast cancer, suggesting distinct biochemical functions of isoforms in disease progression. These compelling results establish the foundation for mechanistic pre-clinical studies of these isoforms in breast cancer. Additional studies also are warranted to elucidate the biological and functional differences between the CXCL12 isoforms and validate them as potential biomarkers.

2.6 Tables

Table 2.1 Cancer patient characteristics compiled from TCGA

Mean Age (Years)	58.0 ± 13.3	*Median Follow-up* (Months)	23.7
Variable (n)		Variable (n)	
Estrogen Receptor		*Node Stage*	
Positive	579	0	361
Negative	170	1+	409
Progesterone Receptor		*Death*	
Positive	505	Positive	104
Negative	241	Negative	675
Her2 Receptor		*Recurrence*	
Positive	141	Positive	53
Negative	508	Negative	315
PAM50 Status		*Metastasis*	
Basal	138	Positive	48
Her2	66	Negative	324
Luminal A	414	*Gender*	
Luminal B	190	Female	776
Normal	24	Male	9
Overall Stage		*Menopause*	
1	127	Pre-	181
2	127	Post-	493
3	171	*Race*	
4	15	White	591
Tumor Stage		Black or African American	55
1	207	Asian	51
2	467	American Indian	1
3	76	or Alaskan Native	
4	32		

2.7 Figures

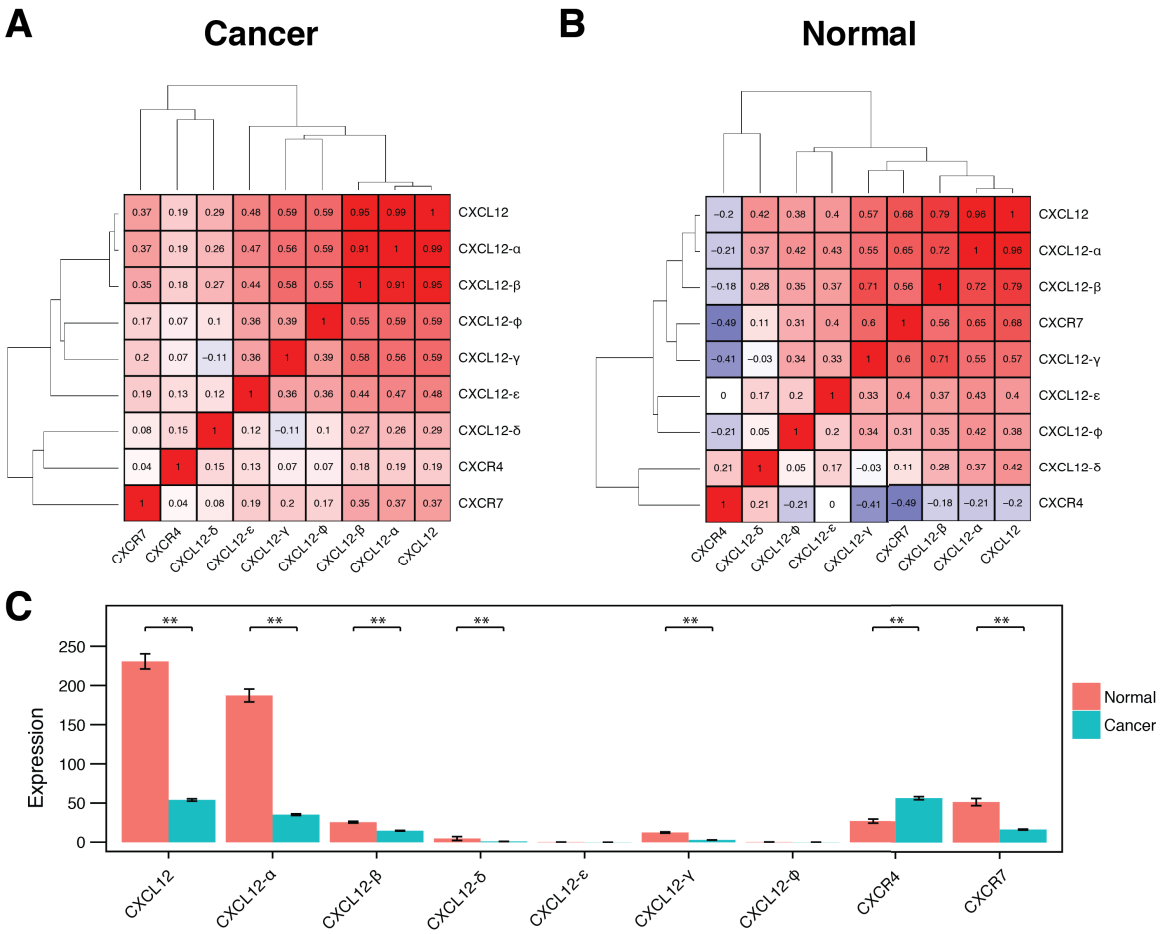

Figure 2.1 Hierarchal clustering and expression levels of CXCL12 isoforms, CXCR4, and CXCR7 in cancer and normal tissue

Spearman's covariance matrix with hierarchal clustering of CXCL12 isoforms, CXCR4, and CXCR7 for (A) breast cancer and (B) normal tissue. (C) Expression levels of CXCL12 isoforms, CXCR4, and CXCR7 in breast cancer and normal tissue. Expression levels are mean ± sem. *: $p<0.05$, **: $p<0.001$

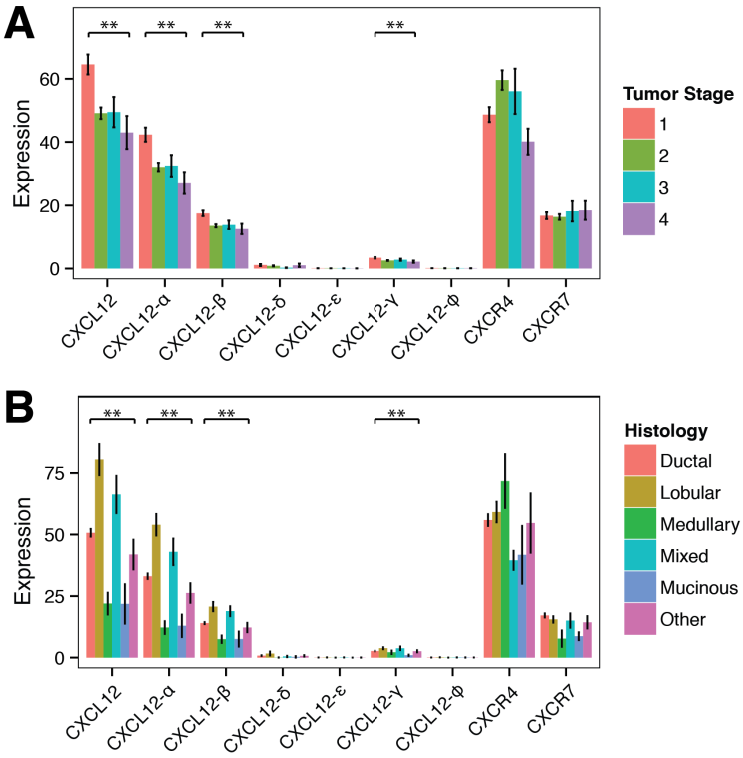

Figure 2.2 Expression levels of CXCL12 isoforms vary by tumor and histology

Expression levels of CXCL12-α, -β and –γ vary significantly by (A) tumor and (B) histology. Expression levels are mean ± sem. *: $p<0.05$, **: $p<0.001$

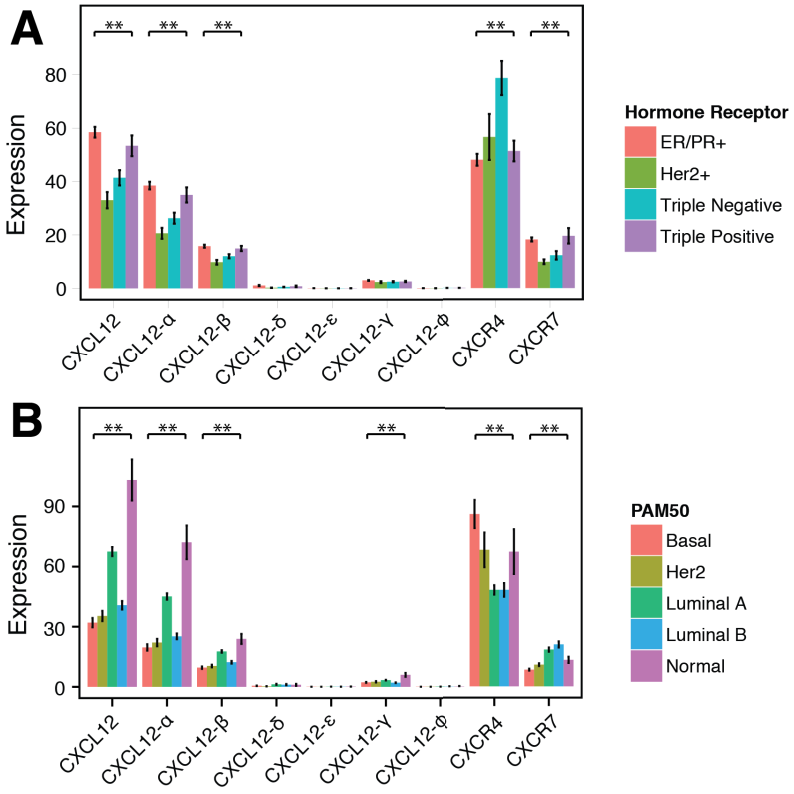

Figure 2.3 Expression levels of CXCL12 isoforms vary with hormone receptor status and molecular subtype

Expression levels of CXCL12 isoforms, CXCR4, and CXCR7 vary with hormone receptor status (A) and PAM50 molecular subtype (B). Expression levels are mean ± sem. *: $p<0.05$, **: $p<0.001$

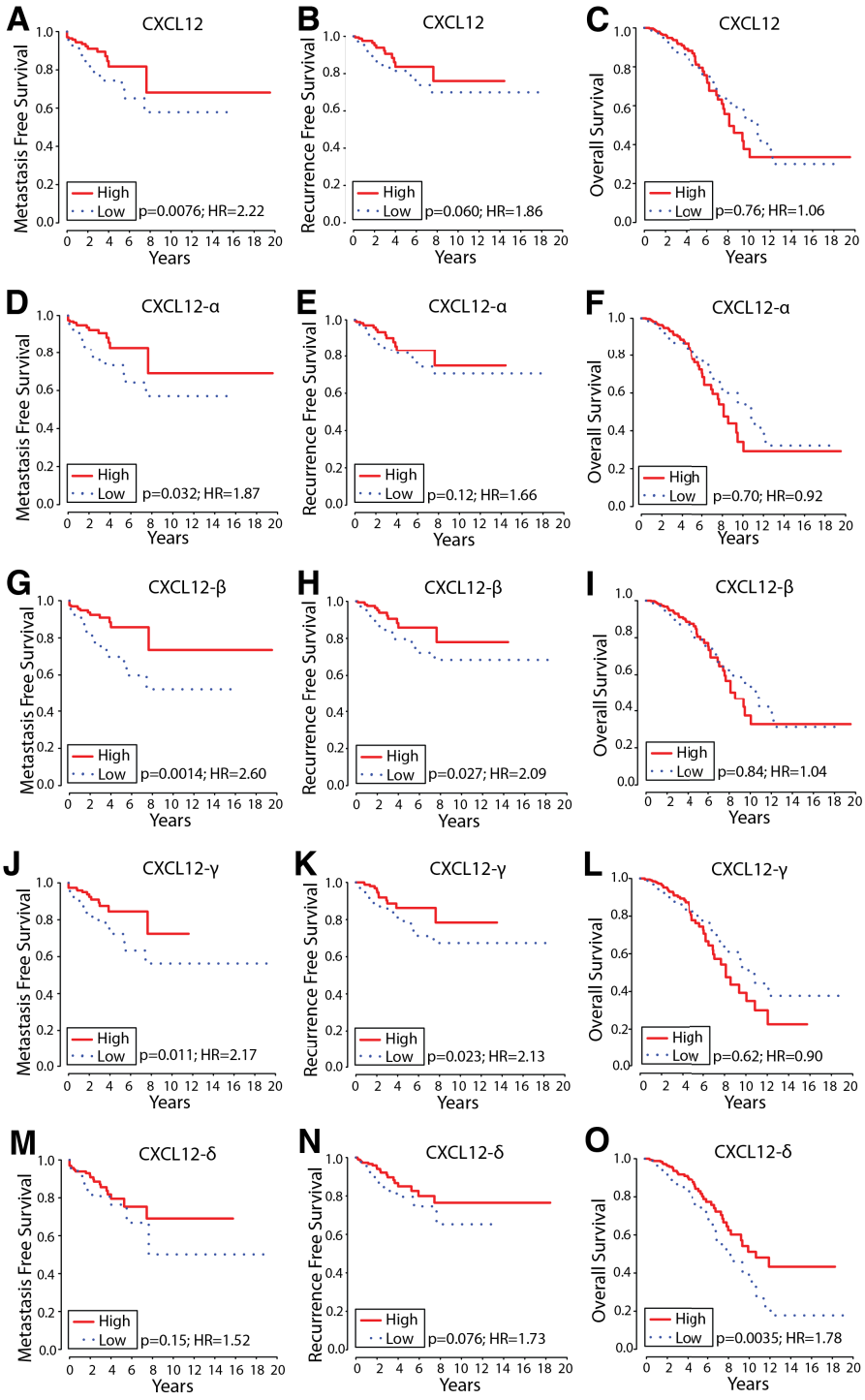

Figure 2.4 Metastasis free, recurrence free and overall survival curves for CXCL12 isoforms

Higher levels of gene-level CXCL12 (A-C), CXCL12-α (D-F), -β (G-I), –γ (J-L) generally correlate with improved metastasis free survival and recurrence free survival. Higher expression of CXCL12-δ (M-O) correlates with better overall survival.

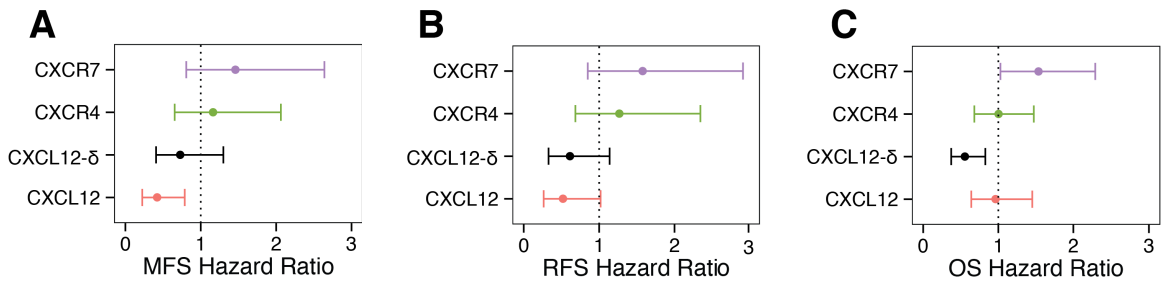

Figure 2.5 Multi-gene analysis for CXCL12-δ, gene-level CXCL12, CXCR4 and CXCR7

Multi-gene analysis reveals that expression of CXCL12-δ for MFS (A) and RFS (B) and OS (C) when accounting for gene-level CXCL12, CXCR4, and CXCR7. Error bars represent 95% confidence intervals.

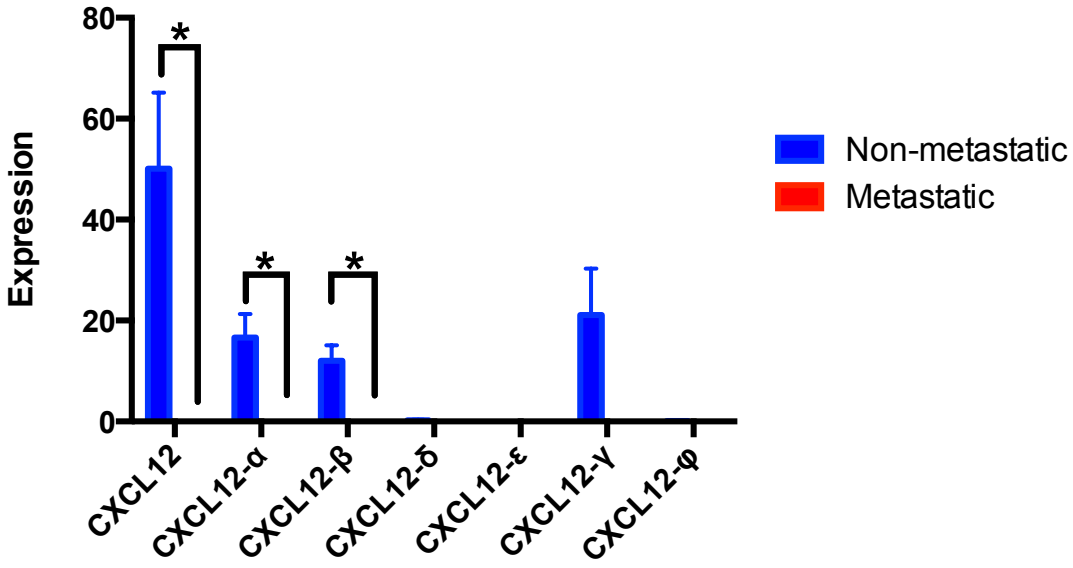

Figure 2.6 Expression of CXCL12 isoforms in breast cancer cell lines

Expression of gene-level CXCL12 and CXCL12-α and –β isoforms are significantly higher in cell lines without metastatic potential, compared to cell lines with metastatic potential. Expression levels are mean ± sem. *: $p<0.05$

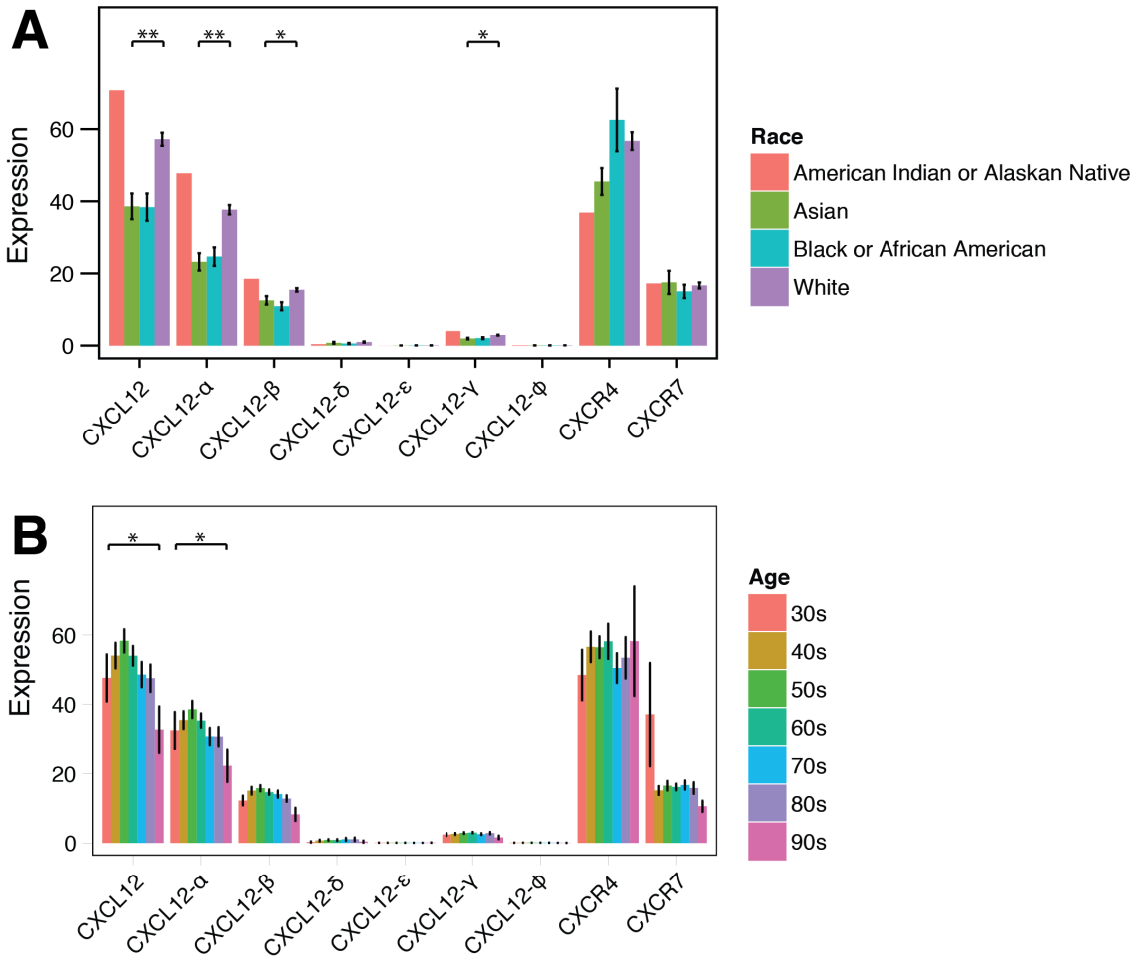

Figure 2.7 Expression of CXCL12 isoforms vary by race and age

(A) CXCL12 and its α, β, and γ isoforms vary significantly with race. (B) Overall CXCL12 and CXCL12-α vary significantly with age. Expression levels are mean ± sem. *: $p<0.05$, **: $p<0.001$

2.8 References

1. Wang ET, Sandberg R, Luo S, Khrebtukova I, Zhang L, et al. (2008) Alternative isoform regulation in human tissue transcriptomes. Nature 456: 470-476.
2. Oltean S, Bates DO (2013) Hallmarks of alternative splicing in cancer. Oncogene.
3. Zhang J, Manley JL (2013) Misregulation of pre-mRNA alternative splicing in cancer. Cancer Discov 3: 1228-1237.
4. Babic I, Anderson ES, Tanaka K, Guo D, Masui K, et al. (2013) EGFR mutation-induced alternative splicing of Max contributes to growth of glycolytic tumors in brain cancer. Cell Metab 17: 1000-1008.
5. Martin S, Jansen F, Bokelmann J, Kolb H (1997) Soluble CD44 splice variants in metastasizing human breast cancer. Int J Cancer 74: 443-445.
6. Schwerk C, Schulze-Osthoff K (2005) Regulation of apoptosis by alternative pre-mRNA splicing. Mol Cell 19: 1-13.
7. Christofk HR, Vander Heiden MG, Harris MH, Ramanathan A, Gerszten RE, et al. (2008) The M2 splice isoform of pyruvate kinase is important for cancer metabolism and tumour growth. Nature 452: 230-233.
8. Christofk HR, Vander Heiden MG, Wu N, Asara JM, Cantley LC (2008) Pyruvate kinase M2 is a phosphotyrosine-binding protein. Nature 452: 181-186.
9. Hofmann M, Rudy W, Zoller M, Tolg C, Ponta H, et al. (1991) CD44 splice variants confer metastatic behavior in rats: homologous sequences are expressed in human tumor cell lines. Cancer Res 51: 5292-5297.
10. Brinkman BM (2004) Splice variants as cancer biomarkers. Clin Biochem 37: 584-594.
11. Pajares MJ, Ezponda T, Catena R, Calvo A, Pio R, et al. (2007) Alternative splicing: an emerging topic in molecular and clinical oncology. Lancet Oncol 8: 349-357.
12. Duda DG, Kozin SV, Kirkpatrick ND, Xu L, Fukumura D, et al. (2011) CXCL12 (SDF1alpha)-CXCR4/CXCR7 pathway inhibition: an emerging sensitizer for anticancer therapies? Clin Cancer Res 17: 2074-2080.
13. Sun X, Cheng G, Hao M, Zheng J, Zhou X, et al. (2010) CXCL12 / CXCR4 / CXCR7 chemokine axis and cancer progression. Cancer Metastasis Rev 29: 709-722.
14. Teicher BA, Fricker SP (2010) CXCL12 (SDF-1)/CXCR4 pathway in cancer. Clin Cancer Res 16: 2927-2931.
15. Cabioglu N, Sahin A, Doucet M, Yavuz E, Igci A, et al. (2005) Chemokine receptor CXCR4 expression in breast cancer as a potential predictive marker of isolated tumor cells in bone marrow. Clin Exp Metastasis 22: 39-46.
16. Holm NT, Byrnes K, Li BD, Turnage RH, Abreo F, et al. (2007) Elevated levels of chemokine receptor CXCR4 in HER-2 negative breast cancer specimens predict recurrence. J Surg Res 141: 53-59.
17. Kang H, Watkins G, Parr C, Douglas-Jones A, Mansel RE, et al. (2005) Stromal cell derived factor-1: its influence on invasiveness and migration of breast cancer cells in vitro, and its association with prognosis and survival in human breast cancer. Breast Cancer Res 7: R402-410.
18. Muller A, Homey B, Soto H, Ge N, Catron D, et al. (2001) Involvement of chemokine receptors in breast cancer metastasis. Nature 410: 50-56.
19. Smith MC, Luker KE, Garbow JR, Prior JL, Jackson E, et al. (2004) CXCR4 regulates growth of both primary and metastatic breast cancer. Cancer Res 64: 8604-8612.
20. Miao Z, Luker KE, Summers BC, Berahovich R, Bhojani MS, et al. (2007) CXCR7 (RDC1) promotes breast and lung tumor growth in vivo and is expressed on tumor-associated vasculature. Proc Natl Acad Sci U S A 104: 15735-15740.
21. Naumann U, Cameroni E, Pruenster M, Mahabaleshwar H, Raz E, et al. (2010) CXCR7 functions as a scavenger for CXCL12 and CXCL11. PLoS One 5: e9175.
22. Rajagopal S, Kim J, Ahn S, Craig S, Lam CM, et al. (2010) Beta-arrestin- but not G protein-mediated signaling by the "decoy" receptor CXCR7. Proc Natl Acad Sci U S A 107: 628-632.
23. Burns JM, Summers BC, Wang Y, Melikian A, Berahovich R, et al. (2006) A novel chemokine receptor for SDF-1 and I-TAC involved in cell survival, cell adhesion, and tumor development. J Exp Med 203: 2201-2213.
24. Yu L, Cecil J, Peng SB, Schrementi J, Kovacevic S, et al. (2006) Identification and expression of novel isoforms of human stromal cell-derived factor 1. Gene 374: 174-179.

25. Wendt MK, Cooper AN, Dwinell MB (2008) Epigenetic silencing of CXCL12 increases the metastatic potential of mammary carcinoma cells. Oncogene 27: 1461-1471.
26. Zhang XH, Jin X, Malladi S, Zou Y, Wen YH, et al. (2013) Selection of bone metastasis seeds by mesenchymal signals in the primary tumor stroma. Cell 154: 1060-1073.
27. Allinen M, Beroukhim R, Cai L, Brennan C, Lahti-Domenici J, et al. (2004) Molecular characterization of the tumor microenvironment in breast cancer. Cancer Cell 6: 17-32.
28. Orimo A, Gupta PB, Sgroi DC, Arenzana-Seisdedos F, Delaunay T, et al. (2005) Stromal fibroblasts present in invasive human breast carcinomas promote tumor growth and angiogenesis through elevated SDF-1/CXCL12 secretion. Cell 121: 335-348.
29. Mirisola V, Zuccarino A, Bachmeier BE, Sormani MP, Falter J, et al. (2009) CXCL12/SDF1 expression by breast cancers is an independent prognostic marker of disease-free and overall survival. Eur J Cancer 45: 2579-2587.
30. Zhong C, Wang J, Li B, Xiang H, Ultsch M, et al. (2013) Development and preclinical characterization of a humanized antibody targeting CXCL12. Clin Cancer Res 19: 4433-4445.
31. (2012) Comprehensive molecular portraits of human breast tumours. Nature 490: 61-70.
32. Goldman M, Craft B, Swatloski T, Ellrott K, Cline M, et al. (2013) The UCSC Cancer Genomics Browser: update 2013. Nucleic Acids Res 41: D949-954.
33. Allan AL, George R, Vantyghem SA, Lee MW, Hodgson NC, et al. (2006) Role of the integrin-binding protein osteopontin in lymphatic metastasis of breast cancer. Am J Pathol 169: 233-246.
34. Chekhun S, Bezdenezhnykh N, Shvets J, Lukianova N (2013) Expression of biomarkers related to cell adhesion, metastasis and invasion of breast cancer cell lines of different molecular subtype. Exp Oncol 35: 174-179.
35. Matrone MA, Whipple RA, Thompson K, Cho EH, Vitolo MI, et al. (2010) Metastatic breast tumors express increased tau, which promotes microtentacle formation and the reattachment of detached breast tumor cells. Oncogene 29: 3217-3227.
36. Trapnell C, Pachter L, Salzberg SL (2009) TopHat: discovering splice junctions with RNA-Seq. Bioinformatics 25: 1105-1111.
37. Flicek P, Ahmed I, Amode MR, Barrell D, Beal K, et al. (2013) Ensembl 2013. Nucleic Acids Res 41: D48-55.
38. Trapnell C, Williams BA, Pertea G, Mortazavi A, Kwan G, et al. (2010) Transcript assembly and quantification by RNA-Seq reveals unannotated transcripts and isoform switching during cell differentiation. Nat Biotechnol 28: 511-515.
39. Perou CM, Sorlie T, Eisen MB, van de Rijn M, Jeffrey SS, et al. (2000) Molecular portraits of human breast tumours. Nature 406: 747-752.
40. Onitilo AA, Engel JM, Greenlee RT, Mukesh BN (2009) Breast cancer subtypes based on ER/PR and Her2 expression: comparison of clinicopathologic features and survival. Clin Med Res 7: 4-13.
41. Chu QD, Panu L, Holm NT, Li BD, Johnson LW, et al. (2010) High chemokine receptor CXCR4 level in triple negative breast cancer specimens predicts poor clinical outcome. J Surg Res 159: 689-695.
42. Pan Q, Shai O, Lee LJ, Frey BJ, Blencowe BJ (2008) Deep surveying of alternative splicing complexity in the human transcriptome by high-throughput sequencing. Nat Genet 40: 1413-1415.
43. Haber DA, Sohn RL, Buckler AJ, Pelletier J, Call KM, et al. (1991) Alternative splicing and genomic structure of the Wilms tumor gene WT1. Proc Natl Acad Sci U S A 88: 9618-9622.
44. Lopotova T, Polak J, Schwarz J, Klamova H, Moravcova J (2012) Expression of four major WT1 splicing variants in acute and chronic myeloid leukemia patients analyzed by newly developed four real-time RT PCRs. Blood Cells Mol Dis 49: 41-47.
45. Guo P, Xu L, Pan S, Brekken RA, Yang ST, et al. (2001) Vascular endothelial growth factor isoforms display distinct activities in promoting tumor angiogenesis at different anatomic sites. Cancer Res 61: 8569-8577.
46. Ladomery MR, Harper SJ, Bates DO (2007) Alternative splicing in angiogenesis: the vascular endothelial growth factor paradigm. Cancer Lett 249: 133-142.
47. Nowak DG, Amin EM, Rennel ES, Hoareau-Aveilla C, Gammons M, et al. (2010) Regulation of vascular endothelial growth factor (VEGF) splicing from pro-angiogenic to anti-angiogenic isoforms: a novel therapeutic strategy for angiogenesis. J Biol Chem 285: 5532-5540.
48. Wehler TC, Graf C, Altherr K, Zimmermann T, Brenner W, et al. (2011) SDF1beta expression in renal cell carcinoma correlates with grading and infiltration by CD8+ T-cells. Anticancer Res 31: 2797-2803.

49. Gosalbez M, Hupe MC, Lokeshwar SD, Yates TJ, Shields J, et al. (2013) Differential Expression of SDF-1 Isoforms in Bladder Cancer. J Urol.
50. De La Luz Sierra M, Yang F, Narazaki M, Salvucci O, Davis D, et al. (2004) Differential processing of stromal-derived factor-1alpha and stromal-derived factor-1beta explains functional diversity. Blood 103: 2452-2459.
51. Peng H, Wu Y, Duan Z, Ciborowski P, Zheng JC (2012) Proteolytic processing of SDF-1alpha by matrix metalloproteinase-2 impairs CXCR4 signaling and reduces neural progenitor cell migration. Protein Cell 3: 875-882.
52. Altenburg JD, Broxmeyer HE, Jin Q, Cooper S, Basu S, et al. (2007) A naturally occurring splice variant of CXCL12/stromal cell-derived factor 1 is a potent human immunodeficiency virus type 1 inhibitor with weak chemotaxis and cell survival activities. J Virol 81: 8140-8148.
53. Rueda P, Balabanian K, Lagane B, Staropoli I, Chow K, et al. (2008) The CXCL12gamma chemokine displays unprecedented structural and functional properties that make it a paradigm of chemoattractant proteins. PLoS One 3: e2543.
54. Rueda P, Richart A, Recalde A, Gasse P, Vilar J, et al. (2012) Homeostatic and tissue reparation defaults in mice carrying selective genetic invalidation of CXCL12/proteoglycan interactions. Circulation 126: 1882-1895.
55. Sadir R, Imberty A, Baleux F, Lortat-Jacob H (2004) Heparan sulfate/heparin oligosaccharides protect stromal cell-derived factor-1 (SDF-1)/CXCL12 against proteolysis induced by CD26/dipeptidyl peptidase IV. J Biol Chem 279: 43854-43860.
56. Vogel C, Marcotte EM (2012) Insights into the regulation of protein abundance from proteomic and transcriptomic analyses. Nature Reviews Genetics 13: 227-232.
57. Ghazalpour A, Bennett B, Petyuk VA, Orozco L, Hagopian R, et al. (2011) Comparative analysis of proteome and transcriptome variation in mouse. PLoS Genet 7: e1001393.
58. Schwanhausser B, Busse D, Li N, Dittmar G, Schuchhardt J, et al. (2011) Global quantification of mammalian gene expression control. Nature 473: 337-342.
59. Albain KS, Barlow WE, Shak S, Hortobagyi GN, Livingston RB, et al. (2010) Prognostic and predictive value of the 21-gene recurrence score assay in postmenopausal women with node-positive, oestrogen-receptor-positive breast cancer on chemotherapy: a retrospective analysis of a randomised trial. Lancet Oncol 11: 55-65.
60. Martin M, Prat A, Rodriguez-Lescure A, Caballero R, Ebbert MT, et al. (2013) PAM50 proliferation score as a predictor of weekly paclitaxel benefit in breast cancer. Breast Cancer Res Treat 138: 457-466.
61. Paik S, Tang G, Shak S, Kim C, Baker J, et al. (2006) Gene expression and benefit of chemotherapy in women with node-negative, estrogen receptor-positive breast cancer. J Clin Oncol 24: 3726-3734.
62. Prat A, Parker JS, Fan C, Perou CM (2012) PAM50 assay and the three-gene model for identifying the major and clinically relevant molecular subtypes of breast cancer. Breast Cancer Res Treat 135: 301-306.
63. Cavnar SP, Ray P, Moudgil P, Chang SL, Luker KE, et al. (2014) Microfluidic source-sink model reveals effects of biophysically distinct CXCL12 isoforms in breast cancer chemotaxis. Integr Biol (Camb).

Chapter 3 Cell, isoform, and environment factors shape gradients and modulate chemotaxis

3.1 Abstract

Chemokine gradient formation requires multiple processes that include ligand secretion and diffusion, receptor binding and internalization, and immobilization of ligand to surfaces. To understand how these events dynamically shape gradients and influence ensuing cell chemotaxis, we built a multi-scale hybrid agent-based model linking gradient formation, cell responses, and receptor-level information. The CXCL12/CXCR4/CXCR7 signaling axis is highly implicated in metastasis of many cancers. We model CXCL12 gradient formation as it is impacted by CXCR4 and CXCR7, with particular focus on the three most highly expressed isoforms of CXCL12. We trained and validated our model using data from an *in vitro* microfluidic source-sink device. Our simulations demonstrate how isoform differences on the molecular level affect gradient formation and cell responses. We determine that ligand properties specific to CXCL12 isoforms (binding to the migration surface and to CXCR4) significantly impact migration and explain differences in *in vitro* chemotaxis data. We extend our model to analyze CXCL12 gradient formation in a tumor environment and find that short distance, steep gradients characteristic of the CXCL12-γ isoform are effective at driving chemotaxis. We highlight the importance of CXCL12-γ in cancer cell migration: its high effective affinity for both extracellular surface sites and CXCR4 strongly promote CXCR4+ cell migration. CXCL12-γ is also more difficult to inhibit, and we predict that co-inhibition of CXCR4 and CXCR7 is necessary to effectively hinder CXCL12-γ-induced migration. These findings support the growing importance of understanding differences in protein isoforms, and in particular their implications for cancer treatment.

3.2 Introduction

Chemotaxis is a critical physiological and pathological process. Although cells only discern local differences in chemokine concentration via receptor binding, chemoattractant gradients may be maintained over distances much greater than a cell length. These long distance gradients provide a roadmap for leukocytes to reach sites of inflammation or cancer cells to invade and metastasize to distant organs. The simplest notion of chemotactic gradient formation involves secretion of soluble chemokines and diffusion away from their source. *In vivo* gradient formation is fundamentally more complicated and dynamic, involving multiple cell types, chemokine removal by receptors, and interactions with the physical migration "terrain". To therapeutically target gradient formation and chemotaxis, experimental and computational models are needed to facilitate observation, control, and prediction at all scales: molecular, cellular, and tissue.

Due to the challenge of visualizing and manipulating *in vivo* gradients, many chemotaxis model systems have been developed. Such systems, including Boyden chambers and microfluidic generators, supply stable, defined gradients, but these exogenous, applied gradients may not provide physiologically-relevant gradient formation. To bridge this gap, we recently highlighted an *in vitro* microfluidic source-sink device that exploits *cell-generated* gradients to drive chemotaxis [1,2] (Figure A.1). Here, we leverage these microfluidic device-based data to develop a computational model and predict which underlying molecular-scale events control *in vivo* gradient generation and ensuing chemotaxis.

The CXCL12/CXCR4 signaling axis is a prime example of how cellular and environmental factors form complex chemoattractant gradients that guide cells to distant locations. This signaling pathway has been implicated as a major driver of metastasis in multiple malignancies [3-8]. In breast cancer, CXCL12 is secreted by both carcinoma-associated fibroblasts and cancer cells in the primary tumor environment and is constitutively expressed in common sites of metastasis, such as bone, lung, and liver

[9,10]. CXCL12 has two known receptors, the G-protein coupled receptor CXCR4 and the atypical chemokine receptor CXCR7 (recently renamed ACKR3). CXCR4 binding to CXCL12 initiates survival, growth, and chemotaxis pathways [11]. Expression of the CXCR4 receptor, which is upregulated on cancer cells in both primary and metastatic tumors, mirrors that of CXCL12, suggesting that CXCR4-bearing cancer cells are actively guided by CXCL12 gradients to exit the primary tumor and metastasize to distant organs [12]. CXCR7 functions in part as a decoy receptor that scavenges and degrades ligand from the extracellular space [13]. CXCR7 is overexpressed on tumor-associated vasculature as well as on subsets of cancer cells in the primary tumor environment, and this receptor has been shown to lower overall CXCL12 levels in tumors [14,15]. Collectively, these receptor-based interactions between CXCL12, CXCR4, and CXCR7 only partially define the dynamic and complex signaling environment that drives chemotaxis.

Although receptor-based mechanisms of gradient formation and signaling are most well-known, ligand-specific effects may also dictate gradient shape. Much of the current knowledge on CXCL12/CXCR4 signaling focuses on the CXCL12-α isoform, as it is the most prevalent. However, other isoforms have been detected at lower expression levels. Studies of CXCL12 generally have overlooked the existence of six alternatively spliced isoforms (α, β, γ, δ, ε, and φ) that are comprised of an identical N-terminal core and vary by the addition of 1 to 41 largely basic amino acids at unstructured C-termini [16]. Both α and β isoforms have been detected in the primary tumor environment[10], and we recently identified CXCL12-γ in late stage cancer [1]. These isoforms have between 1 and 4 putative basic heparan sulfate binding domains, which affect how well isoforms bind to the migration surface and receptors and may also influence gradient stability and local concentrations [17-20]. Whether or not isoform-specific effects enhance or hinder migration is unclear.

To improve our understanding of how gradients are dynamically shaped and maintained and how cells interact with such gradients, we developed a multi-scale hybrid agent-based model. Multi-scale models have been used to explain emergent properties on the

tissue-scale that arise from individual cell decisions informed by the molecular-scale for a wide range of biological phenomena [21-23]. We used *in vitro* data on breast cancer cells migrating in a microfluidic source-sink device to train and validate the model and to predict gradient characteristics. We then used the model to ask: How do active cell properties, such as binding and internalization, shape the gradient? What are the factors that can explain different isoform abilities to elicit chemotaxis? Given what can be discovered in the device, how might these results be used to make predictions for a tumor environment?

Our simulations demonstrate that the decoy receptor CXCR7 dictates gradient magnitude and shape across the device environment due to its strong affinity for CXCL12. Despite a lower effective affinity of CXCL12 for CXCR4, CXCR4-expressing cells shape the local gradient at their leading edge and dynamically change the gradient as they move. In addition to these active-cell factors, simulations identify that properties of strong affinity for the migration surface and a high effective affinity for CXCR4 make the CXCL12-γ isoform a much stronger elicitor of chemotaxis than the α or β isoforms. Our model predicts that CXCR4+ cells move best in short distance, steep gradients that are characteristic of gradients of CXCL12-γ. Furthermore, we predict that blocking CXCR4 and CXCR7 receptors is less effective at inhibiting CXCR4+ migration in gradients of CXCL12-γ compared to the other isoforms. Importantly, these emergent properties still hold true in simulations of a tumor environment, indicating the potential importance of CXCL12-γ in enhancing chemotaxis in cancer.

3.3 Methods

3.3.1 Cell migration in a microfluidic source-sink device

All *in vitro* experimental data, except those used for model validation, are taken from our previous report of chemotaxis in an *in vitro* microfluidic source-sink device [1]. Briefly, MDA-MB-231 breast cancer cells were individually transduced to express recombinant CXCL12 isoforms (α, β, or γ), CXCR4, or CXCR7. Three cell types, cells secreting one of the CXCL12 isoforms (CXCL12+, source cells), CXCR4-expressing cells (CXCR4+), and CXCR7-expressing (CXCR7+) cells, were patterned in the microfluidic source-sink device. This pattern consisted of one stripe of CXCR4+ cells patterned between one stripe each of CXCL12+ and CXCR7+ cells. Each stripe of cells is 200 μm wide with 200 μm distance between each stripe [1,2] (Figure A.1). Chemotaxis was quantified by averaging the mean distance CXCR4+ cells moved towards the source cells after 24 hr compared to 0 hr. To manipulate ligand levels, portions of the CXCL12+ cells were replaced with non-secreting cells. These cell dilutions are represented as "Percentage of source cells secreting CXCL12." Parameters obtained directly from the *in vitro* source-sink device include dimensions of the microfluidic environment, cell density, cell patterning dimensions, and dilution of the number of secreting cells (Table A.1).

For this work, we obtained additional data for model validation using the microfluidic source-sink device. For these experiments, we increased gaps between the cell stripes from 200 μm to 400 μm (Figure A.1). Total receptor numbers were quantified using flow cytometry as described in [24] and are shown in Table A.2.

3.3.2 Multi-scale hybrid agent-based model overview

We constructed two variants of a multi-scale hybrid agent-based model of CXCR4+ chemotaxis in cell-generated CXCL12 gradients (Figure 3.1). We represent our microfluidic source-sink device environment (Figure A.1; [1]) with a 3D lattice. CXCL12+, CXCR4+, CXCR7+ cells are represented as discrete agents within the model and move in 2D on the bottom layer of the lattice, the "migration surface" (Figure 3.1A). We represent the *in vivo* tissue environment with a 2D grid. For both model variants, CXCL12 is secreted into the environment, diffuses and degrades in the extracellular

space, and binds to the migration surface and to CXCR4 and CXCR7 receptors. Receptor-mediated uptake of CXCL12 by CXCR4 and CXCR7 further shapes the gradient by removing ligand from the environment. Movement on the cellular-scale is dependent on gradient formation on the tissue-scale and receptor dynamics on the molecular-scale. These three scales are linked by a chemotaxis algorithm that governs CXCR4+ cell movement.

3.3.3 Model implementation

The model consists of two different layers: an environment layer and an agent layer. The environment is a grid that holds the information for all of the extracellular molecules (soluble and device-bound CXCL12). The agent layer contains the position and molecular-scale information (Table A.1b for all molecular species) for each agent. When an agent interacts with its environment (ie. ligand uptake), the extracellular ligand concentration is the value in the corresponding gridspace of the environment layer.

3.3.4 Model geometry

The chamber of the experimental microfluidic source-sink device is 20 mm x 2 mm x 0.1 mm (length x width x height) [1] (Figure A.1). In order to model gradient generation and cell movement within the microfluidic source-sink device while minimizing computational cost, we assume symmetry and model a 0.25 mm x 2 mm x 0.1 mm space using a 25 x 200 x 10 grid. The lattice spacing is 10 μm, approximately the size of a single cell, and thus only one cell is allowed to occupy each lattice space at any time. For CXCL12 diffusion, we implement no flux boundary conditions on the four sides that represent the top, bottom, left, and right edges of the device and periodic boundary condition on the front and back edges. Agents reside on the migration surface and move in 2D. For agent movement, we implement no flux boundary conditions on left and right edges, and periodic boundary conditions on the front and back edges. Implementation of these boundary conditions approximate both gradient generation and agent movement in the long microfluidic channel despite the shortened grid (Figure A.2).

For tumor-environment simulations, we use the same lattice framework, but with a 100 x 100 2D grid. We assume that the simulated tumor environment neighbors a similar

environment by implementing no flux boundary conditions on all four sides for diffusion and periodic boundary conditions on all sides for agent movement. To assess if gradient predictions in the 2D grid can be extrapolated to those in 3D gradients, we performed some pseudo-tumor simulations with a 100 x 100 x 5 grid, with no flux boundary conditions for diffusion on all sides.

3.3.5 Secretion and diffusion of soluble CXCL12

We assume a constant and uniform secretion rate per cell (rate constant: *CXCL12sec*); secreted ligands are deposited into the cell-containing compartment. To compare to experimental data, in some simulations we allow only a fraction of CXCL12 cells to secrete CXCL12. The overall secretion rate is the product of the number of secreting cells and the secretion rate constant. Diffusion of soluble CXCL12 (L) is described by the diffusion equation.

$$\frac{\partial [L]}{\partial t} = D\left(\frac{\partial^2 [L]}{\partial x^2} + \frac{\partial^2 [L]}{\partial y^2} + \frac{\partial^2 [L]}{\partial z^2}\right) \tag{3.1}$$

3.3.6 Binding of CXCL12 to migration surface

CXCL12 isoforms have different affinities for glycosaminoglycans ($\gamma > \beta > \alpha$), and we assume that the affinity of isoforms to the device surface is in the same order [19,20]. We use mass action kinetics and assume reversible binding of ligand (L) to sites on the migration surface (S) to calculate the concentration of ligand bound to the migration surface ($L \cdot S$):

$$\frac{d[L \cdot S]}{dt} = k_{f,L,S}([L][S] - K_{D,L,S}[L \cdot S]) \tag{3.2}$$

where $k_{f,L,S}$ is the forward rate constant for ligand binding to the surface site and $K_{D,L,S}$ is the equilibrium dissociation constant for the same (Figure 3.1B). We assume that ligand cannot bind surface sites that are currently occupied by a cell.

3.3.7 Extracellular degradation of CXCL12

CXCL12 undergoes protease-mediated degradation in cell media and in extracellular space[25,26]. For simplicity, we assume that extracellular degradation of soluble and surface-bound CXCL12 occurs with the same first-order kinetics (rate constant k_{deg}):

$$\frac{d[L]}{dt} = -k_{\text{deg}}[L] \tag{3.3}$$

$$\frac{d[L \cdot S]}{dt} = -k_{\text{deg}}[L \cdot S] \tag{3.4}$$

3.3.8 Receptor-mediated ligand uptake and dynamics

Receptor internalization and desensitization impacts chemotactic responses as well as gradient shaping, which are both influenced by receptor interactions with β-arrestin [27-31]. To focus on the effects of cell-based gradient shaping, we implement ordinary differential equations (ODEs) based on mass action to describe molecular-scale events for CXCR4+ (Figure 3.1C) and CXCR7+ cells (Figure 3.1D). These equations describe ligand binding to receptor, receptor binding to β-arrestin, internalization of β-arrestin-bound complexes, receptor and β-arrestin recycling, and receptor and ligand degradation. The ODEs that describe these events were constructed and validated in previous work ([32] and Tables A.1b-f). We consider the effective affinity of ligand for receptor to account for binding affinities for the receptor itself and glycosaminoglycans on the cell surface. There are two key differences between CXCR4 and CXCR7 dynamics: (1) β-arrestin binds transiently to CXCR4, whereas it binds tightly to CXCR7, and (2) CXCR4 degradation is ligand-induced, whereas CXCR7 is constitutively recycled (Figure 3.1C-D). Prior to simulation, these CXCR4 and CXCR7 ODEs are solved in the absence of ligand to determine the number of unbound β-arrestin and surface and internalized receptors per cell at steady state, and cells with these quantities are placed on the grid. We did not incorporate other aspects of CXCL12/CXCR4/CXCR7 signaling, such as ligand dimerization and receptor homo- and heterodimers, as there is very limited information on the kinetics of these processes and our previous work showed that they are not required to adequately describe ligand binding and internalization [32]. Dimer formation occurs at a much smaller time scale than ligand-receptor dynamics and dimers are relatively stable over the experimental time frame [33-36], indicating that including kinetics of dimer formation in the model may not be necessary. We did not include CXCR7 signaling, as the migrating cells do not express CXCR7 [2]. Our focus on the model is on the effects of cell-generated gradients, and prior studies also show that

chemokine scavenging by CXCR7 on sink cells is sufficient for gradient formation [37-39].

3.3.9 Random cell movement

Cells move in 2D on the surface of the device or in the tissue environment. At each movement time step, we calculate the next location for each agent. An agent can move to any of the eight lattice spaces in its Moore neighborhood or stay in its current space. To implement random movement for CXCL12+ and CXCR7+ cells, each of the nine lattice spaces is assigned an equal probability for movement. From these individual probabilities, we calculate a cumulative probability distribution that sums to 1. A random number between 0 and 1 is chosen, and the agent moves into the lattice space corresponding to that probability, if the chosen lattice space is empty. Otherwise it remains in its current lattice space. This type of simple random movement algorithm has been employed in numerous models (e.g. [40-43]).

3.3.10 Chemotaxis algorithm

To replicate experimental *in vitro* data, we needed to capture the motion of hundreds of individual cells over a 24 hr time period in response to a changing chemokine gradient. Specifically, we wanted to understand the role of receptor binding and internalization in that process. For computational tractability we chose a coarse-grained representation where chemotaxis is implemented as a movement probability defined by receptor occupancy and the number of CXCR4 surface receptors.

We build on previous models by assuming that cells sense gradients by comparing differences in receptor occupancy across their length [44-50] and implement this assumption on the discretized environment by calculating the projected receptor occupancy (*RO*) [50,51] for each lattice space in the Moore neighborhood of a CXCR4+ cell (including its current space):

$$RO = \frac{[C]}{[C] + K_{D,R4,L12}} * \frac{(surfaceCXCR4)}{9}, \qquad (3.5)$$

where *[C]* is the sum of soluble and surface-bound ligand concentration in that lattice space [52-55], $K_{D,R4,L12}$ is the equilibrium dissociation constant for ligand binding to CXCR4, and *surfaceCXCR4* is the total number of CXCR4 receptors on the cell surface of the agent. We assume a uniform distribution of receptors on the cell surface, and thus 1/9 of the total surface receptors are available to sense concentrations in any of the 9 lattice spaces [56].

To translate differences in receptor occupancy to probability intervals, we first calculate

$$dRO_i = \frac{RO_i - \min + s}{\sum_{i=1}^{9} RO_i - \min + s}, \qquad (3.6)$$

where RO_i is the projected receptor occupancy of the i^{th} lattice space, *min* is the minimum *RO* of the neighborhood and *s* is a chemotaxis sensitivity factor, representing the difference in *RO* to which a cell is sensitive. The sensitivity factor allows cells to respond to absolute differences in receptor occupancy, as opposed to relative differences in receptor occupancy. Similar to the procedure for CXCL12+ and CXCR7+ cells, the dRO_i values are normalized to 1, the cumulative probability distribution is created, and the agent moves into the lattice space corresponding to a random number chosen from 0 and 1 if the chosen lattice space is empty. If $K_{D,R4,L12} >> [C]$, or if $K_{D,R4,L12} << [C]$ then the calculated receptor occupancy values are similar and cells move essentially randomly.

The inclusion of the chemotaxis sensitivity factor *s* implements the assumption that chemotaxis is dependent on the number of cell surface receptors present at the time of movement [50,56-58]. We implement *s* as a decreasing linear function of the number of available surface chemokine receptors:

$$s = m \times surfaceCXCR4 + b, \qquad (3.7)$$

where *m* is the slope, *b* is the y-intercept, and *surfaceCXCR4* is as described above. These sensitivity parameters are fit to experimental data. While *s* is not limited to this form, model variants without this simple dependence on receptor number were unable to capture cell migration behavior in device experiments. When the number of available surface chemokine receptors is small, *s* is much greater than the difference in receptor occupancy, and the resulting probability intervals are similar and movement is random.

As the number of available surface chemokine receptors increases and *s* approaches zero, chemotaxing cells move based on differences in receptor occupancy alone.

3.3.11 Initial cell positions

The simulation grid is initialized with CXCL12+, CXCR4+, and CXCR7+ cells. For device simulations, cells are positioned randomly in stripes, with space in between where no cells are seeded (Figure A.1, Figure 3.1, Figure 3.2A) with a density of 2500 cells/mm^2, as they are experimentally. For tumor-like simulations, we base cell patterns on histological data from primary breast tumors. Both CXCR4+ cancer cells and CXCL12+ stromal cells typically are in clusters of 4-5 cells [10,14]. CXCR7+ cells in the tumor environment appear more randomly placed [15]. We determined cell densities by counting the number of CXCL12+, CXCR4+ or CXCR7+ cells in an image frame and divided by the total number of cells within the same frame. In accordance with these images, we initialized tumor-like simulations by randomly placing clusters of CXCL12+ and CXCR4+ cells and individual CXCR7+ cells on the grid. While limited to representative examples of primary breast cancers, these data provide qualitative insights into cell arrangements in human tumors.

3.3.12 Numerical solution

The overall algorithm of the simulation is depicted in Figure A.3. We use the principle of operator splitting to solve the simultaneous events of diffusion, degradation, and reactions [59-64]. Briefly, this method reduces the diffusion, extracellular binding and degradation, and molecular-scale reaction events to a partial differential equation, linear first order ordinary differential equations, and sets of ordinary differential equations for each lattice space and agent as described above. Within the model workflow, we simulate cell movement using a six minute movement time step over the 24 hr experimental set up, for a total of 240 timesteps. The six minute movement time step was determined by fitting the spread of randomly moving cells to experimental data of CXCR4+ cells moving in the absence of ligand (Figure A.4). Ligand secretion, diffusion, degradation and ligand binding to the migration surface are calculated using 0.1 second timesteps. ODEs depicting receptor-ligand dynamics are solved for each agent using a fourth-order Runge Kutta numerical solver with 0.01 second timesteps. The diffusion and ODE time

steps are the maximum time step allowable for solver stability. We use the alternating-direction explicit (ADE) method to solve diffusion as described in previous work [60,61].

3.3.13 Uncertainty and sensitivity analysis

We use Latin Hypercube Sampling (LHS) and Partial Rank Correlation Coefficients (PRCC) to identify parameters that have a significant effect on model output. LHS is a stratified non-replacement sampling strategy where all parameters are varied simultaneously [65,66]. PRCC values are calculated to determine how well the variability of a parameter correlates to a selected model output. PRCC values are between -1 and 1, which are associated with a perfectly negative or perfectly positive correlation between the parameter and model outcome.

To determine how molecular scale events dictate CXCR4+ chemotaxis, we performed sensitivity analyses by varying CXCR4 and CXCR7 kinetic parameters. We used LHS to generate 100 parameter sets, where each parameter was ranged over its known literature values (Tables A.1c-d). Each set was replicated 10 times to get an average value to perform PRCC analysis.

3.3.14 Parameter estimation, model fitting and validation

When possible, we use experimental data to determine model parameters. Kinetic and equilibrium parameters for CXCR4 and CXCR7 ODEs are the same as previously published, unless otherwise noted [32] (Tables A.1c-d). When unavailable, we estimate parameters with values restricted within ranges reported from literature. To determine the isoform-specific effective equilibrium dissociation constant to CXCR4, the equilibrium dissociation constant for binding to the migration surface, secretion rate constant, and m and b that define the chemotaxis sensitivity factor, we fit the model to experiments measuring CXCR4+ cell migration for each of three CXCL12 isoforms and for several different rates of ligand secretion. The initial estimate for the effective equilibrium dissociation constant to CXCR4 of CXCL12-α was set to the value used in our previously published ODE model; and we assumed that CXCL12 isoforms with higher numbers of heparan sulfate binding domains [17-20] would have higher affinities. The initial estimates for equilibrium dissociation constant for binding to the migration surface of

each CXCL12 isoform to the migration surface are based on their reported affinities to heparan sulfate [19]. The initial estimates for isoform-specific secretion rates are based on previously reported experiments using ELISA and bioluminescence-based measurements [1]. We used LHS to generate 100 random parameter sets, ran each parameter set for 20 replications, and chose the parameter set that minimized the squared error between model and experimental data. To validate these isoform-specific fitted parameters, we ran the model for the case where CXCL12+ and CXCR7+ cells are spaced further from the CXCR4+ cells.

3.3.15 Statistics

All plots and statistical comparisons were created with GraphPad Prism (La Jolla, CA). We plot simulation data as the mean of 30 replications with standard deviation. Additional replications beyond 30 did not significantly change the mean or standard deviation.

3.4 Results

3.4.1 Multi-scale hybrid agent-based model tracks ligand concentration, cell locations, and molecular-scale information

Using an *in vitro* microfluidic source-sink device dependent on cell-generated gradients to prompt chemotaxis, we previously determined that the strength of CXCR4-mediated chemotaxis is differentially impacted by CXCL12 isoforms and is increased when in the presence of its scavenger receptor, CXCR7 [1,2]. We hypothesized that this is due to gradient shaping mechanisms that are impacted by isoform-specific secretion rates, ligand binding to surfaces and the rate of ligand scavenging by CXCR7. To quantify these underlying molecular events and how they control gradient shaping and cell responses to chemotaxis, we developed a hybrid agent-based model that links molecular scale interactions to cell population (or tissue) scale outcomes. The model calculates the chemokine concentration gradient over time and position as it is influenced by cell secretion, diffusion and external degradation, receptor-ligand dynamics on moving cells, and binding to the migration surface. Here we present model outputs using the physiological parameters noted in Table A.1.

At the start of simulation, CXCL12+, CXCR4+ and CXCR7+ cells are placed in an environment that lacks ligand (Figure 3.2A). The model allows us to analyze which molecular-scale events dominate over time. At early times, diffusion and surface binding control the CXCL12 gradient (Figure A.5, panels A-C). At later times, ligand removal by CXCR4 and CXCR7 dynamics are crucial to controlling gradient magnitude and shape; however, they control the gradient at different length scales. CXCR7 is an effective scavenger that binds to CXCL12 with a much greater affinity than CXCR4 [67]. This high affinity for CXCL12 allows CXCR7 to significantly reduce the overall magnitude of CXCL12 concentration in the device and can alter the gradient over distances on the order of millimeters. In contrast, CXCR4 also depletes CXCL12 levels, but primarily in the region where CXCR4+ cells are located (Figure A.5, panels D-F). Sensitivity analysis identified that ligand binding and internalization by CXCR4 and CXCR7 have significant impact on CXCR4+ migration and overall CXCL12 concentration (Table A.3). The contribution of soluble and surface-bound CXCL12 to the total gradient can also be assessed. Most ligand is bound to the migration surface, despite the fact that the affinity of ligand to surface is relatively low (100nM), because there are many surface sites (Figure 3.2B).

As cells move on the grid, the model dynamically updates molecular scale information. As CXCR4+ cells spend more time in rising CXCL12 levels, ligand binding induces receptor internalization and degradation, resulting in decreasing receptor number over time and position within the device (Figure 3.2C). Simulations predict that significant losses of surface receptors can occur even at low ligand concentrations. In this representative example, the CXCR4+ cells at the furthermost left and right edges of the device have a difference of ~99,000 surface receptors (a 20% decrease between the rightmost and leftmost cells) at the end of simulation. Much of chemotaxis literature demonstrates chemotaxis in gradients of which cells move, but do not modify, yet we predict that cells actively shape their gradient as they move. As CXCR4+ cells advance towards the source cells, ligand binding, internalization and degradation result in gradient shifting along with the CXCR4+ cells (Figure 3.2D). Thus, our model captures experimentally observed phenomena and gives mechanistic and molecular insight into

chemotaxis. Furthermore, the model offers insight on the differences in contributions of CXCR4 and CXCR7 to the ligand gradient across position and time.

3.4.2 Migration in cell-generated gradients is dependent on isoform-specific properties

CXCL12 isoforms have different abilities to generate chemotaxis within the source-sink device. Our experimental data measuring CXCR4+ migration towards the source cells [1] are reproduced in Figure 3.3A-C. Notice that with 100% of source cells secreting, gradients of CXCL12-γ can elicit greater migration than gradients of CXCL12-β and CXCL12-α (CXCR4+ migration at 100% secretion, CXCL12-α: 39.6 μm ± 24.3; CXCL12-β: 46.1 μm ± 26.6; CXCL12–γ: 65.7 μm ± 35.5, ordinary one-way ANOVA P-value < 0.0001). CXCL12 isoforms also differ in their migration curves. CXCR4+ migration in gradients of CXCL12-α does not significantly change even when the percentage of secreting cells is decreased by two orders of magnitude, but presents a bell-shaped curve for CXCL12-β and significantly decreases when secretion is diluted to 1% for CXCL12-γ. We hypothesized that four isoform-specific parameters impact migration – secretion rate, affinity for the migration surface, effective affinity for CXCR4, and the chemotaxis sensitivity factor (*s*) – and fit these model isoform-specific parameters to data on CXCR4+ migration for each of the CXCL12 isoforms across the different secretion rates (Figure 3.3A-C).

It has been previously noted that CXCL12-γ has a markedly lower secretion rate than the α and β isoforms and a much higher affinity to cell surfaces (due to strong binding to glycosaminoglycans) [1,19,20]. As expected, the fit parameters have secretion rates in the order of α>β>>γ and affinities to the migration surface of γ>>β>α (Table 1). Initially, we refrained from varying the effective ligand affinity for CXCR4 and the chemotaxis sensitivity factor parameters, as differences among isoforms are not well established. However, a reasonable fit for CXCL12-γ data was not possible without increasing the effective affinity of CXCL12-γ to CXCR4 as well as slightly decreasing the slope (*m*) of the chemotaxis sensitivity factor (resulting in more sensitive migration) for the CXCL12–γ isoform. Although measurements of CXCL12 isoform binding determined that the affinity of CXCL12-γ to CXCR4 is lower than the other isoforms [20], it has been suggested that the high affinity by which CXCL12–γ binds to cell-surface heparan

sulfates may confer a higher effective affinity to CXCR4 than the other isoforms [17]. Limited data show differences in signaling between isoforms, and indicate that binding of the γ isoform to CXCR4 elicits more β-arrestin signaling than the other isoforms [1,17,68]. The fitted values for ligand affinity to the migration surface and secretion rate constants between isoforms are in accordance with experimental data [1,17,19].

Next, we predicted the effect of increasing the distance between the initial cell positions for all three CXCL12 isoforms on CXCR4+ migration (Figure 3.3D). Compared to migration using 200 μm spacing, CXCR4+ migration using 400 μm spacing is reduced for all isoforms. We then used the *in vitro* source-sink device under these conditions to measure the average CXCR4+ migration and found that the model predictions agree well with experimental data. Thus, our model accurately describes migration in our microfluidic source-sink device based on isoform-specific differences, placement of cells, and a broad range of CXCL12 secretion. In addition, the fitted parameters support that isoforms differ in their binding to the surface, binding to CXCR4, secretion rates, and sensitivity to movement, with the CXCL12–γ in particular displaying a much higher affinity to the migration surface and effective affinity to CXCR4 compared to the other isoforms.

3.4.3 Non-specific and receptor binding are both critical to migration

Because our computational model suggested that isoforms differ in binding to the migration surface and to CXCR4, we varied these two parameters to explore how ligand properties affect the chemokine gradient and subsequent chemotaxis. Increasing ligand affinity to the migration surface (decreasing $K_{D,L,S}$) creates steeper gradients and results in an upward shift of the chemotaxis curve (Figure 3.3E). Increased affinity to the migration surface can explain why CXCR4+ cells move furthest in gradients of CXCL12-γ, followed by –β, then –α at 100% secretion. Examination of the CXCL12 gradients reveals that despite lower secretion rates, gradients of CXCL12-β and –γ have higher overall concentrations and steeper gradients due to enhanced binding to the migration surface (Figure A.6). Increasing the ligand effective affinity to CXCR4 results in an upward shift of the chemotaxis curve (Figure 3.3F). As ligand effective affinity to CXCR4 increases (decreasing $K_{D,R4,L12}$), cells chemotax more efficiently in lower

concentrations. However, at higher concentrations, surface receptors are downregulated, reducing migration. Together with secretion rate, effective affinity for CXCR4 can explain the isoform-specific chemotaxis curve shapes. CXCL12-α has a low effective affinity to CXCR4 and mid-level secretion rate constant (20 molecules/cell-s) resulting in a relatively flat chemotaxis curve. We could not reproduce the steep bell-shaped curve for CXCL12-β, but note the large error bars for the 10% condition. (A lower secretion rate combined with a high affinity to CXCR4 - outside current literature ranges - would achieve a bell-shaped curve.) Finally, CXCL12-γ is secreted at a low rate and has a high effective affinity for CXCR4. The significant decrease at 1% secretion compared to 100% is due to its high effective affinity for CXCR4 resulting in maximal chemotaxis of the CXCL12-γ at 100%, and then a drop off at 1% due to low levels of ligand. These findings confirm that isoform-specific differences in binding to both the migration surface and to CXCR4 significantly control CXCR4+ migration.

3.4.4 Migration is sensitive to the number of CXCR4 receptors, and less sensitive to CXCR7

Potential therapeutic strategies for reducing chemotaxis include blocking CXCR4 or CXCR7 [57,69]. Using CXCL12-α-like parameters listed in Table A.1a (and determined above), we find that migration is sensitive to the number of CXCR4 and less so to the number of CXCR7 receptors. Blocking as few as 25% of CXCR4 receptors is sufficient to completely inhibit migration at low secretion rates, but is less effective at inhibiting migration at higher secretion rates (Figure 3.4A). Stronger inhibition of migration across all secretion rates requires blocking more than 50% of CXCR4 receptors. In contrast, nearly all CXCR7 receptors (90-99%) must be blocked to effectively reduce CXCR4+ cell migration at high secretion rates (Figure 3.4B). Note that due to the high starting numbers of receptors in the transfected cells modeled in the simulation, 50% blocking of CXCR4 and 90% blocking of CXCR7 correspond to ~10^5 available receptors per cell (3.55×10^5 and 2×10^5 receptors per cell for CXCR4 and CXCR7, respectively). Cancer cells have on the order of $10^3 – 10^5$ receptors per cell [70,71]. Clearly strong inhibition of migration is difficult with receptor numbers on the higher end of the range, but may require a smaller percentage of receptors to be blocked to effectively reduce migration on the lower end of the range. Blocking CXCR7 has a greater effect on CXCR4+ migration

at high secretion rates and a smaller effect on CXCR4+ migration at lower secretion rates, which is consistent with our *in vitro* data using CXCR7+ cells unable to internalize CXCL12-CXCR7 complexes [1]. At lower secretion rates, the gradient is primarily controlled by diffusion and ligand binding to the migration surface and CXCR7 has little effect. At high secretion rates, CXCR7 plays a significant role in diminishing the overall concentration in the device and limiting CXCR4 internalization (Figure A.7). By blocking both CXCR4 and CXCR7, migration can be inhibited across all secretion rates (Figure 3.4C), suggesting that a combination of CXCR4 and CXCR7 blocking may work as a treatment strategy to effectively hinder migration.

3.4.5 Inhibition of CXCR4+ migration is isoform-specific

Next, we examined if inhibition of CXCR4+ cell migration by blocking CXCR4 or CXCR7 is isoform-specific. We already established that high ligand affinity to the migration surface or to CXCR4, which is characteristic of the γ isoform, elicits higher CXCR4+ cell migration (Figure 3.3). Blocking 50% of CXCR4 receptors is effective at reducing migration across secretion rates for ligand with higher affinity to the migration surface as well as higher affinity to CXCR4 (Figure 3.4D), but not as well as with lower affinities to the surface or to CXCR4 (CXCL12-α-like). Furthermore, model simulations blocking CXCR7 with isoforms having elevated affinities to the migration surface and to CXCR4 reveal that the role of CXCR7 in modulating migration may also be isoform-specific (Figure 3.4E). Although blocking 90% of CXCR7 markedly decreases migration for the CXCL12-α-like parameters, it has much less of an effect in modulating migration for ligand with higher affinities to the migration surface and to CXCR4, further highlighting the potential importance of understanding the role of high affinity ligands like CXCL12-γ within the tumor environment. Two questions arise from these *in vitro* and *in silico* studies: do isoform gradients form in the tumor environment and what is the effect on CXCR4+ cell migration?

3.4.6 Gradients produced by tumor-like cell arrangements

We have focused up to this point on cell migration observed in our microfluidic source-sink device, where cells are initially arranged in stripes. We next wanted to explore the implications of our findings for gradient formation and cell migration in a more tumor-

like environment. To do this, we patterned cells to mimic the disorganization of CXCL12+, CXCR4+, and CXCR7+ cells observed in invasive breast cancer. We arranged CXCL12+, CXCR4+ and CXCR7+ cells on the simulation grid based on histological data (Figure 3.5A) [10,14,15]. For our initial set of simulations, all cells were immobile and we focused on generation of chemokine gradients within a 24 hr time period.

We first examine gradients using the same parameter values and receptor numbers as in the device (Table A.1). Predicted gradients at 24 hr are shown in Figure 3.5B-D for the three isoforms. Similarly to the microfluidic source-sink device (Figure A.6), gradients of CXCL12-β (Figure 3.5C) and -γ (Figure 3.5D) are steeper and have higher maximum concentrations than gradients of CXCL12-α. When CXCR7 is removed from the grid (Figure 3.5E-G), gradients for all isoforms become more diffuse, but have the most change for CXCL12-α and CXCL12-β. As CXCR7 has the most influence in gradient shaping when the ligand affinity for the extracellular space is low and when secretion rates are high, CXCR7 is more necessary to shape gradients of CXCL12-α and CXCL12-β than that of CXCL12-γ.

The simulations in Figure 3.5B-G used receptor numbers characteristic of the transfected cell lines used in our microfluidic source-sink device experiments (CXCR4, $7.1x10^5$; CXCR7, $2x10^6$). Next, we ran simulations to predict gradients for lower receptor levels ($5x10^3$ receptors/cell) that represent the lower range of receptor overexpression in cancer (Figure 3.5H-J) [70,71]. Gradients predicted for receptor numbers in this pathological range are similar to gradients predicted for environments that lack CXCR7. We note that CXCR4+ and CXCR7+ cells are able to produce micrograd ients, as they internalize ligand in the lattice space where they are placed (highlighted by the Inset of Panel I). These model predictions show that qualitative differences between gradients of CXCL12 isoforms determined in the microfluidic source-sink device hold true in the more disorganized cell arrangements found in tumors, and that secretion rates and ligand binding to the migration surface controls gradient shape and scope.

3.4.7 Steep short-distance gradients provide better homing than shallow long-distance gradients

Continuing with the parameters relevant to receptor overexpression in cancer (as in Figure 3.5H-J), we allowed CXCR4+ cells to move (Figure 3.6). We quantified chemotaxis by normalizing the number of CXCR4+ cells within 30 μm of a CXCL12 cluster at 24 hr to the number at the start of simulation. Similarly to the microfluidic source-sink device, we find that CXCR4+ cells move best in gradients of CXCL12-γ, followed by CXCL12-β, and CXCL12-α. The shallow long-range gradients of CXCL12-α do not promote migration in this cell arrangement and for these low receptor numbers; however, using a higher number of total receptors results in increased migration of CXCR4+ cells in CXCL12-α gradients (Figure A.8), indicating that gradients formed with CXCL12-α-like properties can induce chemotaxis when combined with increased receptor signaling. We also explored which isoform-specific parameters are most responsible for increased migration in gradients of CXCL12-β and –γ by systematically replacing one of the ligand-related parameters of CXCL12-α for that of γ (Figure A.8). Similarly to the device simulations, we found that increased effective affinity for CXCR4 and for the migration surface promotes CXCR4+ chemotaxis towards CXCL12 producing cells. Higher migration in gradients of CXCL12-γ and -β also mirror higher levels of surface CXCR4. The average number of CXCR4 surface receptors per cell is 10 times higher in gradients of CXCL12-γ than in CXCL12-α (850 compared to 86 CXCR4 surface receptors per cell).

Inhibition of either CXCR4 or CXCR7 results in a significant decrease in CXCR4+ migration in gradients of CXCL12-β. Given that single inhibition of CXCR4 or CXCR7 was relatively ineffective at limiting chemotaxis in CXCL12-γ gradients, we performed co-inhibition of CXCR4 and CXCR7, resulting in complete suppression of CXCR4+ movement (P-value = 0.52 at 24 hr compared to at 0 hr). To understand how these results on the 2D grid apply to the 3D environment, we performed additional simulations with the same parameters (as in Figure 3.5H-J), but with a 3D dimension for diffusion, using a grid size of 100x100x5 instead of 100x100x1. The gradient trends remain the same: CXCL12-γ and -β promote shorter and steeper gradients than CXCL12-α. When CXCR4+ cells within this expanded grid were allowed to move, we found that the 2D

migration trends hold true in 3D (Figure A.9). Taken together, these results demonstrate that CXCL12 isoforms form gradients that differ in shape, magnitude and scope even within the disorganized pattern of cancer cells present in some tumors. Moreover, we call attention to the importance of CXCL12-γ within the tumor environment, as its high ligand binding properties elicits higher CXCR4+ migration and requires interventions such as co-inhibition of CXCR4 and CXCR7 to significantly reduce migration.

3.5 Discussion

Chemotaxis plays a critical role at major stages of cancer progression. Angiogenesis required to supply the tumor with nutrients is directed by external gradients of cytokines such as vascular endothelial growth factor [72-75]. Tumor-promoting macrophages are recruited from blood to tumor sites by CCL2 and CCL5 [76]. Expression of chemokines and their receptors, such as CXCL12/CXCR4 and CCL21/CCR7, in both primary and metastatic tumors suggest that chemokine receptor-bearing cells actively enter the circulation and home to metastatic sites [12]. While it is well established that cells move in a directed manner towards chemoattractants, little is known about the shape and magnitude of chemoattractant gradients in tissue. Understanding gradient dynamics and cell responses to these gradients is imperative to targeting cancer metastasis.

Our multi-scale hybrid agent-based model calculates gradient formation as it is shaped by molecular-scale events and cellular behavior. We trained and validated the model on an *in vitro* microfluidic source-sink device that capitalizes on gradients formed by actively secreting CXCL12+ cells, migrating CXCR4+ cells, and scavenging CXCR7+ cells. We used the model to gain insight on why CXCL12 isoforms have differential effects on migration. Recent data suggest that different isoforms of CXCL12 may have distinct outcomes for cancer [1,20,77]. Our simulations demonstrate that ligand affinity for the migration surface and for CXCR4 significantly impact migration. Gradients of CXCL12-γ prompt greater migration of CXCR4+ cells than CXCL12-α in both the microfluidic source-sink device and the pseudo-tumor simulations and can in part be explained by high affinity for both the migration surface and receptor. High affinity for the surface results in steeper gradients for cells to navigate, and the high effective affinity for the

receptor results in a shift of the chemotaxis curve that allows higher migration even at lower secretion rates. In addition, cells in gradients of CXCL12-γ maintain higher levels of cell surface CXCR4 than when in gradients of the other CXCL12 isoforms. This is analogous to reports of enhanced chemotaxis with higher cell surface CXCR4 in the pathological setting of WHIM syndrome (warts, hypogammaglobulinemia, infections, and myelokathexis). The cytoplasmic tail of CXCR4 is truncated in WHIM syndrome, resulting in reduced internalization,higher number of CXCR4 surface receptors, and enhanced chemotaxis of leukocytes in response to CXCL12 [3,78]. These factors may explain why CXCL12-γ is better at eliciting chemotaxis of immune cells and endothelial progenitors compared to other isoforms [20,79].

The properties that make CXCL12-γ better at eliciting chemotaxis also make it harder to inhibit. Blocking CXCR4 or CXCR7 is less effective at inhibiting CXCR4+ migration when the ligand (like CXCL12-γ) has a high affinity for the migration surface or for CXCR4. Our pseudo-tumor simulations demonstrate that blocking both CXCR4 and CXCR7 receptors may be a potential method to inhibit migration in such gradients. In addition to having a higher affinity for the migration surface and CXCR4, CXCL12-γ is present at lower levels within the tumor environment [77], and lower levels of CXCL12 correlate with increased metastasis in mouse models and worse prognosis in breast cancer [14,15,77,80,81]. The combined effects of low expression and high binding characteristics make CXCL12-γ a worthwhile target for study in cancer metastasis.

More broadly, our simulations highlight the importance of non-specific ligand binding to extracellular space. We predict that the majority of the chemokine presented to cells is surface-immobilized, even for ligands with ostensibly lower affinities to surface-sites as CXCL12-α. These findings are consistent with *in vivo* findings of stable and functional haptotactic gradients [82]. Many extracellular matrix proteins, such as heparan sulfate and collagens, have been shown to be elevated in cancer [83], but much of the research focus is on their mechanical properties. Our simulations indicate that the high presence of extracellular matrix proteins in cancer may support the steep, short-distance gradients that more efficiently regulate chemotaxis.

One surprising result is that cells shape their own gradient as they move. Largely due to the difficulty of visualizing gradients, most reports of CXCR4+ chemotaxis overlook the participation of CXCR4-bearing cells in shaping their own gradient. Here we use our agent-based model to observe and confirm that cell clusters of CXCR4 actively shape their own gradients. In the *in vitro* microfluidic source-sink device, the collective migrating cells maintain gradient steepness locally at the leading edge. In the pseudo-tumor simulations, we find that individual CXCR4+ cells deplete ligand in their local environment. There is currently little literature on the potential for cells to shape their own gradient [38,84]; this may be one mechanism by which migrating cells can promote migration of follower cells [85].

While the receptor-ligand binding and internalization dynamics were constructed and validated on quantitative experimental data [32], we recognize that the model uses a simplified view of the complex interactions among CXCL12, CXCR4 and CXCR7. All of these proteins exist in both monomer and dimer forms that may have further implications on the strength of chemotaxis response or switches to other biological responses [33-35,86,87]. The presence of heparan sulfate, which was incorporated in the model with device surface-sites as well as the increased effective affinity of CXCL12 to CXCR4, further complicates the picture by inducing CXCL12 dimers and may alter CXCR4 recognition of the ligand [88,89]. As we gain more knowledge as to how these complicated interactions affect cell responses, we will be able to model more complicated behaviors of migrating cells within CXCL12 gradients.

Ultimately, we are interested in what gradients may look like in the tumor environment. Gradients form even with disorganized tissue architecture present in cancers. We find that short-distance, steep gradients promote greater chemotaxis towards chemokine-secreting cells than shallow gradients maintained over longer distances. Only a few reports have successfully visualized *in vivo* gradients [82,90,91], but characteristics such as gradient shape and magnitude have not been quantified. As imaging techniques such as intravital microscopy improve, we should be able to gain more information on gradient

formation over time and position in living tissues. To improve our understanding of the factors that modulate chemotaxis in tumors, it will be important to gather more histological data on the numbers and patterning of secreting and receptor-bearing cells in the tumor environment. Improvements to the model should capture matrix interactions in a packed cell environment, the mechanics of cell movement in a dense tissue environment, possible gradients of glycosaminoglycans, and isoform-specific protection from degradation. The integration of computational and experimental work to understand *in vivo* gradient formation will also provide insights to allow modulation of gradients for therapeutic purposes.

3.6 Tables

Table 3.1 Isoform-specific fitted parameters

Parameter	Definition	CXCL12-α	CXCL12-β	CXCL12-γ
$K_{D,L,S}$ (nM)	Equilibrium dissociation constant for surface site binding	100	20	5
CXCL12sec (#/cell-s)	Secretion rate constant	20	15	5
$K_{D,R4,L12}$ (nM)	Effective equilibrium dissociation constant for CXCR4 binding	40	40	10
m	Chemotaxis sensitivity factor slope	-6.73×10^{-3}	-6.73×10^{-3}	-6.25×10^{-3}
b	Chemotaxis sensitivity factor y-intercept	3.5×10^{3}	3.5×10^{3}	3.5×10^{3}

3.7 Figures

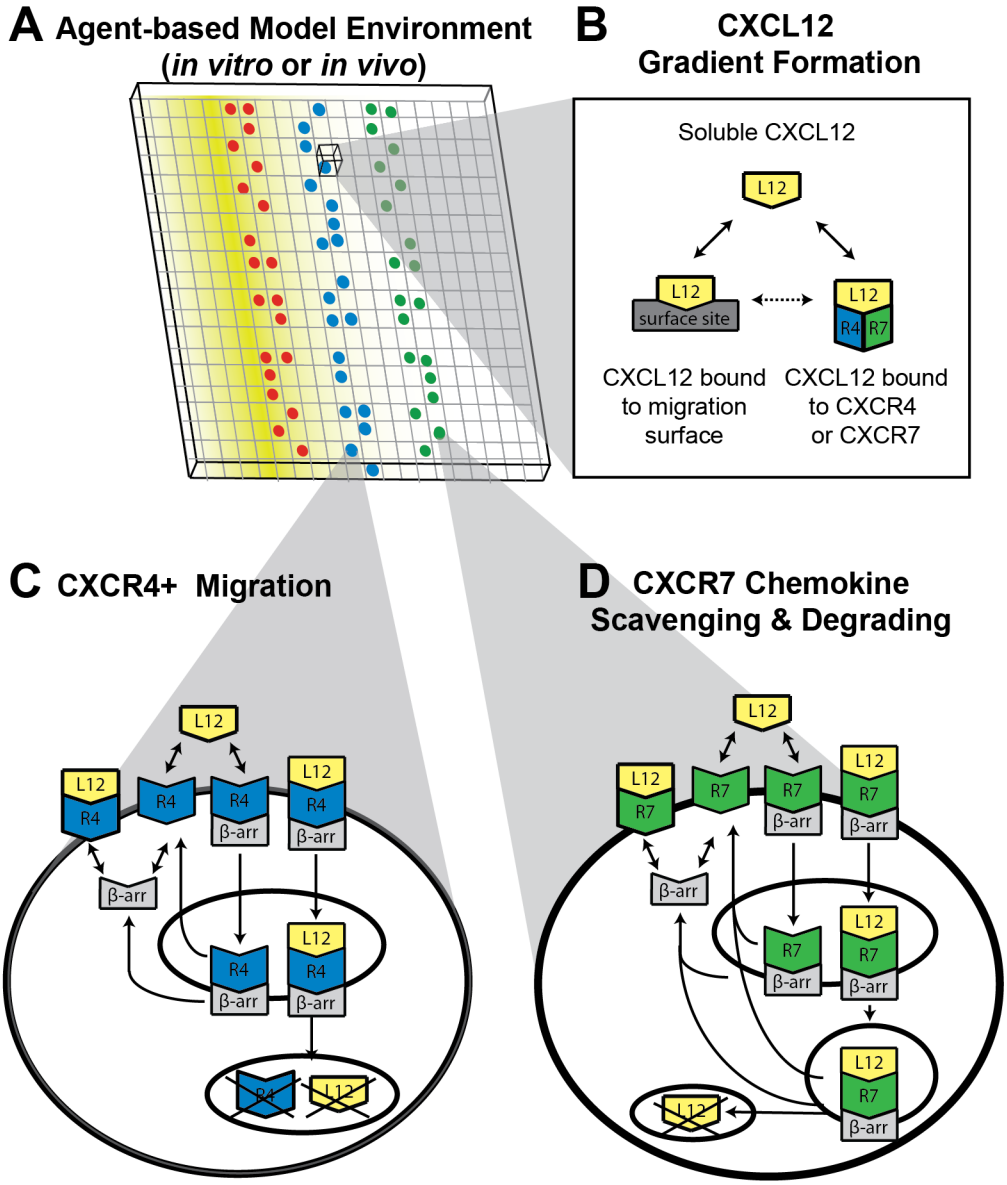

Figure 3.1 Multi-scale hybrid agent-based model

Model simulates CXCR4+ cell movement in response to CXCL12 gradients. (A) Three types of agents (cells) move in a discrete manner on the surface of a 2D or 3D lattice: CXCL12+, CXCR4+ cells and CXCR7+ cells. CXCL12 gradients are formed and shaped by diffusion and degradation binding to the migration surface (B), and receptor-mediated uptake by CXCR4 (C) and CXCR7 (D). We assume that both soluble CXCL12 and CXCL12 bound to the migration surface are able to bind CXCR4 or CXCR7. Molecule-scale dynamics shown in C and D are described by experiments and model in [32].

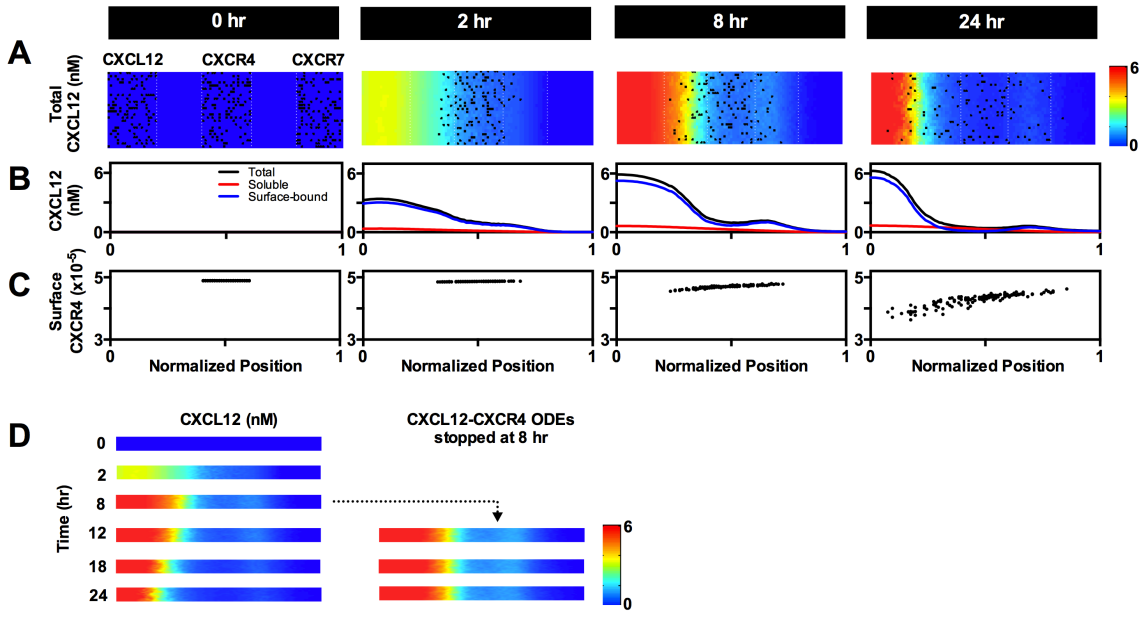

Figure 3.2 Multi-scale model predicts cell movement, molecular-scale information, and gradient formation within the microfluidic source-sink device

(A) Heat maps depict CXCL12 concentration in the agent layer and are overlaid with agent positions. Initial patterning of CXCL12+, CXCR4+ and CXCR7+ cells is shown at 0 hr. CXCL12+ and CXCR7+ cells, which move randomly, are not shown at later time points for clarity. Concentration values are averaged from 30 simulations. Cell positions shown are from one representative simulation. (B) Contribution of surface-bound (blue) and soluble (red) CXCL12 on total CXCL12 (black) concentration. At 0 hr, all concentrations are 0 nM. Concentration values are averaged from 30 simulations. (C) Number of CXCR4 surface receptors (sum of free, ligand-bound and β-arrestin-bound CXCR4) per individual CXCR4+ cell is plotted at the cell's position across the width of the device. Data are shown for one representative simulation, the same simulation used for cell positions in (A). (D) Heat maps depicting CXCL12 concentration when CXCL12-CXCR4 binding and internalization ODEs are turned off at 8 hrs. All simulations depicted here were run with parameters from Table A.1. Normalized position of 0 to 1 corresponds to the device width of 0.5mm to 1.5mm.

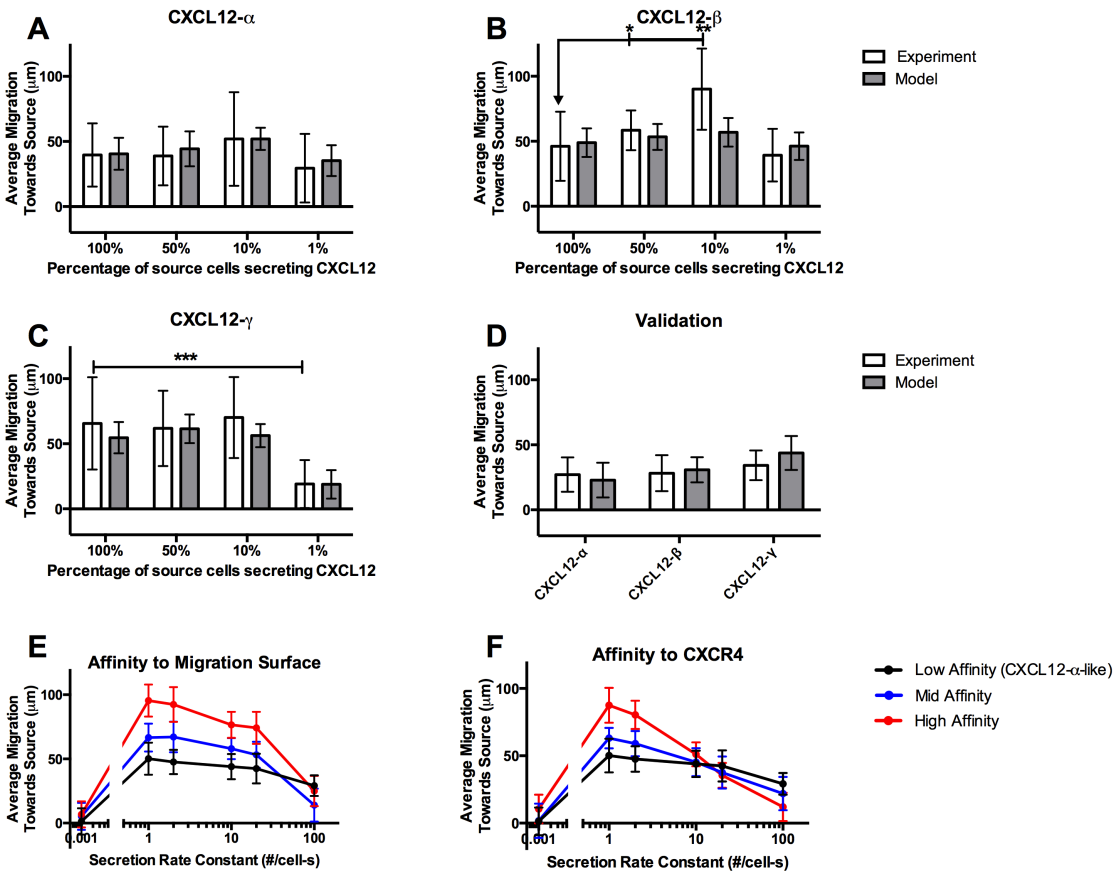

Figure 3.3 CXCL12 isoform-specific effects on CXCR4+ cell migration

(A-C) Experimental data show isoform-specific differences in average CXCR4+ cell migration as a function of the percentage of source cells secreting CXCL12 in our source-sink device (data from [1]). We fit our model to these data by varying four isoform-specific parameters (chemotaxis sensitivity factor parameter *m*, CXCL12 isoform affinity to the migration surface, CXCL12 isoform effective affinity for CXCR4, and CXCL12 isoform secretion rate). (D) Using the model, we predicted the average migration of CXCR4+ cells within the same source-sink device for when 100% of source cells are secreting and when the distance between the cells stripes is increased from 200 μm to 400 μm. Compared to panels A-C, migration for all isoforms is reduced. We measured the average migration using the source-sink device and find that that it matches model predictions. (E,F) The model predicts CXCR4+ average migration for different secretion rate constants of CXCL12+ cells as (E) ligand affinity to migration surface (Mid affinity $K_{D,L,S}$ = 5nM; High affinity $K_{D,L,S}$ = 1nM) and (F) ligand affinity to CXCR4 (Mid affinity $K_{D,R4,L12}$ = 5nM; High affinity $K_{D,R4,L12}$ = 1nM) are increased. The low affinity case for both E and F uses the CXCL12-α parameters listed in Table A.1. Model data are expressed as mean of 30 replications +/- standard deviation. For experiments only: * $P < 0.05$; ** $P < 0.005$; *** $P < 0.0005$.

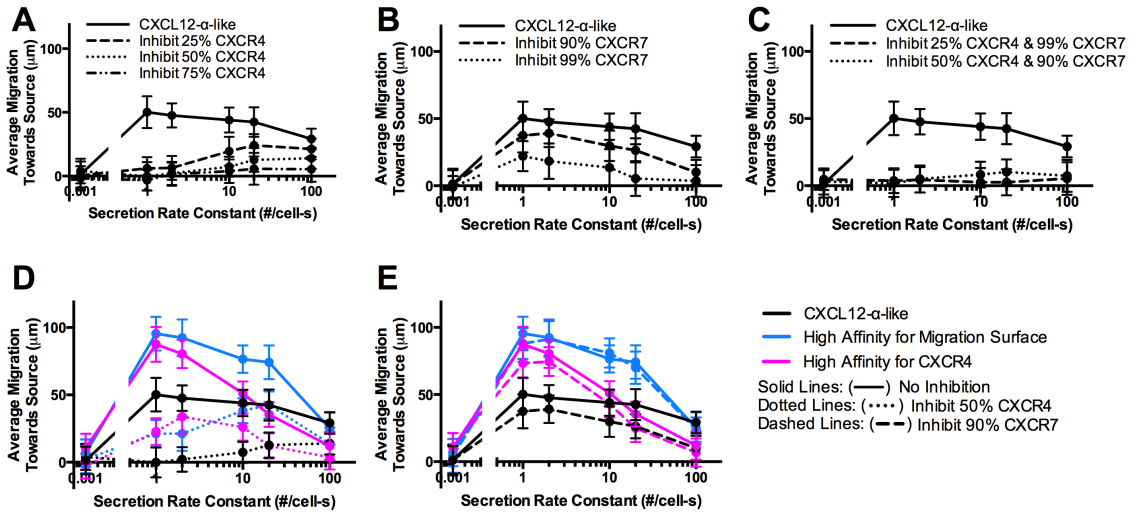

Figure 3.4 Blocking migration to high affinity ligands is more difficult than to low affinity ligands

Average migration of CXCR4+ cells for different secretion rate constants of CXCL12-secreting cells as (A) CXCR4, (B) CXCR7 or (C) both CXCR4 and CXCR7 are blocked. Blocking 50% of CXCR4 receptors (D) or 90% of CXCR7 receptors (E) is not as effective at reducing CXCR4+ migration when the ligand has a high affinity for CXCR4 ($K_{D,R4,L12}$ = 1nM) and when the ligand has a high affinity for the migration surface ($K_{D,L,S}$ = 1nM). Data are expressed as mean of 30 replications +/- standard deviation.

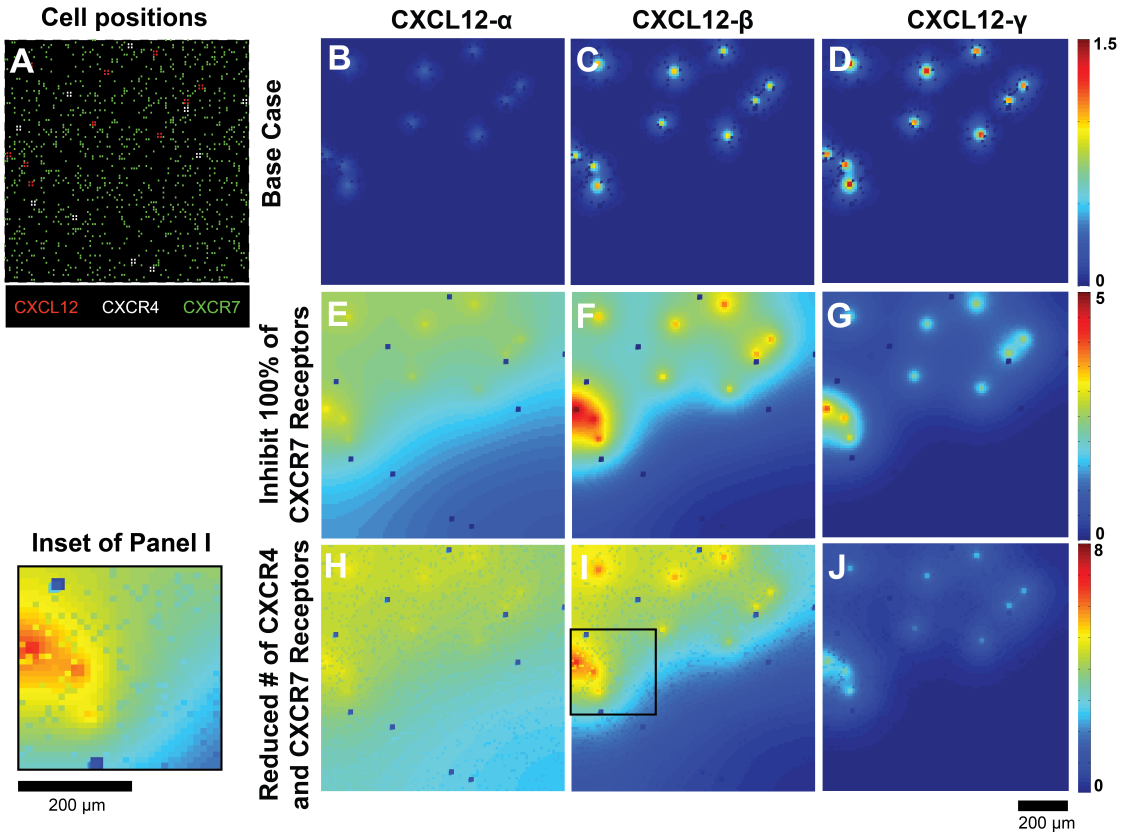

Figure 3.5 Gradients form even in disorganized cell structures representative of tumors

(A) Positions of CXCL12+ (red), CXCR4+ (white) and CXCR7+ (green) cells in simulation, based on histological data from literature [10,14,15]. We predicted chemokine gradients using same parameters as used in the device (Table A.1) for CXCL12-α (B), CXCL12-β (C) and CXCL12-γ (D). Gradients when CXCR7+ cells are replaced with non-receptor bearing cells for CXCL12-α (E), CXCL12-β (F) and CXCL12-γ (G). Gradients using a reduced number of CXCR4 and CXCR7 receptors ($5x10^3$ per cell) for CXCL12-α (H), CXCL12-β (I) and CXCL12-γ (J). Gradients shown are at 24 hr; cells were immobile throughout the entire time period. Data are expressed as mean concentration using 30 replications.

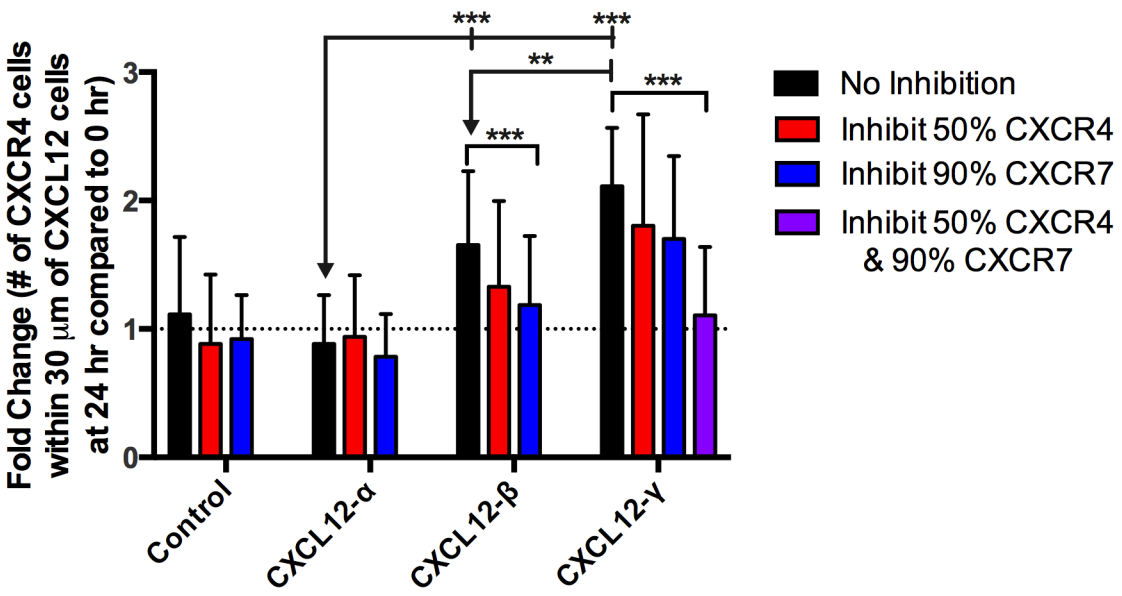

Figure 3.6 CXCL12-γ enhances migration in tumor-like simulations

Model predictions of directed CXCR4+ migration in a tumor-like environment. Number of CXCR4+ cells within 30 μm of a CXCL12 cluster at 24 hr represented as fold change (in comparison to number at 0 hr). Each simulation had a randomly generated pattern. CXCL12 and CXCR7+ cells remained static throughout the entire time period, whereas CXCR4+ cells were allowed to move. All parameters are the same as those used for gradient predictions in Figure 3.5H-J, with reduced numbers of CXCR4 and CXCR7 ($5x10^3$ per cell), except that the chemotaxis sensitivity factors (for all isoforms: m=-$6.85x10^{-3}$, b=25) were altered to increase sensitivity to migration. Control simulation lacks CXCL12 on the grid. Data are expressed as mean of 30 replications +/- standard error of the mean. Arrows represent statistics using Student's T-test, brackets represent statistics using ANOVA. * $P < 0.05$, ** $P < 0.0005$, *** $P < 0.0005$

3.8 References

1. Cavnar SP, Ray P, Moudgil P, Chang SL, Luker KE, et al. (2014) Microfluidic source-sink model reveals effects of biophysically distinct CXCL12 isoforms in breast cancer chemotaxis. Integr Biol (Camb) 6: 564-576.
2. Torisawa YS, Mosadegh B, Bersano-Begey T, Steele JM, Luker KE, et al. (2010) Microfluidic platform for chemotaxis in gradients formed by CXCL12 source-sink cells. Integr Biol (Camb) 2: 680-686.
3. Balabanian K, Lagane B, Pablos JL, Laurent L, Planchenault T, et al. (2005) WHIM syndromes with different genetic anomalies are accounted for by impaired CXCR4 desensitization to CXCL12. Blood 105: 2449-2457.
4. Buckley CD, Amft N, Bradfield PF, Pilling D, Ross E, et al. (2000) Persistent induction of the chemokine receptor CXCR4 by TGF-beta 1 on synovial T cells contributes to their accumulation within the rheumatoid synovium. J Immunol 165: 3423-3429.
5. Lukacs NW, Berlin A, Schols D, Skerlj RT, Bridger GJ (2002) AMD3100, a CxCR4 antagonist, attenuates allergic lung inflammation and airway hyperreactivity. Am J Pathol 160: 1353-1360.
6. Dubrovska A, Elliott J, Salamone RJ, Telegeev GD, Stakhovsky AE, et al. (2012) CXCR4 expression in prostate cancer progenitor cells. PLoS One 7: e31226.
7. Bendall LJ, Baraz R, Juarez J, Shen W, Bradstock KF (2005) Defective p38 mitogen-activated protein kinase signaling impairs chemotaxic but not proliferative responses to stromal-derived factor-1alpha in acute lymphoblastic leukemia. Cancer Res 65: 3290-3298.
8. Rubin JB, Kung AL, Klein RS, Chan JA, Sun Y, et al. (2003) A small-molecule antagonist of CXCR4 inhibits intracranial growth of primary brain tumors. Proc Natl Acad Sci U S A 100: 13513-13518.
9. Allinen M, Beroukhim R, Cai L, Brennan C, Lahti-Domenici J, et al. (2004) Molecular characterization of the tumor microenvironment in breast cancer. Cancer Cell 6: 17-32.
10. Orimo A, Gupta PB, Sgroi DC, Arenzana-Seisdedos F, Delaunay T, et al. (2005) Stromal fibroblasts present in invasive human breast carcinomas promote tumor growth and angiogenesis through elevated SDF-1/CXCL12 secretion. Cell 121: 335-348.
11. Teicher BA, Fricker SP (2010) CXCL12 (SDF-1)/CXCR4 pathway in cancer. Clin Cancer Res 16: 2927-2931.
12. Muller A, Homey B, Soto H, Ge N, Catron D, et al. (2001) Involvement of chemokine receptors in breast cancer metastasis. Nature 410: 50-56.
13. Rajagopal S, Kim J, Ahn S, Craig S, Lam CM, et al. (2010) Beta-arrestin- but not G protein-mediated signaling by the "decoy" receptor CXCR7. Proc Natl Acad Sci U S A 107: 628-632.
14. Luker KE, Lewin SA, Mihalko LA, Schmidt BT, Winkler JS, et al. (2012) Scavenging of CXCL12 by CXCR7 promotes tumor growth and metastasis of CXCR4-positive breast cancer cells. Oncogene 31: 4750-4758.
15. Miao Z, Luker KE, Summers BC, Berahovich R, Bhojani MS, et al. (2007) CXCR7 (RDC1) promotes breast and lung tumor growth in vivo and is expressed on tumor-associated vasculature. Proc Natl Acad Sci U S A 104: 15735-15740.
16. Yu L, Cecil J, Peng SB, Schrementi J, Kovacevic S, et al. (2006) Identification and expression of novel isoforms of human stromal cell-derived factor 1. Gene 374: 174-179.
17. Altenburg JD, Jin Q, Alkhatib B, Alkhatib G (2010) The potent anti-HIV activity of CXCL12gamma correlates with efficient CXCR4 binding and internalization. J Virol 84: 2563-2572.
18. Amara A, Lorthioir O, Valenzuela A, Magerus A, Thelen M, et al. (1999) Stromal cell-derived factor-1alpha associates with heparan sulfates through the first beta-strand of the chemokine. J Biol Chem 274: 23916-23925.
19. Laguri C, Sadir R, Rueda P, Baleux F, Gans P, et al. (2007) The novel CXCL12gamma isoform encodes an unstructured cationic domain which regulates bioactivity and interaction with both glycosaminoglycans and CXCR4. PLoS One 2: e1110.
20. Rueda P, Balabanian K, Lagane B, Staropoli I, Chow K, et al. (2008) The CXCL12gamma chemokine displays unprecedented structural and functional properties that make it a paradigm of chemoattractant proteins. PLoS One 3: e2543.
21. Qutub AA, Mac Gabhann F, Karagiannis ED, Vempati P, Popel AS (2009) Multiscale models of angiogenesis. IEEE Eng Med Biol Mag 28: 14-31.

22. Kirschner DE, Hunt CA, Marino S, Fallahi-Sichani M, Linderman JJ (2014) Tuneable resolution as a systems biology approach for multi-scale, multi-compartment computational models. Wiley Interdiscip Rev Syst Biol Med.
23. Walpole J, Papin JA, Peirce SM (2013) Multiscale computational models of complex biological systems. Annu Rev Biomed Eng 15: 137-154.
24. Luker KE, Mihalko LA, Schmidt BT, Lewin SA, Ray P, et al. (2012) In vivo imaging of ligand receptor binding with Gaussia luciferase complementation. Nat Med 18: 172-177.
25. Bellmann-Sickert K, Beck-Sickinger AG (2011) Palmitoylated SDF1alpha shows increased resistance against proteolytic degradation in liver homogenates. ChemMedChem 6: 193-200.
26. Lambeir AM, Proost P, Durinx C, Bal G, Senten K, et al. (2001) Kinetic investigation of chemokine truncation by CD26/dipeptidyl peptidase IV reveals a striking selectivity within the chemokine family. J Biol Chem 276: 29839-29845.
27. DeFea KA (2007) Stop that cell! Beta-arrestin-dependent chemotaxis: a tale of localized actin assembly and receptor desensitization. Annu Rev Physiol 69: 535-560.
28. Fong AM, Premont RT, Richardson RM, Yu YR, Lefkowitz RJ, et al. (2002) Defective lymphocyte chemotaxis in beta-arrestin2- and GRK6-deficient mice. Proc Natl Acad Sci U S A 99: 7478-7483.
29. Naumann U, Cameroni E, Pruenster M, Mahabaleshwar H, Raz E, et al. (2010) CXCR7 functions as a scavenger for CXCL12 and CXCL11. PLoS One 5: e9175.
30. Sun Y, Cheng Z, Ma L, Pei G (2002) Beta-arrestin2 is critically involved in CXCR4-mediated chemotaxis, and this is mediated by its enhancement of p38 MAPK activation. J Biol Chem 277: 49212-49219.
31. Violin JD, DiPilato LM, Yildirim N, Elston TC, Zhang J, et al. (2008) beta2-adrenergic receptor signaling and desensitization elucidated by quantitative modeling of real time cAMP dynamics. J Biol Chem 283: 2949-2961.
32. Coggins NL, Trakimas D, Chang SL, Ehrlich A, Ray P, et al. (2014) CXCR7 Controls Competition for Recruitment of beta-Arrestin 2 in Cells Expressing Both CXCR4 and CXCR7. PLoS One 9: e98328.
33. Babcock GJ, Farzan M, Sodroski J (2003) Ligand-independent dimerization of CXCR4, a principal HIV-1 coreceptor. J Biol Chem 278: 3378-3385.
34. Luker KE, Gupta M, Luker GD (2009) Imaging chemokine receptor dimerization with firefly luciferase complementation. FASEB J 23: 823-834.
35. Percherancier Y, Berchiche YA, Slight I, Volkmer-Engert R, Tamamura H, et al. (2005) Bioluminescence resonance energy transfer reveals ligand-induced conformational changes in CXCR4 homo- and heterodimers. J Biol Chem 280: 9895-9903.
36. Woolf PJ, Linderman JJ (2004) An algebra of dimerization and its implications for G-protein coupled receptor signaling. Journal of Theoretical Biology 229: 157-168.
37. Boldajipour B, Mahabaleshwar H, Kardash E, Reichman-Fried M, Blaser H, et al. (2008) Control of chemokine-guided cell migration by ligand sequestration. Cell 132: 463-473.
38. Dona E, Barry JD, Valentin G, Quirin C, Khmelinskii A, et al. (2013) Directional tissue migration through a self-generated chemokine gradient. Nature 503: 285-289.
39. Venkiteswaran G, Lewellis SW, Wang J, Reynolds E, Nicholson C, et al. (2013) Generation and dynamics of an endogenous, self-generated signaling gradient across a migrating tissue. Cell 155: 674-687.
40. Checa S, Prendergast PJ (2009) A mechanobiological model for tissue differentiation that includes angiogenesis: a lattice-based modeling approach. Ann Biomed Eng 37: 129-145.
41. Fallahi-Sichani M, El-Kebir M, Marino S, Kirschner DE, Linderman JJ (2011) Multiscale computational modeling reveals a critical role for TNF-alpha receptor 1 dynamics in tuberculosis granuloma formation. J Immunol 186: 3472-3483.
42. Gerlee P, Anderson AR (2007) An evolutionary hybrid cellular automaton model of solid tumour growth. Journal of Theoretical Biology 246: 583-603.
43. Riggs T, Walts A, Perry N, Bickle L, Lynch JN, et al. (2008) A comparison of random vs. chemotaxis-driven contacts of T cells with dendritic cells during repertoire scanning. Journal of Theoretical Biology 250: 732-751.
44. Byrne MB, Kimura Y, Kapoor A, He Y, Mattam KS, et al. (2014) Oscillatory behavior of neutrophils under opposing chemoattractant gradients supports a winner-take-all mechanism. PLoS One 9: e85726.
45. Guo Z, Sloot PM, Tay JC (2008) A hybrid agent-based approach for modeling microbiological systems. Journal of Theoretical Biology 255: 163-175.

46. Herzmark P, Campbell K, Wang F, Wong K, El-Samad H, et al. (2007) Bound attractant at the leading vs. the trailing edge determines chemotactic prowess. Proc Natl Acad Sci U S A 104: 13349-13354.
47. Lin F, Butcher EC (2008) Modeling the role of homologous receptor desensitization in cell gradient sensing. J Immunol 181: 8335-8343.
48. Tranquillo RT, Lauffenburger DA (1987) Stochastic model of leukocyte chemosensory movement. J Math Biol 25: 229-262.
49. Wang SJ, Saadi W, Lin F, Minh-Canh Nguyen C, Li Jeon N (2004) Differential effects of EGF gradient profiles on MDA-MB-231 breast cancer cell chemotaxis. Exp Cell Res 300: 180-189.
50. Zigmond SH (1981) Consequences of chemotactic peptide receptor modulation for leukocyte orientation. J Cell Biol 88: 644-647.
51. Lauffenburger DA, Linderman JJ (1993) Receptors : models for binding, trafficking, and signaling. New York: Oxford University Press. x, 365 p. p.
52. Aznavoorian S, Stracke ML, Krutzsch H, Schiffmann E, Liotta LA (1990) Signal transduction for chemotaxis and haptotaxis by matrix molecules in tumor cells. J Cell Biol 110: 1427-1438.
53. Handel TM, Johnson Z, Crown SE, Lau EK, Proudfoot AE (2005) Regulation of protein function by glycosaminoglycans--as exemplified by chemokines. Annu Rev Biochem 74: 385-410.
54. Johnson Z, Proudfoot AE, Handel TM (2005) Interaction of chemokines and glycosaminoglycans: a new twist in the regulation of chemokine function with opportunities for therapeutic intervention. Cytokine Growth Factor Rev 16: 625-636.
55. Paskauskas S, Parseliunas A, Kerkadze V, Nobiling R, Schmidt J, et al. (2011) Blockade of leukocyte haptokinesis and haptotaxis by ketoprofen, diclofenac and SC-560. BMC Immunol 12: 64.
56. Bailly M, Wyckoff J, Bouzahzah B, Hammerman R, Sylvestre V, et al. (2000) Epidermal growth factor receptor distribution during chemotactic responses. Mol Biol Cell 11: 3873-3883.
57. Fricker SP, Anastassov V, Cox J, Darkes MC, Grujic O, et al. (2006) Characterization of the molecular pharmacology of AMD3100: a specific antagonist of the G-protein coupled chemokine receptor, CXCR4. Biochem Pharmacol 72: 588-596.
58. Hatse S, Princen K, Bridger G, De Clercq E, Schols D (2002) Chemokine receptor inhibition by AMD3100 is strictly confined to CXCR4. FEBS Lett 527: 255-262.
59. Choi T, Maurya MR, Tartakovsky DM, Subramaniam S (2012) Stochastic operator-splitting method for reaction-diffusion systems. J Chem Phys 137: 184102.
60. Cilfone NA, Kirschner DE, Linderman JJ (2014) Strategies for efficient numerical implementation of hybrid multi-scale agent-based models to describe biological systems. Cellular and Molecular Bioengineering.
61. Cilfone NA, Perry CR, Kirschner DE, Linderman JJ (2013) Multi-scale modeling predicts a balance of tumor necrosis factor-alpha and interleukin-10 controls the granuloma environment during Mycobacterium tuberculosis infection. PLoS One 8: e68680.
62. Lucas TA (2008) Operator Splitting for an Immunology Model Using Reaction-Diffusion Equations with Stochastic Source Terms. Siam Journal on Numerical Analysis 46: 3113-3135.
63. Mitha F, Lucas TA, Feng F, Kepler TB, Chan C (2008) The Multiscale Systems Immunology project: software for cell-based immunological simulation. Source Code Biol Med 3: 6.
64. Sundnes J, Lines GT, Tveito A (2005) An operator splitting method for solving the bidomain equations coupled to a volume conductor model for the torso. Math Biosci 194: 233-248.
65. Helton JC, Johnson JD, Sallaberry CJ, Storlie CB (2006) Survey of sampling-based methods for uncertainty and sensitivity analysis. Reliability Engineering & System Safety 91: 1175-1209.
66. Marino S, Hogue IB, Ray CJ, Kirschner DE (2008) A methodology for performing global uncertainty and sensitivity analysis in systems biology. Journal of Theoretical Biology 254: 178-196.
67. Balabanian K, Lagane B, Infantino S, Chow KY, Harriague J, et al. (2005) The chemokine SDF-1/CXCL12 binds to and signals through the orphan receptor RDC1 in T lymphocytes. J Biol Chem 280: 35760-35766.
68. Altenburg JD, Broxmeyer HE, Jin Q, Cooper S, Basu S, et al. (2007) A naturally occurring splice variant of CXCL12/stromal cell-derived factor 1 is a potent human immunodeficiency virus type 1 inhibitor with weak chemotaxis and cell survival activities. J Virol 81: 8140-8148.
69. Maksym RB, Tarnowski M, Grymula K, Tarnowska J, Wysoczynski M, et al. (2009) The role of stromal-derived factor-1--CXCR7 axis in development and cancer. Eur J Pharmacol 625: 31-40.

70. Hesselgesser J, Liang M, Hoxie J, Greenberg M, Brass LF, et al. (1998) Identification and characterization of the CXCR4 chemokine receptor in human T cell lines: ligand binding, biological activity, and HIV-1 infectivity. J Immunol 160: 877-883.
71. Nimmagadda S, Pullambhatla M, Stone K, Green G, Bhujwalla ZM, et al. (2010) Molecular imaging of CXCR4 receptor expression in human cancer xenografts with [64Cu]AMD3100 positron emission tomography. Cancer Res 70: 3935-3944.
72. Bentley K, Mariggi G, Gerhardt H, Bates PA (2009) Tipping the balance: robustness of tip cell selection, migration and fusion in angiogenesis. PLoS Comput Biol 5: e1000549.
73. Cleaver O, Krieg PA (1998) VEGF mediates angioblast migration during development of the dorsal aorta in Xenopus. Development 125: 3905-3914.
74. Serini G, Ambrosi D, Giraudo E, Gamba A, Preziosi L, et al. (2003) Modeling the early stages of vascular network assembly. EMBO J 22: 1771-1779.
75. Bauer AL, Jackson TL, Jiang Y (2007) A cell-based model exhibiting branching and anastomosis during tumor-induced angiogenesis. Biophysical Journal 92: 3105-3121.
76. Lamagna C, Aurrand-Lions M, Imhof BA (2006) Dual role of macrophages in tumor growth and angiogenesis. J Leukoc Biol 80: 705-713.
77. Zhao S, Chang SL, Linderman JJ, Feng FY, Luker GD (2014) A Comprehensive Analysis of CXCL12 Isoforms in Breast Cancer. Transl Oncol.
78. Lagane B, Chow KY, Balabanian K, Levoye A, Harriague J, et al. (2008) CXCR4 dimerization and beta-arrestin-mediated signaling account for the enhanced chemotaxis to CXCL12 in WHIM syndrome. Blood 112: 34-44.
79. Rueda P, Richart A, Recalde A, Gasse P, Vilar J, et al. (2012) Homeostatic and tissue reparation defaults in mice carrying selective genetic invalidation of CXCL12/proteoglycan interactions. Circulation 126: 1882-1895.
80. Mirisola V, Zuccarino A, Bachmeier BE, Sormani MP, Falter J, et al. (2009) CXCL12/SDF1 expression by breast cancers is an independent prognostic marker of disease-free and overall survival. Eur J Cancer 45: 2579-2587.
81. Wendt MK, Cooper AN, Dwinell MB (2008) Epigenetic silencing of CXCL12 increases the metastatic potential of mammary carcinoma cells. Oncogene 27: 1461-1471.
82. Weber M, Hauschild R, Schwarz J, Moussion C, de Vries I, et al. (2013) Interstitial dendritic cell guidance by haptotactic chemokine gradients. Science 339: 328-332.
83. Lu PF, Weaver VM, Werb Z (2012) The extracellular matrix: A dynamic niche in cancer progression. Journal of Cell Biology 196: 395-406.
84. Schneider IC, Haugh JM (2006) Mechanisms of gradient sensing and chemotaxis: conserved pathways, diverse regulation. Cell Cycle 5: 1130-1134.
85. Roussos ET, Condeelis JS, Patsialou A (2011) Chemotaxis in cancer. Nat Rev Cancer 11: 573-587.
86. Decaillot FM, Kazmi MA, Lin Y, Ray-Saha S, Sakmar TP, et al. (2011) CXCR7/CXCR4 heterodimer constitutively recruits beta-arrestin to enhance cell migration. J Biol Chem 286: 32188-32197.
87. Levoye A, Balabanian K, Baleux F, Bachelerie F, Lagane B (2009) CXCR7 heterodimerizes with CXCR4 and regulates CXCL12-mediated G protein signaling. Blood 113: 6085-6093.
88. Fermas S, Gonnet F, Sutton A, Charnaux N, Mulloy B, et al. (2008) Sulfated oligosaccharides (heparin and fucoidan) binding and dimerization of stromal cell-derived factor-1 (SDF-1/CXCL 12) are coupled as evidenced by affinity CE-MS analysis. Glycobiology 18: 1054-1064.
89. Sadir R, Baleux F, Grosdidier A, Imberty A, Lortat-Jacob H (2001) Characterization of the stromal cell-derived factor-1alpha-heparin complex. J Biol Chem 276: 8288-8296.
90. McDonald B, Pittman K, Menezes GB, Hirota SA, Slaba I, et al. (2010) Intravascular danger signals guide neutrophils to sites of sterile inflammation. Science 330: 362-366.
91. Okada T, Miller MJ, Parker I, Krummel MF, Neighbors M, et al. (2005) Antigen-engaged B cells undergo chemotaxis toward the T zone and form motile conjugates with helper T cells. PLoS Biol 3: e150.

Chapter 4

Regulation of G-protein coupled receptor signaling by competition control points

4.1 Abstract

Signaling pathways are highly connected networks with multiple shared components. Perturbations in one signaling pathway may result in unintended changes in another. In this chapter, we examine the role of competition in CXCL12/CXCR4/CXCR7 signaling pathway. These receptors share not only a ligand, CXCL12, but also intracellular signaling components such as β-arrestin and ERK. Both receptors are highly implicated in numerous cancers. To determine how targeting one receptor may result in unintended consequences due to the sharing of common components, we constructed a mechanistic model of CXCR4 and CXCR7 receptor dynamics and signaling. We find that CXCR7 has been overlooked in its role as a scavenger when co-expressed with CXCR4. Its high affinity for both CXCL12 and β-arrestin limit both aspects of CXCR4 signaling. The model also predicts that changes in β-arrestin can increase, decrease, or have no impact on CXCR4 G-protein signaling depending on receptor recycling and relative rates of phosphorylation to ligand binding. Furthermore, to determine if co-expression of CXCR7 affects patient outcomes, we trained and validated a Cox proportional hazards model incorporating CXCL12, CXCR4, and CXCR7. When taking into account these three genes, CXCR7 is the most significantly associated with clinical outcome.

4.2 Motivation

Signaling pathways are not isolated sets of intracellular reactions, but are connected networks that regulate and can be regulated by one another. Competition for shared components within signaling pathways plays a crucial role in determining cell responses and behavior. For example, competition is a means to ultrasensitivity, a mechanism to amplify signaling responses. Both intermolecular (multiple molecules competing for a substrate) and intramolecular (two sites on a single molecule competing for a substrate) competition are mechanisms by which graded responses are converted to switch-like responses [1-4]. As another example, G-protein coupled receptors (GPCRs), the most common receptor target for therapeutics, can operate through classical G-protein pathways as well as β-arrestins [5]. For the angiotensin II type 1A receptor, competition between the G-protein coupled receptor kinases GRK2 and GRK5/6 controls whether signaling occurs primarily through G-proteins or through β-arrestins, resulting in distinct dynamics of phosphorylated ERK [6]. Identifying key parameters controlling competition is critical to the design of therapeutics that limit off-target effects.

The CXCL12/CXCR4/CXCR7 signaling axis offers a unique opportunity to look at competition. While the majority of chemokine receptors have at least three ligands as binding partners [7], CXCL12 is the only known ligand for CXCR4, and has just one other receptor, CXCR7 (recently renamed as ACKR3) [8]. The CXCL12/CXCR4 signaling pathway is a requirement for immune cell homing and plays a key role in metastasis of many cancers [7,9-15]. Upon binding CXCL12, CXCR4 elicits G-protein activation, a rise in intracellular free calcium, cAMP inhibition, and signaling via Akt, ERK, and β-arrestin [16-21]. CXCR7 is an atypical chemokine receptor that signals primarily via β-arrestins and can also promote ERK signaling [5,22]. Therefore, CXCR4 and CXCR7 share a ligand, and many intracellular components, raising the potential for crosstalk between pathways.

While it appears that CXCR4 and CXCR7 co-expression results in signaling and cell behavior distinct from cells expressing only one of the receptors [23-27], consequences

of co-expression are still poorly understood. Since β-arrestin binds to CXCR7 with an order of magnitude higher affinity than to CXCR4 [28], one hypothesis is that CXCR7 co-expression would sequester β-arrestin and thus promote CXCR4-mediated G-protein signaling [24]. However, CXCR7 is also a high affinity receptor for CXCL12, and binds with an affinity 10 times higher than that of CXCR4 to CXCL12 [29]. It is difficult to extract patterns from literature because studies examining CXCR4 and CXCR7 co-expression use different cell lines, levels of receptor expression, ligand concentrations, and various assays to analyze signaling and behavioral outputs [23-27,30]. Even if experimental systems were made completely consistent, complexity still remains because competition occurs in the context of multiple simultaneous kinetic events. Therefore, computational modeling is an essential tool to understand and manipulate pathway outcomes.

To understand how competition modulates intracellular signaling pathways, we constructed a mechanistic model using ordinary differential equations that incorporate ligand-receptor dynamics, G-protein and β-arrestin signaling. We use this model to ask the following questions: To what extent does CXCR7 control CXCR4 signaling? Can we alleviate the effects of CXCR7 on CXCR4 signaling by adjusting levels of shared components or targeting a kinetic event? How does affecting the levels of the shared component, β-arrestin, or inhibiting CXCR7 affect CXCR4 signaling? To address these questions, we use a model system containing (?) G-protein-mediated phosphorylated ERK as our output of CXCR4 G-protein signaling. To understand how CXCR7 affects ERK signaling, we performed time course Westerns blots and found that the addition of CXCR7 reduces overall ERK signaling in MDA-MB-231 and mouse embryonic cell lines. Using our mechanistic model, we find that CXCR7 co-expression can reduce CXCR4-mediated G-protein signaling due to its high affinity for CXCL12, while simultaneously scavenging β-arrestin. Furthermore, adding a competitive inhibitor to CXCR7 can disrupt its effects on CXCL12/CXCR4 signaling, but only at high CXCL12 concentration when CXCL12 is not limiting. We also determined that targeting CXCR4 recycling or CXCR4 rates of ligand binding relative to phosphorylation are two potential methods to mediate CXCL12/CXCR4 signaling. Lastly, we evaluated the clinical

relevance of CXCL12/CXCR4/CXCR7 by creating a Cox proportional hazards model using publicly available clinical data. We found that out of the three genes, CXCR7 is most significantly associated with metastasis free survival, when taking into account all three proteins of the CXCL12/CXCR4/CXCR7 axis.

4.3 Methods

4.3.1 Model overview

The seven-transmembrane receptors CXCR4 and CXCR7 share at least three signaling components: CXCL12, β-arrestin, and ERK. We constructed a mass action kinetic model using ordinary differential equations to examine the role of competition between CXCR4 and CXCR7 as detailed in Figure 4.1 and Tables 4.1 - 4.4. We used our previously published and validated model of ligand and β-arrestin dynamics to CXCR4 and CXCR7 as the base of our model [28]. To examine CXCL12/CXCR4 signaling, we incorporated G-protein activation. To understand integrated signaling responses, we added ERK phosphorylation by both G-protein and β-arrestin pathways.

4.3.2 Ligand and β-arrestin binding to receptors

We assume that CXCL12 binds to CXCR4 and CXCR7 with a 1:1 stoichiometric ratio [31]. Although CXCL12 and its receptors exist as both monomers and dimers [16,23,30,32-35], we do not incorporate dynamics of dimer formation in the model, as previous reports show that the number of CXCR4 and CXCR7 homo- and heterodimers is not a function of CXCL12 or CXCL11 levels at physiological concentrations and remains relatively stable for ~ 60 minutes [30].

We include the presence of a CXCR7 inhibitor in the model to understand how inhibiting CXCR7 may shift CXCR4 signaling. We assume that the CXCR7 inhibitor is comparable to a current molecule in development, CCX733 (ChemoCentryx). We assume that the CXCR7 inhibitor competes with CXCL12 at the same binding site, activates β-arrestin recruitment to CXCR7, and trafficks similarly to CXCL12 with CXCR7 [36].

β-arrestin can bind to both ligand and non-ligand bound phosphorylated receptors. Our first generation model of CXCR4/CXCR7 dynamics did not include receptor

phosphorylation prior to β-arrestin binding [28]. The model in this work adds phosphorylation of free and ligand-bound receptors to simulate receptor phosphorylation by GRKs [37,38]. We assume that the concentration of GRK is not limiting, and therefore do not track it as a separate species in the model [6]. We found the addition of receptor phosphorylation to be needed to give appropriate phosphoERK dynamics (as discussed in more detail below.)

4.3.3 Receptor trafficking, degradation and recycling

CXCR4 is a class A G-protein coupled receptor that has a transient association with β-arrestin. CXCR7 is a biased receptor that has a more persistent interaction with β-arrestin [39]. In the model, this is incorporated by modeling the trafficking of internalized CXCR7 through a late endosome before recycling to the cell membrane. Ligand-bound CXCR4 is degraded, whereas non-ligand bound CXCR4 is recycled as free receptor to the surface. All CXCR7 is recycled and all ligands (CXCL12 and drug) are degraded.

4.3.4 G-protein and ERK signaling

We assume that ligand-bound CXCR4 can bind reversibly to G-proteins. Upon binding, the G-protein can be promoted to its activated state and detach from the receptor complex. We also incorporate constitutive activation and deactivation of G proteins [40-42]. G-protein-mediated ERK phosphorylation (gpERK) is a function of both activated G protein and ERK concentrations. G-protein-phosphorylated ERK can translocate to the nucleus [43]. ERK can also be phosphorylated via the CXCL12/CXCR7 β-arrestin pathway. CXCL12-bound CXCR7 residing in the endosome can induce phosphorylation of ERK (bpERK), which is calculated in a separate pool than G-protein-phosphorylated ERK. We assume the same rate constant for constitutive dephosphorylation of both bpERK and gpERK. Class A receptors such as CXCR4 result in transient activation of phosphorylated ERK that peaks between 2 and 10 minutes [32,44]. In order to achieve such a pattern, the model required the addition of the phosphorylated receptor species that is unable to interact with G-proteins.

4.3.5 Differences from the first generation model

There are four major differences from our first generation model. The first is the addition of receptor phosphorylation prior to β-arrestin binding. We fit the forward and reverse rate constants of the phosphorylation step to match measurements of CXCR4 and CXCR7-β-arrestin interaction (described in results)[28]. Second, we added equations for CXCR4-mediated G-protein signaling, including constitutive G-protein activation and deactivation, G-protein binding to CXCL12-bound CXCR4, activation of the CXCR4-G-protein complex, detachment of activated G-protein from the receptor-complex and activation of gpERK. Parameter ranges for these kinetic events were based on literature (Tables 4.1 - 4.4), and parameter values were adjusted within literature ranges to produce patterns of gpERK activation consistent with literature. Third, we added ERK phosphorylation from the β-arrestin pathway. Parameters of bpERK activation were taken from literature. Lastly, we adjusted the dissociation constant (KdL12R4) from its previous value of 40nM to 8nM, which is within the range of values reported in literature [32,45]. All baseline parameters, initial conditions, and equations can be found in Tables 4.1 - 4.4.

4.3.6 Measurement of phosphorylated ERK in MDA-MB-468 and MEFs

We cultured MDA-MB-468 and mouse embryonic fibroblasts in DMEM (Life Technologies) with 10% serum, 1% glutamine, and 0.1% penicillin/streptomycin. To induce increased CXCR7 expression, we transduced cells as described previously [28]. Cells were harvested and SDS-PAGE was performed using a 10% gel (Biorad). We analyzed endogenous phosphoERK1/2 and total ERK1/2 in total cell lysates by Western blotting with a rabbit mAb (Cell Signaling) and an anti-rabbit secondary antibody conjugated with horse radish peroxidase (Cell Signaling). Primary and secondary antibody dilutions for phosphoERK1/2 and total ERK1/2 were 1:1500 and 1:4000; and 1:4000 and 1:6000, respectively. We detected bound antibody complexes with Pierce ECL Western Blotting Substrate (Thermo Scientific). We used IVIS Spectrum instrument (Caliper, Hopkinton, MA, USA) to quantify light emitted from Western blots as photon flux.

4.3.7 Cox proportional hazards model

We used three publicly available breast cancer clinical cohorts and their associated clinical and normalized gene expression data. We divided these cohorts into a training cohort (Wang et al.), and two validation cohorts (Kao et al., van de Vijver et al). The clinical characteristics of the cohorts have been described previously. Briefly, the cohort by Wang et al. was comprised of 286 tumor samples from lymph node-negative patients from the Netherlands who were treated from 1980-95 and who did not receive systemic adjuvant or neoadjuvant therapy. The median age was 52 years, the median follow-up time was 8.4 years for the patients who survived, 97% were T1-2, and the majority (87%) received radiation therapy [46]. The first validation cohort was from Kao et al. and consisted of 327 frozen tumor samples from every third patient treated between 1991 and 2004 at the Koo Foundation Sun-Yat-Sen Cancer Center in Taiwan [47]. The median age was 46, median follow-up was 8.1 years, and the patients were heterogeneous in stage, grade, hormone receptor status and treatment modality [47]. The second validation cohort was from van de Vijver et al. and comprised 295 consecutive tumor samples from patients from the Netherlands who were treated from 1984-95, and who were diagnosed at age 52 or younger with a tumor less than 5cm in diameter. The median age was 44 and the median follow-up was 7.2 years [48].

The MIAME compliant datasets were downloaded from the Gene Expression Omnibus (GEO) database with series number GSE20685 (Kao) and GSE2034 (Wang). Data for the van de Vijver cohort was obtained from http://microarray-pubs.stanford.edu/wound_NKI/explore.html (also available from http://www.oncomine.org). Expression levels were log transformed, median centered and scaled. Wang was chosen to be the training cohort because the patients were node negative and had not received any adjuvant or neo-adjuvant systemic therapy and thus best captured true metastatic potential. We used the Cox proportional hazards function in R to create a gene signature incorporate CXCL12, CXCR4 and CXCR7. This model was fit to metastasis free survival in the training cohort with CXCL12, CXCR4 and CXCR7 as covariates. Then the model was used to make predictions in the validation cohorts.

Performance was evaluated by comparing the outcomes in the top quartile of the signature predictions, versus the rest, using the log-rank test in all three clinical cohorts.

4.4 Results

4.4.1 Model validation

In this work, we built upon our previously published and validated model of CXCR4 and CXCR7 ligand, receptor and β-arrestin dynamics to further understand how competition for shared components affect signaling [28]. To examine CXCL12/CXCR4 signaling, we added equations for G-protein activation, including G-protein binding to CXCL12-bound CXCR4, G protein activation and detachment (Figure 4.1). Both activated G-proteins and ligand-bound CXCR7 promote ERK phosphorylation. It has been well established that ERK phosphorylation by G-proteins (gpERK) is more transient, with a peak between 2-10 minutes, whereas β-arrestins promote a steady increase of ERK phosphorylation (bpERK) [32, 39, 44]. In order to produce gpERK temporal patterns consistent with literature, we implemented receptor phosphorylation as a requirement for β-arrestin association[38, 49] and to fit phosphorylation rate constants (kpR4, kpL12R4, kpR7, kpC7) of β-arrestin mediated pathways to ERK with the restriction that phosphorylation of ligand-bound receptors occurs with a faster rate constant than phosphorylation of free receptors (Table 4.1) [50, 51].

The addition of receptor phosphorylation did not significantly alter dynamics of β-arrestin interaction with the receptors. Fold change interaction of CXCR4 (Figure 4.2A) and CXCR7 (Figure 4.2B) to β-arrestin is still consistent with the first generation model, as well as experimental data measuring receptor-β-arrestin interaction using a bioluminescence complementation assay (Figure 4.2C,D) [28]. Due to a stronger interaction with β-arrestin, in the absence of ligand, CXCR7 is found mostly inside the cell, whereas a weaker interaction with β-arrestin results in primarily cell-surface CXCR4. Our model is also consistent with the observation that truncated CXCR4 unable to bind β-arrestin result in an increase of surface CXCR4, as in WHIM syndrome [37, 52] (Figure 4.2E).

4.4.2 Increasing CXCR7 results in reduced total ERK phosphorylation in MDA-MB-468 and mouse embryonic fibroblast cell lines

Previous reports of CXCR4 and CXCR7 co-expression use a variety of cell lines to probe combined CXCR4/CXCR7 signaling. The goal was to use cell lines that did not have detectable endogenous CXCR7, so we could look at the effects when adding CXCR7. This way, we could determine initial conditions of phosphorylated ERK and if the temporal patterns change. We administered 100ng/ml of CXCL12 to both normal (mouse embryonic fibroblasts) and cancer (MDA-MB-468 breast cancer cells) cells and performed Western blots for phosphorylated ERK. In both cell types, we found that overall levels of pERK decrease by 20-50% in the presence of increased CXCR7. We used this experimental data to inform the model for initial pERK levels (about 10% of total ERK).

4.4.3 Increasing CXCR7 results in reduced CXCR4-mediated G-protein signaling

CXCR7 has been hypothesized to promote CXCR4-mediated G-protein signaling by scavenging β-arrestin from CXCR4 [24]. To understand the effects of CXCR7 on CXCR4 signaling, we varied levels of CXCR7 in relation to CXCR4 expression from 0 to 50 times the number of CXCR4 receptors/cell. We also varied CXCL12 ligand concentration from 0.01 to 1000nM. All other parameters remained as in Table 4.1. We use G-protein phosphorylated ERK (gpERK) as our output of CXCR4 signaling.

The model predicts that CXCR7 co-expression results in a reduction of CXCR4-mediated G-protein signaling (Figure 4.4A). This trend remains with increasing or decreasing total CXCR4 (data not shown). While CXCR7 is a high affinity receptor for β-arrestin, it is also a high affinity partner for CXCL12. As CXCR7 levels increase, it scavenges both β-arrestin and CXCL12 from CXCR4 (Figure 4.4B). Reducing CXCR7 affinity to CXCL12 (Figure 4.4C) and reducing CXCR7 binding to β-arrestin can alleviate its effect on CXCR4 signaling (Figure C.1). Therefore, CXCR7 scavenges both CXCL12 and β-arrestin from CXCR4 (Figure 4.4E).

4.4.4 CXCR4 recycling and rapid phosphorylation enhances CXCR4-mediated G protein signaling

Following receptor phosphorylation by GRKs, β-arrestin scaffolds with CXCR4 or CXCR7 to internalize the receptor complexes. We hypothesized that increasing β-arrestin would result in decreased G-protein signaling due to increased competition between G proteins and β-arrestin for CXCR4. However, the model predicts the opposite: increasing β-arrestin results in a small increase (< 10%) of CXCR4-mediated G-protein signaling (Figure 4.5A). Despite increased G-protein signaling, the proportion of internalized and degraded receptors increases with β-arrestin levels. How can increased receptor internalization and increased G-protein signaling occur at the same time? By systematically turning off kinetic events in the model, we determined that this phenomenon is due to a combination of the following: (1) internalized CXCR4 recycles to the surface and (2) ligand binding is faster than phosphorylation. By eliminating CXCR4 recycling, G-protein signaling no longer increases with β-arrestin levels (Figure 4.5B), but instead decreases due to increased CXCR4 degradation. In addition, increasing the forward rate of binding of CXCL12 to CXCR4 while decreasing the phosphorylation rate of CXCR4 reduces the dependence on β-arrestin levels (Figure 4.5C). Thus, depending on the trafficking patterns of CXCR4 and the relative rates of ligand binding to receptor phosphorylation, increasing β-arrestin levels can provide two types of effects (Figure 4.5D).

4.4.5 High CXCR7 inhibitor concentrations can alleviate CXCL12 scavenging, but sequesters β-arrestin and promotes bpERK at high CXCL12 concentrations.

The role of CXCR7 in cancer has spurred the development of inhibitors against CXCR7 [53, 54]. Since CXCR7 shares many signaling components with CXCR4, we include the presence of a CXCR7 inhibitor in the model to understand how inhibiting CXCR7 may shift CXCR4 signaling. An inhibitor of CXCR7 might be expected to increase CXCR4-mediated G-protein signaling, due to a higher availability of CXCL12. Indeed, the model

predicts that at low CXCL12 concentrations, CXCR4-mediated G-protein signaling does increase with increasing CXCL11 (Figure 4.6A). Closer examination on where CXCL12 and ERK is being distributed reveals three distinct regions. At low CXCL12 and inhibitor concentrations, the majority of CXCL12 bound to any receptor preferentially binds to CXCR7 (Figure 4.6B). At low CXCL12 and high inhibitor concentrations, CXCL12 now preferentially binds to CXCR4. However at high CXCL12 concentration, CXCL12 is no longer limiting. Therefore, CXCL12/CXCR7 binding increases. The model also predicts that the G-protein and β-arrestin pathways compete for ERK. As gpERK decreases, bpERK increases (Figure 4.6C).

4.4.6 CXCR7 is most significantly associated with clinical outcomes within the signaling trio

The model has demonstrated how co-expression of CXCR7 with CXCR4 can dramatically shift CXCR4 signaling by affecting at least three control points: CXCL12, β-arrestin, and ERK. To investigate if the co-expression of CXCR7 is correlated with patient outcomes, we used publicly available clinical data to examine CXCL12, CXCR4, CXCR7 expression to create a three-gene Cox proportional hazards model. First, we evaluated the relationship between gene expression of CXCL12, CXCR4, and CXCR7 with metastasis free survival in the Wang clinical cohort. In this model, we found that low CXCL12 and high CXCR7 expression both confer significantly increased risk, which is consistent with previous reports (Figure 4.7A) [55, 56]. However, CXCR4 expression does not significantly affect metastasis risk after taking into account CXCL12 and CXCR7 expression. The gene signature is able to risk stratify patients in our training data (p=0.0002, HR=12.07). To validate the gene signature, we used the parameters from the Cox proportional hazards model in two addition clinical cohorts. We find that a high signature confers increased risk of metastasis in both cohorts (Kao: p=0.008, HR=1.81, Van de Vijver: p=0.002, HR=1.9), validating the prognostic ability of the model and confirming that the inter-relationship and relative gene expression of CXCL12, CXCR4, and CXCR7 are clinically important (Figure 4.7B).

4.5 Discussion

Despite the identification of countless oncogenes as major drivers of cancer, cancer drug development has a poor rate of clinical success [57]. Part of the difficulty in targeting the CXCL12/CXCR4 pathway is that it is essential for many homeostatic functions [58]. The second receptor to CXCL12, CXCR7, has also been implicated in cancer and inhibition of CXCR7 has been suggested as a strategy that may also mitigate the malignant effects of CXCR4 signaling [53, 54]. Considering that CXCR4 and CXCR7 share multiple components within their pathways, modulating one pathway may have undesired consequences for the other. To understand such consequences, we developed a mechanistic model of CXCL12/CXCR4/CXCR7 receptor dynamics and signaling with an emphasis on the shared components in the pathways.

Our model predicts that increasing CXCR7 results in a decrease in CXCR4-mediated G protein signaling across a large range of CXCL12 concentrations (Figure 4.4). This is supported by studies using cAMP inhibition, Ca2+ signaling and GTP-gS binding as metrics of G-protein activity [23, 24]. While other studies focus on the importance of CXCR7 in controlling extracellular ligand concentration and gradients [59-62], our model highlights the importance of CXCR7 in scavenging CXCL12 from CXCR4 receptors on the same cell. Due to its higher affinity for both ligand and β-arrestin, CXCR7 can significantly hamper CXCR4 signaling. Targeting CXCR7 with a competitive inhibitor can reverse these effects, but our model shows that if CXCL12 levels are not limiting, then the inhibitor has little effect (Figure 4.6). Thus, the model points to the importance of determining CXCL12 levels within tissue.

Receptor-ligand dynamics shifts the direction in which a shared molecule controls signaling. The model shows that increasing levels of β-arrestin can increase, decrease, or have no effect on CXCR4-mediated G-protein signaling, depending on recycling of internalized receptor and relative rates of ligand binding compared to receptor phosphorylation (Figure 4.5). This suggests one reason for the lack of consensus in

literature regarding how CXCR7 shapes CXCR4 signaling [23-27]. The direction in how a shift in β-arrestin levels affect CXCR4 signaling is sensitive to overall rates of recycling, receptor phosphorylation, and ligand binding. It is difficult to compare across experiments that use various cell types because controlling for all of these important events in receptor-ligand dynamics is not currently possible.

Once we established that co-expression of CXCR7 can regulate CXCR4 signaling, we investigated if patient outcomes are also dependent on the co-expression of CXCR4 and CXCR7. Previous studies have identified that CXCR4 and CXCL12 are independently correlated with patient outcomes [9, 15, 55, 56, 63, 64]. However, the expression of these three genes in the integrated CXCL12/CXCR4/CXCR7 signaling axis have never been evaluated in the context of one another. We created a Cox proportional hazards model that evaluates CXCL12, CXCR4, and CXCR7 expression in three breast cancer clinical cohorts. This model calculates that CXCR7 is most significantly correlated with patient outcome compared to CXCL12 and CXCR4. In addition, the hazard ratio of CXCR7 (1.186) suggests that higher levels of CXCR7 confer with worse patient prognosis.

One future direction is to predict which downstream pathway of CXCR4 is the one related to malignancy. While our Cox proportional hazards model suggests that increasing CXCR7 is related to worse outcomes, our mechanistic model is unable to pinpoint if it is due to altered CXCR4-mediatd G-protein or β-arrestin signaling, as increasing CXCR7 limits both G-protein and β-arrestin pathways. Furthermore, while we detailed receptor-ligand dynamics in this model, our model did not detail potential signaling differences when CXCR4 and CXCR7 create heterodimers, which may have signaling effects unique to the heterodimer structure. Lastly, a major limitation with the clinical data used in the Cox proportional hazards model is the inability to determine if cells co-express CXCR4 and CXCR7, or if they are expressed on separate populations of cells.

4.6 Tables

Table 4.1 Initial quantities

Parameter	Units	Description	Totals*	Steady-state value
R4	#/cell	Free surface CXCR4	10^5 [1]	$2.0x10^4$
R4p	#/cell	Phosphorylated R4	0	$5.8x10^4$
R4B	#/cell	β-arrestin-bound R4	0	$6.5x10^2$
L12R4	#/cell	CXCL12-bound R4	0	0
L12R4p	#/cell	Phosphorylated L12R4	0	0
L12R4B	#/cell	β-arrestin-bound L12R4	0	0
L12R4G	#/cell	G-protein-bound L12R4	0	0
L12R4Ga	#/cell	Ga-bound L12R4	0	0
R4Bi	#/cell	Internalized R4 (B is removed)	0	$2.2x10^4$
L12R4Bi	#/cell	Internalized L12R4B	0	0
L12R4Bii	#/cell	L12R4Bi after B removal	0	0
degR4	#/cell	Degraded R4	0	0
R7	#/cell	Free surface CXCR7	10^5 [1]	$9.3x10^1$
R7p	#/cell	Phosphorylated R7	0	$8.2x10^4$
R7B	#/cell	β-arrestin-bound R7	0	$2.9x10^3$
L12R7	#/cell	CXCL12-bound R7	0	0
L12R7p	#/cell	Phosphorylated L12R7	0	0
L12R7B	#/cell	β-arrestin-bound L12R7	0	0
R7Bi	#/cell	Internalized R7B	0	$4.5x10^3$
R7Bii	#/cell	R7Bi after B removal	0	$1.0x10^4$
L12R7Bi	#/cell	Internalized L12R7Bi	0	0
L12R7Bii	#/cell	L12R7Bi trafficked to late endosome	0	0
XR7	#/cell	Inhibitor-bound R7	0	0
XR7p	#/cell	Phosphorylated XR7	0	0
XR7B	#/cell	β-arrestin-bound XR7	0	0
XR7Bi	#/cell	Internalized XR7Bi	0	0
XR7Bii	#/cell	XR7Bi trafficked to late endosome	0	0
B	#/cell	Free β-arrestin	10^5 [1]	$9.2x10^4$
G	#/cell	Unactivated G protein	10^5 [2,3]	$9.9x10^4$
Ga	#/cell	Activated G protein	10^4	$1.0x10^1$
L12	nM	Extracellular CXCL12	0	0
X	nM	Extracellular inhibitor	0	0
ERK	#/cell	Free ERK	10^5 [3,4]	$8.0x10^4$
gpERK	#/cell	ERK phosphorylated by Ga	0	$1.0x10^4$
bpERK	#/cell	ERK phosphorylated by L12R7Bi	0	$1.0x10^4$
nucERK	#/cell	gpERK translocated to the nucleus	0	0

* In order to determine the distribution of receptors bound to β-arrestin prior to ligand binding, equations are solved in the absence of ligand to steady-state conditions.

Table 4.2 Rate constants

Description	Parameter	Value	Units	
Ligand binding				
Forward rate constant of L12 binding to R4, R4p and R4B	$kf_{L12,R4}$	$2.1x10^{-3}$	$nM^{-1}s^{-1}$	[1]
Forward rate constant of L12 binding to R7, R7p and R7B	$kf_{L12,R7}$	$1.4x10^{-3}$	$nM^{-1}s^{-1}$	[1]
Dissociation constant of L12 from R4	$KD_{L12,R4}$	8.0	nM	[1]
Dissociation constant of L12 from R4p and R4B	$KD_{L12,R4B}$	$(KD_{L12,R4}\,KD_{B,L12R4})/KD_{B,R4}$	nM	[1]
Dissociation constant of L12 from R7	$KD_{L12,R7}$	$8.0x10^{-1}$	nM	[1]
Dissociation constant of L12 from R7p and R7B	$KD_{L12,R7B}$	$(KD_{L12,R7}\,KD_{B,L12R7})/KD_{B,R7}$	nM	[1]
β-arrestin binding				
Forward rate constant of B binding to R4p and L12R4p	$kf_{B,R4}$	$8.5x10^{-9}$	cell/#/s	[1]
Forward rate constant of B binding to R7p and L12R7p	$kf_{B,R7}$	$1.4x10^{-8}$	cell/#/s	[1]
Dissociation constant of B from R4p	$KD_{B,R4}$	$7.8x10^{6}$	cell/#/s	[1]
Dissociation constant of B from L12R4p	$KD_{B,L12R4}$	$5.1x10^{6}$	cell/#/s	[1]
Dissociation constant of B from R7p	$KD_{B,R7}$	$2.3x10^{6}$	cell/#/s	[1]
Dissociation constant of B from L12R7p	$KD_{B,L12R7}$	$6.5x10^{5}$	cell/#/s	[1]
Internalization and trafficking				
Rate constant for internalization of R4B	ke_{R4B}	$2.3x10^{-3}$	s^{-1}	[1]
Rate constant for internalization of L12R4B	ke_{L12R4B}	$4.7x10^{-3}$	s^{-1}	[1]
Rate constant for recycling of R4Bi to cell surface	$krec_{R4Bi}$	$6.9x10^{-5}$	s^{-1}	[1]
Dissociation rate constant of B from L12R4i	$koff_{B,L12R4i}$	$7.4x10^{-4}$	cell/#/s	[1]
Rate constant for degradation of R4	$kdeg_{R4}$	$1.0x10^{-4}$	s^{-1}	[1]
Rate constant for internalization of R7B	ke_{R7B}	$3.9x10^{-3}$	s^{-1}	[1]
Rate constant for internalization of L12R7B	ke_{L12R7B}	$2.1x10^{-3}$	s^{-1}	[1]
Rate constant for trafficking of L12R7B	$ktr_{L12R7Bi}$	$5.5x10^{-4}$	s^{-1}	[1]
Rate constant for recycling of L12R7B	$krec_{L12R7Bi}$	$2.8x10^{-4}$	s^{-1}	[1]
Dissociation rate constant of B from R7Bi	$koff_{B,R7}$	$2.5x10^{-3}$	cell/#/s	[1]
Rate constant for degradation of L12	$kdeg_{L12}$	$1.0x10^{-4}$	s^{-1}	[1]
Equations for CXCR7 inhibitor, X				
Forward rate of X binding to R7	$kf_{X,R7}$	$kf_{L12,R7}$	$nM^{-1}s^{-1}$	
Dissociation constant of B from XR7	$KD_{B,XR7}$	$KD_{B,L12R7}$	cell/#/s	
Forward rate of B binding to XR7	$kf_{B,XR7}$	$kf_{B,R7}$	$nM^{-1}s^{-1}$	
Dissociation constant of X from R7	$KD_{X,R7}$	2	nM	
Dissociation constant of X binding to R7p and R7B	$KD_{X,R7B}$	$KD_{X,R7}\,KD_{B,XR7}\,/\,KD_{B,R7}$	nM	[5]
Internalization of XR7B	ke_{XR7B}	ke_{L12R7B}	s^{-1}	
Rate constant for trafficking of XR7B	ktr_{XR7Bi}	$ktr_{L12R7Bi}$	s^{-1}	
Rate constant for recycling of XR7B	$krec_{XR7Bi}$	$krec_{L12R7Bi}$	s^{-1}	
Degradation of X	$kdeg_{X}$	$kdeg_{L12}$	s^{-1}	
G-protein parameters				
Constitutive activation rate constant of G	$k_{act,G}$	$1x10^{-6}$	cell/#/s	[3]
Forward rate constant of L12R4 binding to G	$kf_{b,G,L12R4}$	$1x10^{-3}$	cell/#/s	
Reverse rate constant of L12R4 and G binding	$kr_{b,G,L12}$	1	s^{-1}	[2]
Activation rate constant of L12R4G to L12R4Ga	$k_{act,L12R4G}$	$1x10^{-3}$	s^{-1}	[2]
Detachment rate of Ga from L`14	$k_{detach,Ga}$	$1x10^{1}$	s^{-1}	[2]
Constitutive deactivation of Ga to G	$k_{deact,Ga}$	$1x10^{-4}$	s^{-1}	[2]

Table 4.2 continued

Receptor phosphorylation				
Forward rate constant of phosphorylation of R4 by GRKs	kp_{R4}	$1x10^{-3}$	s^{-1}	^
Reverse phosphorylation rate constant of R4p	kp_{L12R4}	$1x10^{-5}$	s^{-1}	^
Forward rate constant of phosphorylation of L12R4 by GRKs	kp_{L12R4}	$1x10^{-2}$	s^{-1}	^
Reverse phosphorylation rate constant of L12R4p	kp_{L12R4p}	$1x10^{-4}$	s^{-1}	^
Forward rate constant of phosphorylation of R7 by GRKs	kp_{R7}	1	s^{-1}	^
Reverse phosphorylation rate constant of R7p	kp_{L12R7p}	$1x10^{-3}$	s^{-1}	^
Forward rate constant of phosphorylation of L12R7 by GRKs	kp_{L12R7}	1	s^{-1}	^
Reverse phosphorylation rate constant of L12R7p	$kdep_{L12R7}$	$1x10^{-3}$	s^{-1}	^
ERK signaling				
Constitutive activation of gpERK	$v_{act,gpERK}$	$1x10^{-4}$	s^{-1}	[3]
Activation of gpERK by G protein	kp_{gpERK}	$1x10^{-4}$	cell/#/s	[3]
Dephosphorylation of gpERK	$k_{dephos,gpERK}$	$2x10^{-3}$	s^{-1}	[3]
Translocation of gpERK to the nucleus	ke_{gpERK}	$1x10^{-3}$	s^{-1}	[3]
Constitutive activation of bpERK	$k_{act,bpERK}$	$1x10^{-4}$	s^{-1}	[3]
Activation of bpERK by β-arrestins	kp_{bpERK}	$1x10^{-4}$	cell/#/s	[3]
Dephosphorylation of bpERK	$k_{dephos,bpERK}$	$1x10^{-1}$	s^{-1}	[3]

^ Denotes parameters determined in this work

Table 4.3 Event Rates

Ligand binding		
CXCL12 binding to R4 $v_{b,L12,R4} = kf_{L12R4}(R4 \bullet L12 - KD_{L12R4}L12R4)$	CXCL12 binding to R7 $v_{b,L12,R7} = kf_{L12R7}(R7 \bullet L12 - KD_{L12R7}L12R7)$	CXCR7 inhibitor binding to R7 $v_{b,X,R7} = kf_{XR7}(R7 \bullet X - KD_{XR7}XR7)$
CXCL12 binding to R4p $v_{b,L12,R4p} = kf_{L12R4}(R4p \bullet L12 - KD_{L12R4B}L12R4p)$	CXCL12 binding to R7p $v_{b,L12,R7p} = kf_{L12R7}(R7p \bullet L12 - KD_{L12R7B}L12R7p)$	CXCR7 inhibitor binding to R7p $v_{b,X,R7p} = kf_{XR7}(R7p \bullet X - KD_{XR7B}XR7p)$
CXCL12 binding to R4B $v_{b,L12,R4B} = kf_{L12R4}(R4B \bullet L12 - KD_{L12R4B}L12R4B)$	CXCL12 binding to R7B $v_{b,L12.R7B} = kf_{L12R7}(R7B \bullet L12 - KD_{L12R7B}L12R7B)$	CXCR7 inhibitor binding to R7B $v_{b,X.R7B} = kf_{XR7}(R7B \bullet X - KD_{XR7B}XR7B)$
Receptor phosphorylation by GRKs		
Phosphorylation of R4 $v_{p,R4} = kp_{R4}R4$	Phosphorylation of R7 $v_{p,R7} = kp_{R7}R7$	
Phosphorylation of L12R4 $v_{p,L12R4} = kp_{L12R4}L12R4$	Phosphorylation of L12R7 $v_{p,L12R7} = kp_{L12R7}L12R7$	Phosphorylation of XR7 $v_{p,XR7} = kp_{XR7}XR7$
β-arrestin binding		
B binding to R4p $v_{b,B,R4p} = kf_{BR4}(R4p \bullet B - KD_{BR4} \bullet R4B)$	B binding to R7p $v_{b,B,R7p} = kf_{BR7}(R7p \bullet B - KD_{BR7} \bullet R7B)$	
B binding to L12R4p $v_{b,B,L12R4p} = kf_{BR4}(L12R4p \bullet B - KD_{BL12R4} \bullet L12R4B)$	B binding to L12R7p $v_{b,B,L12R7p} = kf_{BR7}(L12R7p \bullet B - KD_{BL12R7} \bullet L12R7B)$	B binding to XR7p $v_{b,B,XR7p} = kf_{BR7}(XR7p \bullet B - KD_{XR7B} \bullet XR7B)$
Receptor internalization		
Internalization of R4B $v_{i,R4B} = ke_{R4B}R4B$	Internalization of R7B $v_{i,R7B} = ke_{R7B}R7B$	
Internalization of L12R4B $v_{i,L12R4B} = ke_{L12R4B}L12R4B$	Internalization of L12R7B $v_{i,L12R7B} = ke_{L12R7B}L12R7B$	Internalization of XR7B $v_{i,XR7B} = ke_{XR7B}XR7B$
β-arrestin dissociation		
Dissociation of B from L12R4Bi $v_{off,L12R4Bi} = koff_{BR4}L12R4Bi$	Dissociation of B from R7Bi $v_{off,R7Bi} = koff_{BR7}R7Bi$	
Trafficking, recycling, and degradation		
	Trafficking of L12R7Bi to late endosomes $v_{tr,L12R7Bi} = ke_{L12R7Bi}L12R7Bi$	Trafficking of XR7Bi to late endosomes $v_{tr,XR7Bi} = ke_{XR7Bi}XR7Bi$
Recycling of R4Bi $v_{rec,R4Bi} = krec_{R4Bi}R4Bi$	Recycling of R7Bii $v_{rec,R7Bii} = krec_{R7Bi}R7Bii$	
Degradation of L12R4Bii $v_{deg,L12R4Bi} = kdeg_{L12R4Bi}L12R4Bii$	Recycling of L12R7Bii $v_{rec,L12R7Bii} = krec_{L12R7Bii}L12R7Bii$	Recycling of XR7Bii $v_{rec,XR7Bii} = krec_{XR7Bii}XR7Bii$
Degradation of CXCL12i $v_{deg,L12i} = kdeg_{L12}L12i$		Degradation of CXCR7 inhibitor $v_{deg,Xi} = kdeg_{X}Xi$

Table 4.3 continued

G protein signaling	*G protein-mediated ERK signaling*	*β-arrestin-mediated ERK signaling*
Constitutive activation of G protein $v_{act,G} = k_{act,G}G$	Phosphorylation of ERK by G proteins $v_{p,gpERK} = kp_{gpERK}Ga \bullet ERK$	Phosphorylation of ERK by L12R7Bi $v_{p,bpERK,7} = kp_{gpERK,7}L12R7Bi \bullet ERK$
Binding of L12R4 to G $v_{b,G,L12R4} = kf_{b,G,L12R4}G \bullet L12R4 - kr_{b,G,L12}L12R4G$	Dephosphorylation of gpERK $v_{dephos,gpERK} = k_{dephos,gpERK}Ga \bullet ERK$	Dephosphorylation of bpERK $v_{dephos,bpERK} = k_{dephos,bpERK}bpERK$
Activation of receptor-bound G protein $v_{act,L12R4G} = k_{act,L12R4G}L12R4G$	Translocation of gpERK to the nucleus $v_{tr,gpERK} = ke_{gpERK}gpERK$	Constitutive activation of bpERK $v_{act,bpERK} = k_{act,bpERK}ERK$
Detachment of Ga from L2R4 $v_{detach,Ga} = k_{detach,Ga}L12R4Ga$	Constitutive activation of gpERK $v_{act,gpERK} = k_{act,gpERK}ERK$	
Deactivation of activated G protein $v_{deact,Ga} = k_{deact,Ga}Ga$		

Table 4.4 Differential Equations

Extracellular ligand	
$dL12/dt = (- v_{b,L12,R4} - v_{b,L12,R4p} - v_{b,L12,R4B} - v_{b,L12,R7} - v_{b,L12,R7p} - v_{b,L12,R7B}) \bullet (n \bullet 10^9 / (Nav \bullet V))$	
$dX/dt = (-v_{b,X,R7} - v_{b,X,R7p} - v_{b,X.R7B}) \bullet (n \bullet 10^9 / (Nav \bullet V))$	
CXCR4 and CXCR7	
$dR4/dt = - v_{b,L12,R4} - v_{p,R4} + v_{rec,R4Bi}$	$dR7/dt = - v_{b,L12,R7} - v_{p,R7} + v_{rec,R7Bii} + v_{rec,L12R7Bii} - v_{b,X,R7} + v_{rec,XR7Bii}$
$dR4B/dt = - v_{b,L12,R4B} + v_{b,B,R4p} - v_{i,R4B}$	$dR7B/dt = - v_{b,L12.R7B} + v_{b,B,R7p} - v_{i,R7B}$
$dL12R4/dt = v_{b,L12,R4} - v_{b,G,L12R4} - v_{p,L12R4} + v_{detach,Ga}$	$dL12R7/dt = v_{b,L12,R7} - v_{p,L12R7}$
$dL12R4B/dt = v_{b,L12,R4B} + v_{b,B,L12R4p} - v_{i,L12R4B}$	$dL12R7B/dt = v_{b,L12.R7B} + v_{b,B,L12R7p} - v_{i,L12R7B}$
$dR4p/dt = v_{p,R4} - v_{b,B,R4p} - v_{b,L12,R4p}$	$dR7p/dt = v_{p,R7} - v_{b,B,R7p} - v_{b,L12,R7p} - v_{b,X,R7p}$
$dL12R4p/dt = v_{p,L12R4} + v_{b,L12,R4p} - v_{b,B,L12R4p}$	$dL12R7p/dt = v_{p,L12R7} + v_{b,L12,R7p} - v_{b,B,L12R7p}$
$dL12R4G/dt = v_{b,G,L12R4} - v_{act,L12R4G}$	
$dL12R4Ga/dt = v_{act,L12R4G} - v_{detach,Ga}$	
$dR4Bi/dt = v_{i,R4B} - v_{rec,R4Bi}$	$dR7Bi/dt = v_{i,R7B} - v_{off,R7Bi}$
	$dR7Bii/dt = v_{off,R7Bi} - v_{rec,R7Bii}$
$dL12R4Bi/dt = v_{i,L12R4B} - v_{off,L12R4Bi}$	$dL12R7Bi/dt = v_{i,L12R7B} - v_{tr,L12R7Bi}$
$dL12R4Bii/dt = v_{off,L12R4Bi} - v_{rec,R4Bi}$	$dL12R7Bii/dt = v_{tr,L12R7Bi} - v_{rec,L12R7Bii}$
	$dXR7/dt = v_{b,X,R7} - v_{p,XR7}$
	$dXR7B/dt = v_{b,B,XR7p} + v_{b,X.R7B} - v_{i,XR7B}$
	$dXR7p/dt = v_{p,XR7} + v_{b,X,R7p} - v_{b,B,XR7p}$
	$dXR7Bi/dt = v_{i,XR7B} - v_{tr,XR7Bi}$
	$dXR7Bii /dt = v_{off,XR7Bi} - v_{rec,XR7Bii}$
β-arrestin, G protein and ERK	
$dB/dt = - v_{b,B,R4p} - v_{b,B,L12R4p} + v_{i,R4B} + v_{off,L12R4Bi} - v_{b,B,R7p} - v_{b,B,L12R7p} + v_{off,R7Bi} + v_{rec,R7Bii} - v_{b,B,XR7p} + v_{rec,XR7Bii}$	
$dG/dt = - v_{b,G,L12R4} + v_{deact,Ga} - v_{act,G}$	$dERK/dt = - v_{act,gpERK} - v_{act,bpERK} - v_{p,gpERK} - v_{p,bpERK,7} + v_{dephos,gpERK} + v_{dephos,bpERK}$
$dGa/dt = v_{detach,Ga} + v_{act,G} - v_{deact,Ga}$	$dgpERK/dt = v_{act,gpERK} + v_{p,gpERK} - v_{dephos,gpERK} - v_{tr,gpERK}$
$dL12R4G/dt = v_{b,G,L12R4} - v_{act,L12R4G}$	$dbpERK/dt = v_{act,ERK} + v_{p,bpERK,7} - v_{dephos,bpERK}$
$dL12R4Ga/dt = v_{act,L12R4G} - v_{detach,Ga}$	$dnucERK/dt = v_{tr,gpERK}$

1. Coggins NL, Trakimas D, Chang SL, Ehrlich A, Ray P, et al. (2014) CXCR7 Controls Competition for Recruitment of beta-Arrestin 2 in Cells Expressing Both CXCR4 and CXCR7. PLoS One 9: e98328.
2. Kinzer-Ursem TL, Linderman JJ (2007) Both ligand- and cell-specific parameters control ligand agonism in a kinetic model of g protein-coupled receptor signaling. PLoS Comput Biol 3: e6.
3. Heitzler D, Durand G, Gallay N, Rizk A, Ahn S, et al. (2012) Competing G protein-coupled receptor kinases balance G protein and beta-arrestin signaling. Molecular Systems Biology 8: 590.
4. Sasagawa S, Ozaki Y, Fujita K, Kuroda S (2005) Prediction and validation of the distinct dynamics of transient and sustained ERK activation. Nat Cell Biol 7: 365-373.
5. Naumann U, Cameroni E, Pruenster M, Mahabaleshwar H, Raz E, et al. (2010) CXCR7 functions as a scavenger for CXCL12 and CXCL11. PLoS One 5: e9175.

4.7 Figures

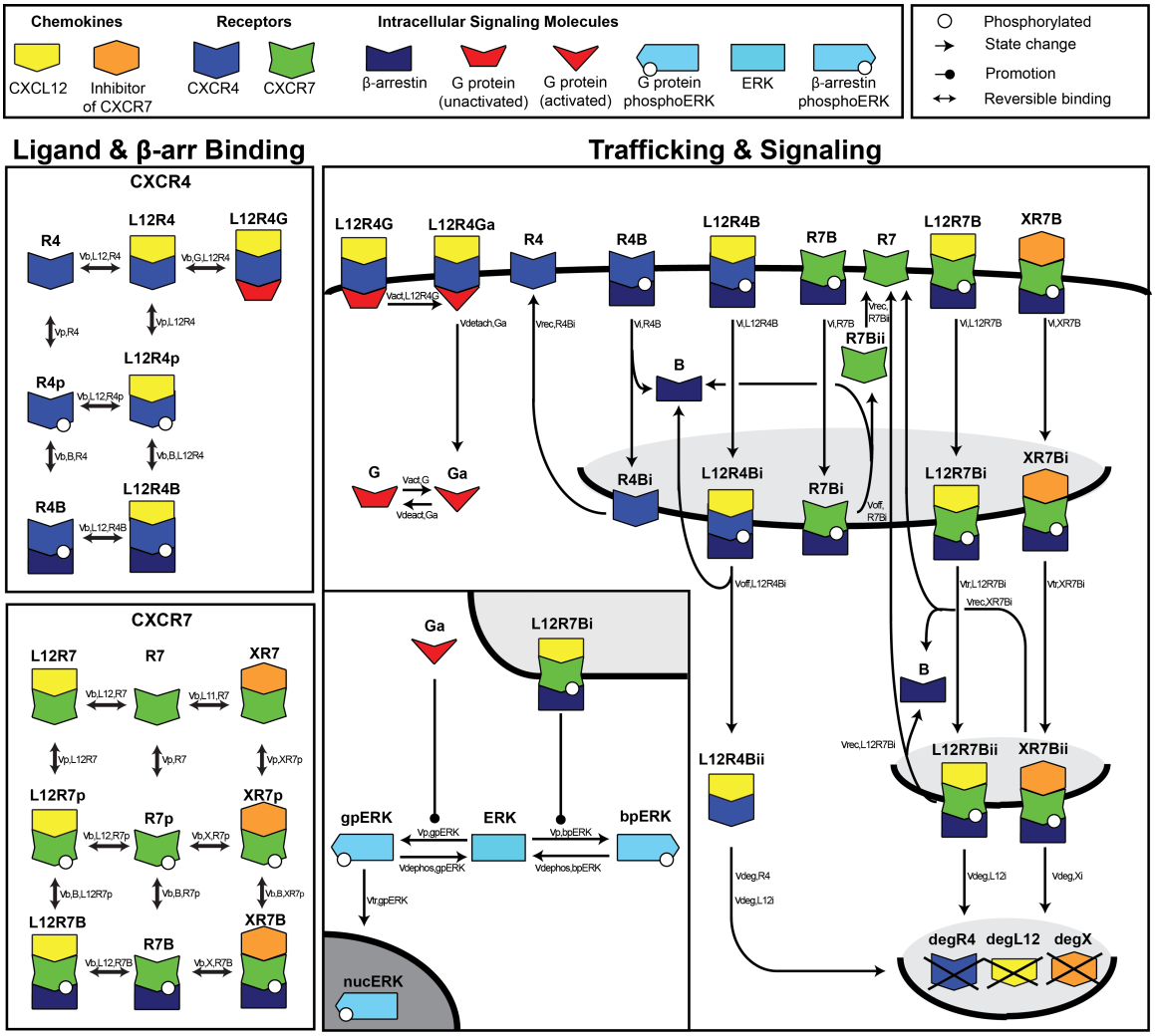

Figure 4.1 Competition within the CXCL12/CXCR4/CXCR7 pathway

Model of competition control points within the CXCL12/CXCR4/CXCR7 signaling pathway. CXCR4 and CXCR7 ligand binding, β-arrestin binding, internalization and signaling to ERK via the G protein and beta-arrestin pathways are modeled using ordinary differential equations based on mass action kinetics.

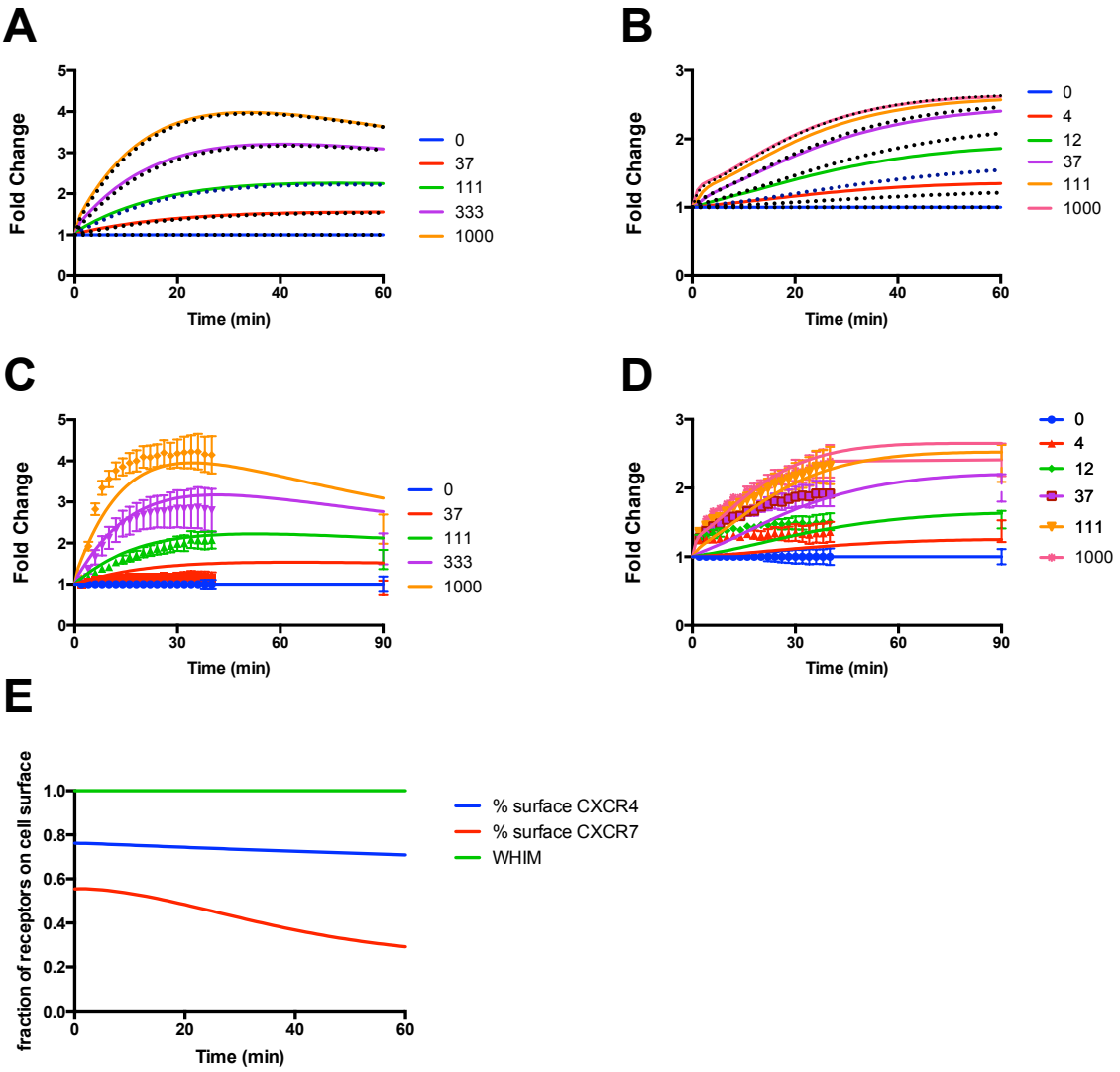

Figure 4.2 Model validation

Fold change of CXCR4 (A) and CXCR7 (B) interaction with β-arrestin as calculated by the first generation model (colored solid lines) and the model in this work (black dotted lines superimposed on the first generation model lines). Receptor phosphorylation parameters were fit to match β-arrestin interaction data. Note that for the 0 nM concentration, the data from both models overlap with a fold change of 1. Experimental data of CXCR4 (C) and CXCR7 (D) interaction with β-arrestin (dots with error bars, as reported in [28]) to the model in this work (solid lines) shows that the model is in agreement with experimental measurements of β -arrestin dynamics. All initial conditions and rate constants are identical with those described in [28]. (E) Consistent with experimental observations, CXCR4 remains primarily on the surface and CXCR7 is primarily intracellular after ligand addition (10nM). Simulation of WHIM syndrome ($kf_{B,R4p}$ and $kf_{B,C4p} = 0$) results in increased CXCR4 surface expression.

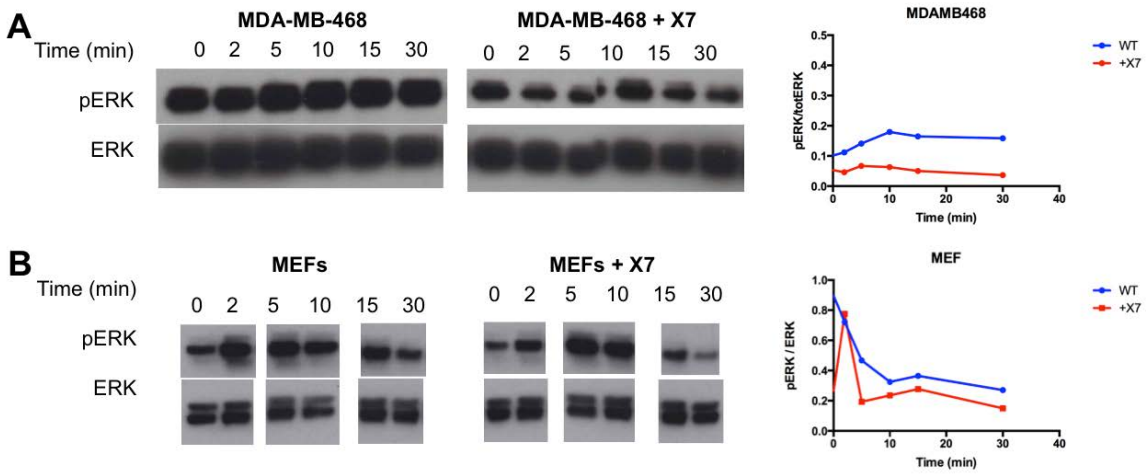

Figure 4.3 Co-expression of CXCR7 reduces overall pERK levels in MDA-MB-468 and MEFs

Western time courses with 100ng/ml of CXCL12 for (A) MDA-MB-468 and (B) mouse embryonic fibroblasts characterized by film and IVIS.

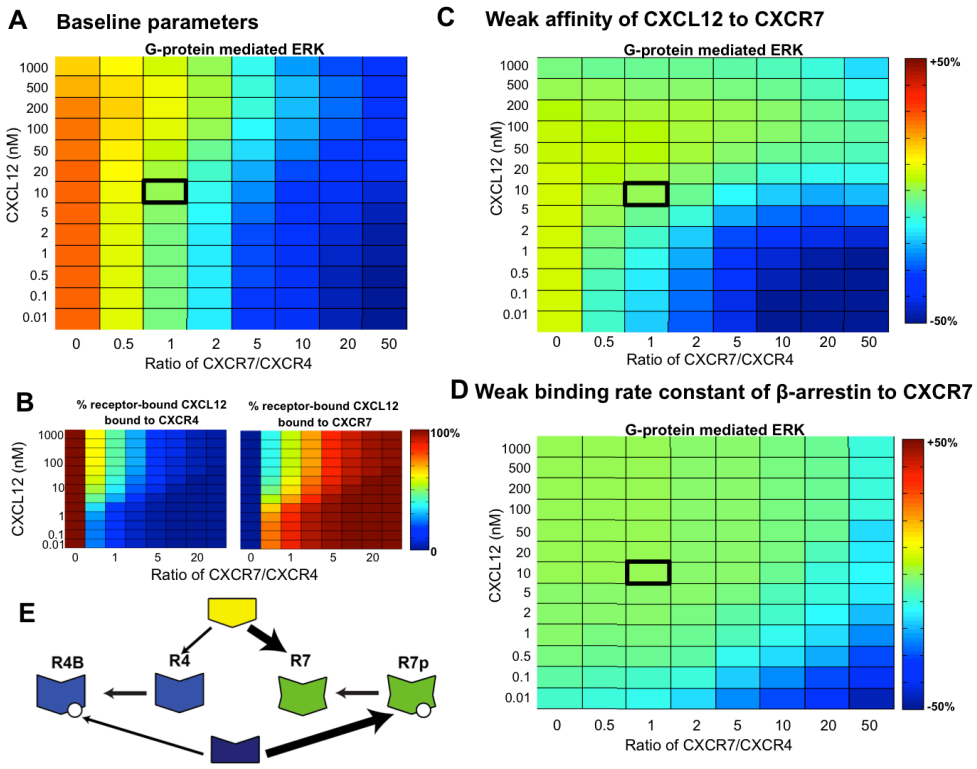

Figure 4.4 Co-expression of CXCR7 decreases G-protein signaling by sequestering CXCL12

(A) G-protein-mediated phosphorylated ERK (integrated over the first 30 minutes after ligand addition) decreases with increased CXCR7 expression with CXCR4. (B) As CXCR7 expression increases, an increasing proportion of receptor-bound CXCL12 is bound to CXCR7. (C) Reducing the affinity of CXCL12 to CXCR7 by two orders of magnitude ($Kd_{L12,R7}$ increased to 80 from 0.8) alleviates the strong dependence on CXCR7 expression. (D) Similarly, reducing the affinity of β-arrestin to CXCR7 ($kf_{b,B,R7}$ decreased and $KD_{B,R7}$ increased by two orders of magnitude) reduces strong dependence on CXCR7 expression. (E) CXCR7 scavenges both CXCL12 and β-arrestin from CXCR4. Panels outlined in dark black indicate the baseline CXCL12 and CXCR7 parameters as listed in Tables 4.1 - 4.4. Colorbars for gpERK are % change from baseline parameters.

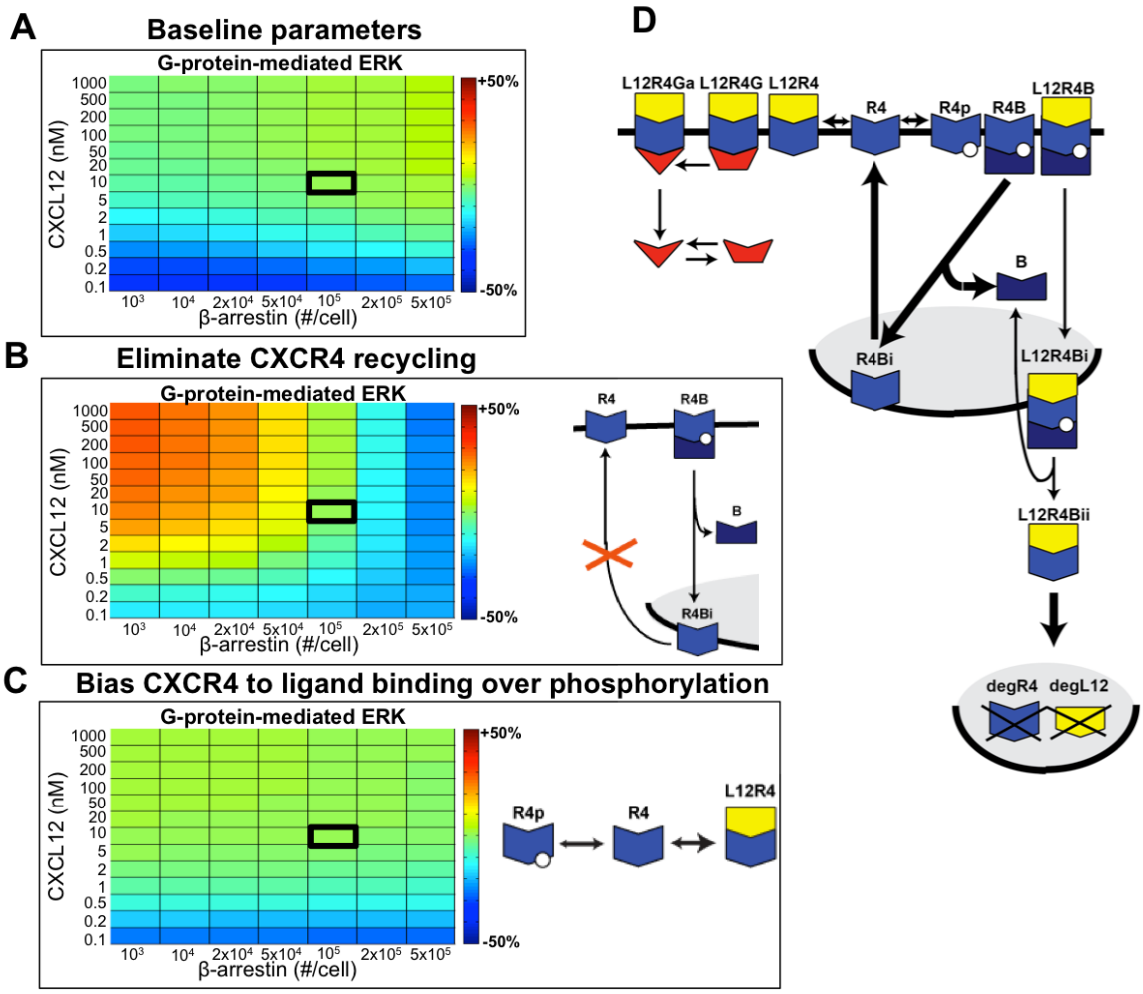

Figure 4.5 CXCR4 recycling and rapid phosphorylation enhances CXCR4-mediated G protein signaling

(A) G-protein-mediated phosphorylated ERK (integrated over the first 30 minutes after ligand addition) increased with increasing β-arrestin. (B) Eliminating recycling of CXCR4 ($krec_{R4Bi} = 0$) shifts the pattern and gpERK decreases with increasing β-arrestin. (C) Biasing CXCR4 to ligand binding over phosphorylation ($kf_{L12R4} = 0.01$, $kp_{R4} = 10^{-4}$, $kp_{C4} = 10^{-6}$) removes the dependence on β-arrestin levels. (D) CXCR4 recycling and rapid phosphorylation drive β-arrestin-dependent effects on CXCR4 signaling. Panels outlined in dark black indicate the baseline CXCL12 and β-arrestin parameters. Colorbars for gpERK are % change from baseline parameters.

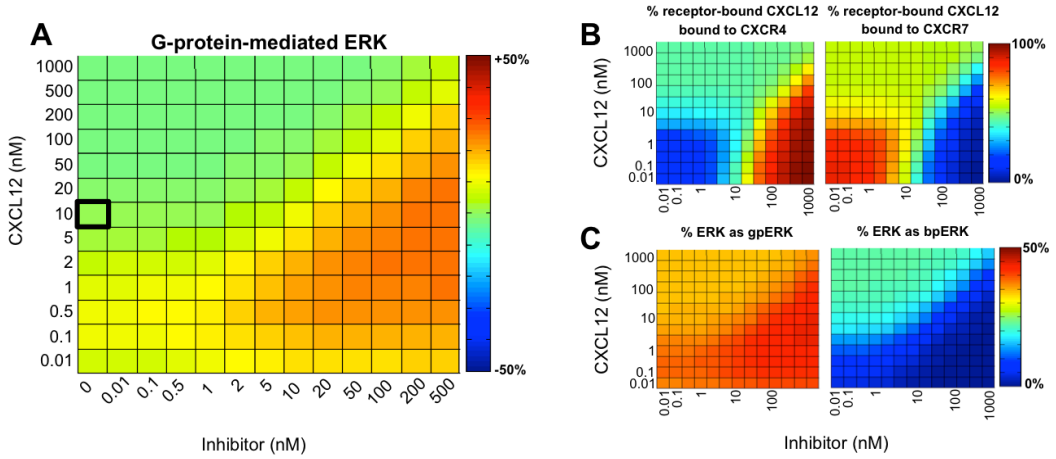

Figure 4.6 Addition of CXCR7 inhibitor

(A) Increasing CXCR7 inhibitor concentration increasing G-protein signaling at low CXCL12 concentrations, but at higher CXCL12 concentrations, CXCL12 is no longer limiting and CXCR7 sequesters both CXCL12 and ERK. (B) Plotting the percent of receptor-bound CXCL12 bound to CXCR4 vs. CXCR7 reveals three regions. At low CXCL12 and low inhibitor concentrations, CXCR7 sequesters CXCL12. At low CXCL12 and high inhibitor concentrations, CXCR4 no longer competes with CXCR7 and binds CXCL12. At high CXCL12 concentrations, CXCL12 is no longer limiting. (C) In addition, at high CXCL12 concentrations, ERK available to be phosphorylated by the G-protein pathway is sequestered by CXCR7.
Panels outlined in dark black indicate the baseline CXCL12 and β-arrestin parameters. Colorbars for gpERK are % change from baseline parameters.

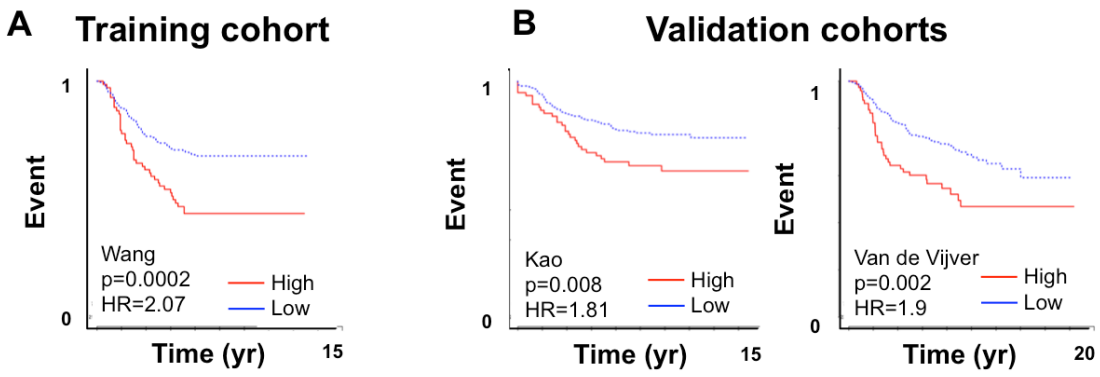

Gene	CXCL12	CXCR4	CXCR7
Hazard Ratio (e^b)	0.853	0.926	1.186
p	2.1E-2	0.23 (n.s.)	1.8E-4

Figure 4.7 Cox proportional hazards model of CXCL12, CXCR4, CXCR7 expression in cancer

The three-gene Cox proportional hazards model was fit to publicly available data from Wang (A) and independently validated in two clinical cohorts (B).

4.8 References

1. Chen M, Li D, Krebs EG, Cooper JA. The casein kinase II beta subunit binds to Mos and inhibits Mos activity. Molecular and cellular biology. 1997;17(4):1904-12. Epub 1997/04/01. PubMed PMID: 9121438; PubMed Central PMCID: PMC232037.
2. Wynn ML, Ventura AC, Sepulchre JA, Garcia HJ, Merajver SD. Kinase inhibitors can produce off-target effects and activate linked pathways by retroactivity. BMC systems biology. 2011;5:156. Epub 2011/10/06. doi: 10.1186/1752-0509-5-156. PubMed PMID: 21970676; PubMed Central PMCID: PMC3257213.
3. Kim SY, Ferrell JE, Jr. Substrate competition as a source of ultrasensitivity in the inactivation of Wee1. Cell. 2007;128(6):1133-45. Epub 2007/03/27. doi: 10.1016/j.cell.2007.01.039. PubMed PMID: 17382882.
4. Rowland MA, Fontana W, Deeds EJ. Crosstalk and competition in signaling networks. Biophys J. 2012;103(11):2389-98. Epub 2013/01/04. doi: 10.1016/j.bpj.2012.10.006. PubMed PMID: 23283238; PubMed Central PMCID: PMC3514525.
5. Rajagopal S, Rajagopal K, Lefkowitz RJ. Teaching old receptors new tricks: biasing seven-transmembrane receptors. Nature reviews Drug discovery. 2010;9(5):373-86. Epub 2010/05/01. doi: 10.1038/nrd3024. PubMed PMID: 20431569; PubMed Central PMCID: PMC2902265.
6. Heitzler D, Durand G, Gallay N, Rizk A, Ahn S, Kim J, et al. Competing G protein-coupled receptor kinases balance G protein and beta-arrestin signaling. Mol Syst Biol. 2012;8:590. Epub 2012/06/28. doi: 10.1038/msb.2012.22. PubMed PMID: 22735336; PubMed Central PMCID: PMC3397412.
7. Balkwill F. Cancer and the chemokine network. Nature reviews Cancer. 2004;4(7):540-50. Epub 2004/07/02. doi: 10.1038/nrc1388. PubMed PMID: 15229479.
8. Balabanian K, Lagane B, Infantino S, Chow KY, Harriague J, Moepps B, et al. The chemokine SDF-1/CXCL12 binds to and signals through the orphan receptor RDC1 in T lymphocytes. The Journal of biological chemistry. 2005;280(42):35760-6. Epub 2005/08/19. doi: 10.1074/jbc.M508234200. PubMed PMID: 16107333.
9. Chu QD, Holm NT, Madumere P, Johnson LW, Abreo F, Li BD. Chemokine receptor CXCR4 overexpression predicts recurrence for hormone receptor-positive, node-negative breast cancer patients. Surgery. 2011;149(2):193-9. Epub 2010/07/06. doi: 10.1016/j.surg.2010.05.016. PubMed PMID: 20598333.
10. Chu QD, Panu L, Holm NT, Li BD, Johnson LW, Zhang S. High chemokine receptor CXCR4 level in triple negative breast cancer specimens predicts poor clinical outcome. The Journal of surgical research. 2010;159(2):689-95. Epub 2009/06/09. doi: 10.1016/j.jss.2008.09.020. PubMed PMID: 19500800.
11. Hassan S, Ferrario C, Saragovi U, Quenneville L, Gaboury L, Baccarelli A, et al. The influence of tumor-host interactions in the stromal cell-derived factor-1/CXCR4 ligand/receptor axis in determining metastatic risk in breast cancer. The American journal of pathology. 2009;175(1):66-73. Epub 2009/06/06. doi: 10.2353/ajpath.2009.080948. PubMed PMID: 19497995; PubMed Central PMCID: PMC2708795.
12. Holm NT, Byrnes K, Li BD, Turnage RH, Abreo F, Mathis JM, et al. Elevated levels of chemokine receptor CXCR4 in HER-2 negative breast cancer specimens predict recurrence. The Journal of surgical research. 2007;141(1):53-9. Epub 2007/06/19. doi: 10.1016/j.jss.2007.03.015. PubMed PMID: 17574038.
13. Muller A, Homey B, Soto H, Ge N, Catron D, Buchanan ME, et al. Involvement of chemokine receptors in breast cancer metastasis. Nature. 2001;410(6824):50-6. Epub 2001/03/10. doi: 10.1038/35065016. PubMed PMID: 11242036.
14. Salvucci O, Bouchard A, Baccarelli A, Deschenes J, Sauter G, Simon R, et al. The role of CXCR4 receptor expression in breast cancer: a large tissue microarray study. Breast cancer research and treatment. 2006;97(3):275-83. Epub 2005/12/14. doi: 10.1007/s10549-005-9121-8. PubMed PMID: 16344916.
15. Zhao H, Guo L, Zhao H, Zhao J, Weng H, Zhao B. CXCR4 over-expression and survival in cancer: A system review and meta-analysis. Oncotarget. 2014. Epub 2015/02/12. PubMed PMID: 25669980.
16. Lagane B, Chow KY, Balabanian K, Levoye A, Harriague J, Planchenault T, et al. CXCR4 dimerization and beta-arrestin-mediated signaling account for the enhanced chemotaxis to CXCL12 in

WHIM syndrome. Blood. 2008;112(1):34-44. Epub 2008/04/26. doi: 10.1182/blood-2007-07-102103. PubMed PMID: 18436740.
17. Luker KE, Gupta M, Luker GD. Imaging CXCR4 signaling with firefly luciferase complementation. Analytical chemistry. 2008;80(14):5565-73. Epub 2008/06/07. doi: 10.1021/ac8005457. PubMed PMID: 18533683.
18. Rubin JB. Chemokine signaling in cancer: one hump or two? Seminars in cancer biology. 2009;19(2):116-22. Epub 2008/11/11. doi: 10.1016/j.semcancer.2008.10.001. PubMed PMID: 18992347; PubMed Central PMCID: PMC2694237.
19. Sun X, Cheng G, Hao M, Zheng J, Zhou X, Zhang J, et al. CXCL12 / CXCR4 / CXCR7 chemokine axis and cancer progression. Cancer metastasis reviews. 2010;29(4):709-22. Epub 2010/09/15. doi: 10.1007/s10555-010-9256-x. PubMed PMID: 20839032; PubMed Central PMCID: PMC3175097.
20. Sun Y, Cheng Z, Ma L, Pei G. Beta-arrestin2 is critically involved in CXCR4-mediated chemotaxis, and this is mediated by its enhancement of p38 MAPK activation. The Journal of biological chemistry. 2002;277(51):49212-9. Epub 2002/10/09. doi: 10.1074/jbc.M207294200. PubMed PMID: 12370187.
21. Teicher BA, Fricker SP. CXCL12 (SDF-1)/CXCR4 pathway in cancer. Clinical cancer research : an official journal of the American Association for Cancer Research. 2010;16(11):2927-31. Epub 2010/05/21. doi: 10.1158/1078-0432.CCR-09-2329. PubMed PMID: 20484021.
22. Rajagopal S, Kim J, Ahn S, Craig S, Lam CM, Gerard NP, et al. Beta-arrestin- but not G protein-mediated signaling by the "decoy" receptor CXCR7. Proceedings of the National Academy of Sciences of the United States of America. 2010;107(2):628-32. Epub 2009/12/19. doi: 10.1073/pnas.0912852107. PubMed PMID: 20018651; PubMed Central PMCID: PMC2818968.
23. Decaillot FM, Kazmi MA, Lin Y, Ray-Saha S, Sakmar TP, Sachdev P. CXCR7/CXCR4 heterodimer constitutively recruits beta-arrestin to enhance cell migration. The Journal of biological chemistry. 2011;286(37):32188-97. Epub 2011/07/07. doi: 10.1074/jbc.M111.277038. PubMed PMID: 21730065; PubMed Central PMCID: PMC3173186.
24. Levoye A, Balabanian K, Baleux F, Bachelerie F, Lagane B. CXCR7 heterodimerizes with CXCR4 and regulates CXCL12-mediated G protein signaling. Blood. 2009;113(24):6085-93. Epub 2009/04/22. doi: 10.1182/blood-2008-12-196618. PubMed PMID: 19380869.
25. Sierro F, Biben C, Martinez-Munoz L, Mellado M, Ransohoff RM, Li M, et al. Disrupted cardiac development but normal hematopoiesis in mice deficient in the second CXCL12/SDF-1 receptor, CXCR7. Proceedings of the National Academy of Sciences of the United States of America. 2007;104(37):14759-64. Epub 2007/09/07. doi: 10.1073/pnas.0702229104. PubMed PMID: 17804806; PubMed Central PMCID: PMC1976222.
26. Hernandez L, Magalhaes MA, Coniglio SJ, Condeelis JS, Segall JE. Opposing roles of CXCR4 and CXCR7 in breast cancer metastasis. Breast cancer research : BCR. 2011;13(6):R128. Epub 2011/12/14. doi: 10.1186/bcr3074. PubMed PMID: 22152016; PubMed Central PMCID: PMC3326570.
27. Zabel BA, Wang Y, Lewen S, Berahovich RD, Penfold ME, Zhang P, et al. Elucidation of CXCR7-mediated signaling events and inhibition of CXCR4-mediated tumor cell transendothelial migration by CXCR7 ligands. J Immunol. 2009;183(5):3204-11. Epub 2009/07/31. doi: 10.4049/jimmunol.0900269. PubMed PMID: 19641136.
28. Coggins NL, Trakimas D, Chang SL, Ehrlich A, Ray P, Luker KE, et al. CXCR7 Controls Competition for Recruitment of beta-Arrestin 2 in Cells Expressing Both CXCR4 and CXCR7. PloS one. 2014;9(6):e98328. Epub 2014/06/05. doi: 10.1371/journal.pone.0098328. PubMed PMID: 24896823.
29. Sanchez-Martin L, Sanchez-Mateos P, Cabanas C. CXCR7 impact on CXCL12 biology and disease. Trends in molecular medicine. 2013;19(1):12-22. Epub 2012/11/17. doi: 10.1016/j.molmed.2012.10.004. PubMed PMID: 23153575.
30. Luker KE, Gupta M, Luker GD. Imaging chemokine receptor dimerization with firefly luciferase complementation. FASEB journal : official publication of the Federation of American Societies for Experimental Biology. 2009;23(3):823-34. Epub 2008/11/13. doi: 10.1096/fj.08-116749. PubMed PMID: 19001056; PubMed Central PMCID: PMC2653984.
31. Kufareva I, Stephens BS, Holden LG, Qin L, Zhao C, Kawamura T, et al. Stoichiometry and geometry of the CXC chemokine receptor 4 complex with CXC ligand 12: molecular modeling and experimental validation. Proceedings of the National Academy of Sciences of the United States of America. 2014;111(50):E5363-72. Epub 2014/12/04. doi: 10.1073/pnas.1417037111. PubMed PMID: 25468967; PubMed Central PMCID: PMC4273337.

32. Drury LJ, Ziarek JJ, Gravel S, Veldkamp CT, Takekoshi T, Hwang ST, et al. Monomeric and dimeric CXCL12 inhibit metastasis through distinct CXCR4 interactions and signaling pathways. Proceedings of the National Academy of Sciences of the United States of America. 2011;108(43):17655-60. Epub 2011/10/13. doi: 10.1073/pnas.1101133108. PubMed PMID: 21990345; PubMed Central PMCID: PMC3203819.
33. Veldkamp CT, Peterson FC, Pelzek AJ, Volkman BF. The monomer-dimer equilibrium of stromal cell-derived factor-1 (CXCL 12) is altered by pH, phosphate, sulfate, and heparin. Protein science : a publication of the Protein Society. 2005;14(4):1071-81. Epub 2005/03/03. doi: 10.1110/ps.041219505. PubMed PMID: 15741341; PubMed Central PMCID: PMC2253449.
34. Ray P, Lewin SA, Mihalko LA, Lesher-Perez SC, Takayama S, Luker KE, et al. Secreted CXCL12 (SDF-1) forms dimers under physiological conditions. The Biochemical journal. 2012;442(2):433-42. Epub 2011/12/07. doi: 10.1042/BJ20111341. PubMed PMID: 22142194.
35. Vila-Coro AJ, Rodriguez-Frade JM, Martin De Ana A, Moreno-Ortiz MC, Martinez AC, Mellado M. The chemokine SDF-1alpha triggers CXCR4 receptor dimerization and activates the JAK/STAT pathway. FASEB journal : official publication of the Federation of American Societies for Experimental Biology. 1999;13(13):1699-710. Epub 1999/10/03. PubMed PMID: 10506573.
36. Luker KE, Gupta M, Steele JM, Foerster BR, Luker GD. Imaging ligand-dependent activation of CXCR7. Neoplasia. 2009;11(10):1022-35. Epub 2009/10/02. PubMed PMID: 19794961; PubMed Central PMCID: PMC2745668.
37. Balabanian K, Levoye A, Klemm L, Lagane B, Hermine O, Harriague J, et al. Leukocyte analysis from WHIM syndrome patients reveals a pivotal role for GRK3 in CXCR4 signaling. The Journal of clinical investigation. 2008;118(3):1074-84. Epub 2008/02/16. doi: 10.1172/JCI33187. PubMed PMID: 18274673; PubMed Central PMCID: PMC2242619.
38. Busillo JM, Armando S, Sengupta R, Meucci O, Bouvier M, Benovic JL. Site-specific phosphorylation of CXCR4 is dynamically regulated by multiple kinases and results in differential modulation of CXCR4 signaling. The Journal of biological chemistry. 2010;285(10):7805-17. Epub 2010/01/06. doi: 10.1074/jbc.M109.091173. PubMed PMID: 20048153; PubMed Central PMCID: PMC2844224.
39. Lefkowitz RJ, Shenoy SK. Transduction of receptor signals by beta-arrestins. Science. 2005;308(5721):512-7. Epub 2005/04/23. doi: 10.1126/science.1109237. PubMed PMID: 15845844.
40. Zhang WB, Navenot JM, Haribabu B, Tamamura H, Hiramatu K, Omagari A, et al. A point mutation that confers constitutive activity to CXCR4 reveals that T140 is an inverse agonist and that AMD3100 and ALX40-4C are weak partial agonists. The Journal of biological chemistry. 2002;277(27):24515-21. Epub 2002/03/30. doi: 10.1074/jbc.M200889200. PubMed PMID: 11923301.
41. Samama P, Cotecchia S, Costa T, Lefkowitz RJ. A mutation-induced activated state of the beta 2-adrenergic receptor. Extending the ternary complex model. The Journal of biological chemistry. 1993;268(7):4625-36. Epub 1993/03/05. PubMed PMID: 8095262.
42. Spalding TA, Burstein ES. Constitutive activity of muscarinic acetylcholine receptors. Journal of receptor and signal transduction research. 2006;26(1-2):61-85. Epub 2006/04/06. doi: 10.1080/10799890600567349. PubMed PMID: 16595339.
43. Zhao M, Discipio RG, Wimmer AG, Schraufstatter IU. Regulation of CXCR4-mediated nuclear translocation of extracellular signal-related kinases 1 and 2. Molecular pharmacology. 2006;69(1):66-75. Epub 2005/10/08. doi: 10.1124/mol.105.016923. PubMed PMID: 16210428.
44. Ahn S, Shenoy SK, Wei H, Lefkowitz RJ. Differential kinetic and spatial patterns of beta-arrestin and G protein-mediated ERK activation by the angiotensin II receptor. The Journal of biological chemistry. 2004;279(34):35518-25. Epub 2004/06/19. doi: 10.1074/jbc.M405878200. PubMed PMID: 15205453.
45. Fricker SP, Anastassov V, Cox J, Darkes MC, Grujic O, Idzan SR, et al. Characterization of the molecular pharmacology of AMD3100: a specific antagonist of the G-protein coupled chemokine receptor, CXCR4. Biochemical pharmacology. 2006;72(5):588-96. Epub 2006/07/04. doi: 10.1016/j.bcp.2006.05.010. PubMed PMID: 16815309.
46. Wang Y, Klijn JG, Zhang Y, Sieuwerts AM, Look MP, Yang F, et al. Gene-expression profiles to predict distant metastasis of lymph-node-negative primary breast cancer. Lancet. 2005;365(9460):671-9. Epub 2005/02/22. doi: 10.1016/S0140-6736(05)17947-1. PubMed PMID: 15721472.
47. Kao KJ, Chang KM, Hsu HC, Huang AT. Correlation of microarray-based breast cancer molecular subtypes and clinical outcomes: implications for treatment optimization. BMC cancer. 2011;11:143. Epub 2011/04/20. doi: 10.1186/1471-2407-11-143. PubMed PMID: 21501481; PubMed Central PMCID: PMC3094326.

48. van de Vijver MJ, He YD, van't Veer LJ, Dai H, Hart AA, Voskuil DW, et al. A gene-expression signature as a predictor of survival in breast cancer. The New England journal of medicine. 2002;347(25):1999-2009. Epub 2002/12/20. doi: 10.1056/NEJMoa021967. PubMed PMID: 12490681.
49. Reiter E, Lefkowitz RJ. GRKs and beta-arrestins: roles in receptor silencing, trafficking and signaling. Trends in endocrinology and metabolism: TEM. 2006;17(4):159-65. Epub 2006/04/06. doi: 10.1016/j.tem.2006.03.008. PubMed PMID: 16595179.
50. Andresen BT. Characterization of G protein-coupled receptor kinase 4 and measuring its constitutive activity in vivo. Methods in enzymology. 2010;484:631-51. Epub 2010/11/03. doi: 10.1016/B978-0-12-381298-8.00031-9. PubMed PMID: 21036254.
51. Miller WE, Houtz DA, Nelson CD, Kolattukudy PE, Lefkowitz RJ. G-protein-coupled receptor (GPCR) kinase phosphorylation and beta-arrestin recruitment regulate the constitutive signaling activity of the human cytomegalovirus US28 GPCR. The Journal of biological chemistry. 2003;278(24):21663-71. Epub 2003/04/02. doi: 10.1074/jbc.M303219200. PubMed PMID: 12668664.
52. Balabanian K, Lagane B, Pablos JL, Laurent L, Planchenault T, Verola O, et al. WHIM syndromes with different genetic anomalies are accounted for by impaired CXCR4 desensitization to CXCL12. Blood. 2005;105(6):2449-57. Epub 2004/11/13. doi: 10.1182/blood-2004-06-2289. PubMed PMID: 15536153.
53. Duda DG, Kozin SV, Kirkpatrick ND, Xu L, Fukumura D, Jain RK. CXCL12 (SDF1alpha)-CXCR4/CXCR7 pathway inhibition: an emerging sensitizer for anticancer therapies? Clinical cancer research : an official journal of the American Association for Cancer Research. 2011;17(8):2074-80. Epub 2011/02/26. doi: 10.1158/1078-0432.CCR-10-2636. PubMed PMID: 21349998; PubMed Central PMCID: PMC3079023.
54. Wurth R, Bajetto A, Harrison JK, Barbieri F, Florio T. CXCL12 modulation of CXCR4 and CXCR7 activity in human glioblastoma stem-like cells and regulation of the tumor microenvironment. Frontiers in cellular neuroscience. 2014;8:144. Epub 2014/06/07. doi: 10.3389/fncel.2014.00144. PubMed PMID: 24904289; PubMed Central PMCID: PMC4036438.
55. Zhao S, Chang SL, Linderman JJ, Feng FY, Luker GD. A Comprehensive Analysis of CXCL12 Isoforms in Breast Cancer. Translational oncology. 2014. Epub 2014/05/20. doi: 10.1016/j.tranon.2014.04.001. PubMed PMID: 24836649; PubMed Central PMCID: PMC4145355.
56. Mirisola V, Zuccarino A, Bachmeier BE, Sormani MP, Falter J, Nerlich A, et al. CXCL12/SDF1 expression by breast cancers is an independent prognostic marker of disease-free and overall survival. Eur J Cancer. 2009;45(14):2579-87. Epub 2009/08/04. doi: 10.1016/j.ejca.2009.06.026. PubMed PMID: 19646861.
57. Kamb A, Wee S, Lengauer C. Why is cancer drug discovery so difficult? Nature reviews Drug discovery. 2007;6(2):115-20. Epub 2006/12/13. doi: 10.1038/nrd2155. PubMed PMID: 17159925.
58. Hendrix CW, Collier AC, Lederman MM, Schols D, Pollard RB, Brown S, et al. Safety, pharmacokinetics, and antiviral activity of AMD3100, a selective CXCR4 receptor inhibitor, in HIV-1 infection. J Acquir Immune Defic Syndr. 2004;37(2):1253-62. Epub 2004/09/24. PubMed PMID: 15385732.
59. Miao Z, Luker KE, Summers BC, Berahovich R, Bhojani MS, Rehemtulla A, et al. CXCR7 (RDC1) promotes breast and lung tumor growth in vivo and is expressed on tumor-associated vasculature. Proceedings of the National Academy of Sciences of the United States of America. 2007;104(40):15735-40. Epub 2007/09/28. doi: 10.1073/pnas.0610444104. PubMed PMID: 17898181; PubMed Central PMCID: PMC1994579.
60. Torisawa YS, Mosadegh B, Bersano-Begey T, Steele JM, Luker KE, Luker GD, et al. Microfluidic platform for chemotaxis in gradients formed by CXCL12 source-sink cells. Integrative biology : quantitative biosciences from nano to macro. 2010;2(11-12):680-6. Epub 2010/09/28. doi: 10.1039/c0ib00041h. PubMed PMID: 20871938.
61. Cavnar SP, Ray P, Moudgil P, Chang SL, Luker KE, Linderman JJ, et al. Microfluidic source-sink model reveals effects of biophysically distinct CXCL12 isoforms in breast cancer chemotaxis. Integrative biology : quantitative biosciences from nano to macro. 2014. Epub 2014/03/29. doi: 10.1039/c4ib00015c. PubMed PMID: 24675873.
62. Dalle Nogare D, Somers K, Rao S, Matsuda M, Reichman-Fried M, Raz E, et al. Leading and trailing cells cooperate in collective migration of the zebrafish posterior lateral line primordium. Development. 2014;141(16):3188-96. Epub 2014/07/27. doi: 10.1242/dev.106690. PubMed PMID: 25063456; PubMed Central PMCID: PMC4197546.

63. Kang H, Watkins G, Parr C, Douglas-Jones A, Mansel RE, Jiang WG. Stromal cell derived factor-1: its influence on invasiveness and migration of breast cancer cells in vitro, and its association with prognosis and survival in human breast cancer. Breast cancer research : BCR. 2005;7(4):R402-10. Epub 2005/07/01. doi: 10.1186/bcr1022. PubMed PMID: 15987445; PubMed Central PMCID: PMC1175055.
64. Cabioglu N, Sahin A, Doucet M, Yavuz E, Igci A, E OY, et al. Chemokine receptor CXCR4 expression in breast cancer as a potential predictive marker of isolated tumor cells in bone marrow. Clinical & experimental metastasis. 2005;22(1):39-46. Epub 2005/09/01. doi: 10.1007/s10585-005-3222-y. PubMed PMID: 16132577.

Chapter 5

Ruffles restrict diffusion in the plasma membrane during macropinosome formation

5.1 Abstract

In murine macrophages stimulated with Macrophage-Colony-stimulating Factor (M-CSF), signals essential to macropinosome formation are restricted to the domain of plasma membrane enclosed within cup-shaped, circular ruffles. Consistent with a role for these actin-rich structures in signal amplification, microscopic measures of Rac1 activity determined that disruption of actin polymerization by latrunculin B inhibited ruffling and the localized activation of Rac1 in response to M-CSF. To test the hypothesis that circular ruffles restrict the lateral diffusion of membrane proteins that are essential for signaling, we monitored diffusion of membrane-tethered, photoactivatable green fluorescent protein (PAGFP-MEM) in ruffling and non-ruffling regions of cells. Although diffusion within macropinocytic cups was not inhibited, circular ruffles retained photoactivated PAGFP-MEM inside cup domains. Confinement of membrane molecules by circular ruffles could explain how actin facilitates positive feedback amplification of Rac1 in these relatively large domains of plasma membrane, thereby organizing the contractile activities that close macropinosomes.

5.2 Introduction

In response to stimulation by growth factors, many cells extend actin-rich, circular ruffles that close into endocytic vacuoles called macropinosomes. Macropinocytosis begins with deformation of the plasma membrane by actin-based motile activities, first into linear or curved ruffles, then into cup shaped circular ruffles at the cell surface [1]. This ruffle closure is followed by cup closure, in which the circular ruffle constricts at its distal margin and separates from the plasma membrane as a macropinosome inside the cell [2].

Previous studies identified molecules that regulate macropinocytosis, including phosphatidylinositol 3'-kinase (PI3K) and Rac1 [2-4]. Activated growth factor receptors recruit and activate type I PI3K, which generates phosphatidylinositol 3,4,5-trisphosphate (PIP3) in the inner leaflet of the plasma membrane. Inhibitors of PI3K allow ruffle closure but inhibit cup closure [3,5], indicating that PIP3 directs the late stage of macropinosome formation. Rac1 is requisite in the macrophage ruffling response to macrophage colony-stimulating factor (M-CSF) [6,7].

How are the movements of the actin cytoskeleton organized to close cup-shaped extensions into intracellular vesicles? Concentrated PIP3 or Rac1 in the macropinocytic cup could regulate actin-myosin-based contractions that close the cup. Imaging of signaling in response to M-CSF showed that PIP3 generation and Rac1 activation closely follow ruffle closure and are confined within circular ruffles [4]. This indicates that circular ruffles create domains of plasma membrane that facilitate signal amplification and the contractile activities of cup closure. We hypothesize that molecules necessary for Rac1 signal amplification are confined to circular ruffles by an actin-based diffusion barrier in the cup. We therefore conducted experiments to probe the existence and location of diffusion barriers in the inner leaflet of ruffling plasma membrane.

5.3 Methods

5.3.1 Cell culture

Bone marrow-derived macrophages (BMM) were generated as previously described [5,8]. Bone marrow exudate was obtained from femurs of C57BL/6J mice. Marrow was cultured in medium (DMEM with 20% FBS and 30% L cell-conditioned medium) promoting the differentiation of macrophages. Bone marrow cultures were differentiated for 1 week with additions of fresh differentiation medium at Days 3 and 6. Following differentiation, macrophages were transfected and plated onto 25-mm circular coverslips. Cultures were incubated overnight in medium lacking M-CSF (RPMI 1640 with 20% heat-inactivated FBS). All experiments were performed the day after plating.

5.3.2 Constructs and cell transfection

Fluorophores were localized to the inner leaflet of the plasma membrane using the membrane localization domain from neuromodulin (MEM), a protein that associates with membrane via prenylation [9]. BMMs were transfected with plasmids encoding PAGFP-MEM and mCherry-MEM via Amaxa Nucleofector II, using automated protocol Y-01. The conditions and reagents for macropinocytosis observation were 200 ng/mL MCSF (R&D Systems) in Ringer's Buffer (155 mM NaCl, 5 mM KCl, 2 mM CaCl2, 1 mM MgCl2, 2 mM NaH2PO4, 10 mM glucose and 10 mM HEPES at pH 7.2). In some experiments, Latrunculin B (5 μM) was added to cells five minutes before addition of M-CSF. All imaging experiments were temperature controlled at 37ºC.

5.3.3 XYT photoactivation experiments

Cells were imaged using an Olympus FV-500 Confocal microscope fitted with a 60x 1.45 NA oil immersion objective. The microscope was equipped with diode-pulse (for photoactivation), argon (for GFP imaging), and HeNe green (for mCherry imaging) lasers. Image collection used Fluoview FV500 imaging software. Images were acquired at 1 frame/second using line sequential scanning. Three pre-activation images were collected for each experiment: these images were averaged to provide a fluorescence baseline reading.

Photoactivation of PAGFP-MEM required one image scan with the diode laser set to

100% intensity. Photoactivation in defined regions of the cell membrane created patches of GFP fluorescence, whose fluorescence intensity decreased quickly by molecule diffusion in the membrane.

Fluorescence intensities and PAGFP/mCherry ratiometric images were quantified using the "region mean intensity" measurement function in MetaMorph (Molecular Dynamics, Sunnyvale, CA). The averaged pre-activation images established a baseline fluorescence that was subtracted from all post-activation images. A normalized fluorescence for each post-activation image was calculated by dividing its fluorescence by the initial post-activation timepoint fluorescence.

5.3.4 Computer modeling experiments

Three-dimensional models of the flat and cupped membranes were constructed using the transient diffusion module of COMSOL Multiphysics 3.4 (COMSOL Inc., Burlington, MA). The flat membrane (Figure 5.6A) was represented by two disks of 5.0 μm radius, r_o, and 0.05 μm thickness, t, representing the top and bottom layers of the membrane, respectively. The outer radius, r_o, was chosen to ensure that no molecules reached the outer edge of the model geometry during the time simulated. The cupped membrane (Figure 5.6B) was represented by a top layer geometry of an inner radius, r_i, of 1.1 μm; distance between inner and outer cup walls, w, of 150 nm; and cup height, h, variable from 0.5 μm to 5.0 μm. The membrane thickness, t, was 0.05 μm and the outer radius, r_o, was 5 μm. The bottom layer of the cupped membrane was represented by the same geometry as the flat membrane. COMSOL required specifying a membrane thickness to solve the cupped membrane, and this small value (0.05 μm) allowed us to mimic diffusion on the membrane surface. The software employs a finite element analysis to follow the time course of diffusion (solving $\frac{\partial c}{\partial t} + D\nabla^2 c = 0$, where c is concentration and D is the diffusion coefficient) and to calculate the concentration of molecules at each point within the model geometry as a function of time. The initial condition for each model was equal to 2000 molecules uniformly distributed within the activation spot (r_a = 1 μm), 1000 molecules each in the top and bottom membrane layers. To compare simulation results with the experimental data (normalized fluorescence ratio), the number of

molecules within the activation spot was calculated at each time point and the computational ratio, R, was calculated as: $R = \frac{top(t) + bottom(t)}{top(0) + bottom(0)}$, where top(t) and bottom(t) are the number of molecules within the activation spot at time t on the top and bottom membrane layers, respectively. Simulation results from a flat membrane were fit to experimental data and used to determine a diffusion coefficient, D, of 1.1 x 10^{-9} cm^2/s. D was then used in simulations with the cupped membrane.

5.3.5 XYZT photoactivation experiments

Three-dimensional reconstructions of membrane dynamics (XYZT) used the same microscope and software as the XYT experiments. Image Z-stacks used a step size of 250 nm between planes. Images were collected continuously in line sequential scanning mode. Collection of each Z-stack required approximately seven seconds. Image stacks were deconvolved using Huygens Essential software and the deconvolved stacks were visualized using the 4D viewer and linescan function in MetaMorph.

5.3.6 FRET Microscopy

Fluorescence images were collected using a Nikon Eclipse TE-300 inverted microscope with a 60x numerical aperture 1.4, oil-immersion PlanApo objective lens (Nikon, Tokyo, Japan) and a Lambda LS xenon arc lamp for epifluorescence illumination (Sutter Instruments, Novato, CA). Fluorescence excitation and emission wavelengths were selected using a JP4v2 filter set (Chroma Technology, Rockingham, VT) and a Lambda 10-2 filter wheel controller (Shutter Instruments) equipped with a shutter for epifluorescence illumination control. Images were recorded with a Photometrics CoolSnap HQ cooled CCD camera (Roper Scientific, Tucson, AZ). Image acquisition and processing were performed using MetaMorph v6.3 (Molecular Devices, Sunnyvale, CA). Additional processing was performed using MATLAB v7.8.0 (The MathWorks, Inc., Natick, MA) and the equations of FRET stoichiometry [10].

FRET microscopy of macrophages expressing Citrine-Rac1 and Cerulean-PBD was carried out as previously described [4,10]. Briefly, collected images were background-subtracted and shading-corrected. EA, ED, and Ratio images were then calculated using

published FRET stoichiometry equations [10,11]. G* images were calculated as previously described, using the coefficient values obtained from cells expressing Citrine-Rac1(L61) and Cerulean-PBD [12]. G* values account for varying levels of donor and acceptor in a population of cells, and can therefore be used to accurately measure the fraction of active Citrine-Rac1 in cells that express variable relative amounts of Cerulean-PBD and Citrine-Rac1. A paired two-tailed Student's t-test was used to compare average G* values from macropinocytic cups and entire cells.

5.4 Results

The relationship between actin-rich membrane ruffles and Rac1 signal amplification was examined by measuring the effect of the actin-depolymerizing agent latrunculin B on Rac1 activity. Quantitative Förster resonance energy transfer (FRET) microscopy was used to observe bone marrow-derived macrophages (BMM) expressing Citrine-Rac1 and Cerulean-PBD. PBD, derived from Pak1, binds the active (GTP-bound) form of Rac1 [13]. The citrine and cerulean chimeras produce significant FRET interactions in regions of the cell where Rac1 is active. FRET stoichiometry was used to determine G*, which is the fraction of activated Citrine- Rac1 in any given region of the image [12]. G* values in forming macropinosomes were higher than in the surrounding cytoplasm, indicating that Rac1 amplification was restricted to the cup domain (Figure 5.1A, C, and F). After M-CSF addition, cells treated with latrunculin B did not ruffle (Figure 5.1D) and the small increase of Rac1 activity was delocalized (Figure 5.1B and E). This indicated that Rac1 signal amplification in cups was actin-dependent.

To test the hypothesis that ruffles create barriers to diffusion in the inner leaflet of the plasma membrane, we measured the redistribution of plasma membrane-localized, photoactivatable green fluorescent protein (PAGFP-MEM), whose fluorescence following photoactivation increases 100-fold [14]. We first investigated whether ruffles could retain PAGFP-MEM near an initial region of photoactivation. Coexpression and imaging of monomeric Cherry (mCherry)-MEM chimeras provided a reference fluorescence that reported plasma membrane distribution. Ratiometric images, generated by dividing pixel values in the PAGFP-MEM images by the corresponding values in the

mCherry-MEM images, normalized PAGFP-MEM distribution in the various ruffling morphologies. We activated small patches of PAGFP-MEM molecules and measured the rates at which fluorescence intensity decreased by diffusion in the plasma membrane (Figure 5.2A). Curve-fitting analyses of fluorescence loss in flat regions of cells obtained a diffusion coefficient for PAGFP-MEM of $1.1x10^{-9}$ cm^2/sec (Figure 5.2B, Figure 5.6A and B). Near linear ruffles, diffusion of the activated molecules was slightly inhibited (Figure 5.2C). However, PAGFP-MEM activated inside circular ruffles was retained much more than PAGFP-MEM in flat or ruffled membrane (Figure 5.2D), indicating that ruffled surfaces created effective barriers to diffusion of PAGFP-MEM.

Quantitative measurements of the fluorescence depletion supported this observation (Figure 5.2E). The retention pattern for membrane cups leveled off approximately 15 seconds after activation, suggesting that activated molecules were retained in the activation region. The steep initial decline in fluorescence retention in all of the membrane structures could be explained by the fact that PAGFP-MEM molecules were photoactivated in both the top and bottom (i.e., substrate-adherent) membranes of the cells. Accordingly, plots of fluorescence depletion reflect the dynamics of PAGFP-MEM in both membranes, including the unrestricted diffusion in the flat, bottom membrane.

The apparent retention of PAGFP-MEM in the cup could be a consequence of its topography. Diffusion of PAGFP-MEM molecules activated inside membrane cups entails travel up the inner cup wall and down the outer cup wall. Apparent retention of activated PAGFP-MEM could simply reflect diffusion in the z-axis. However, simulations of diffusion in macropinocytic cups of various heights indicated that, in the absence of some type of barrier, diffusion in the z-axis would increase the retention of molecules in the activation spot only slightly (Figure 5.2F and 5.6C). The observed retention of PAGFP-MEM in cups could only be simulated by inclusion of a diffusion barrier (i.e., a region with a 10-100x lower diffusion coefficient) in the cup structure.

To verify that the circular structures we analyzed were not closed pinosomes, we visualized photoactivated PAGFP-MEM using through-focus image acquisition and 3D

reconstruction by image deconvolution. These experiments showed directly that open macropinocytic cups retained PAGFP-MEM. Activated PAGFP-MEM molecules were visible in macropinocytic cups at least 19.5 seconds after activation (Figs. 5.3A-C). Comparable 3D reconstructions of activated PAGFP-MEM in flat membrane regions showed rapid and complete loss of fluorescence.

Diffusion inside cups was further characterized using fluorescence intensity linescans of widefield microscopic images. Cherry-MEM linescans showed membrane contours. For open macropinocytic cups, the pixel intensities for Cherry-MEM were roughly equivalent inside and outside the cup, as fluorescence in each region derived from two layers of membrane (Figure 5.4A and B). In contrast, Cherry-MEM fluorescence from closed macropinosomes should include four layers of membrane: the top and bottom membranes of the cell plus the top and bottom membranes of the macropinosome. Accordingly, the Cherry-MEM pixel intensities measured from closed macropinosomes were 2.15 times the intensities of the surrounding area. This allowed us to use fluorescence linescans of Cherry-MEM images to confirm that all of the circular structures included in the quantification for Figure 5.2E were unclosed cups.

Fluorescence linescans also allowed us to measure the extent to which different membrane structures inhibited lateral diffusion of activated PAGFP-MEM. The initial fluorescence profiles for patches of activated PAGFP-MEM showed Gaussian distributions. In flat membrane, the intensity decreased rapidly to that of the surrounding plasma membrane (Figure 5.4D-F), suggesting that the activated molecules diffused out of the activation region. For circular ruffles, the intensity profiles in the activation region remained elevated (Figure 5.4C), indicating retention of the photoactivated PAGFP-MEM in the cup region.

Retention of activated PAGFP-MEM in macropinocytic cups could be explained either by decreased diffusivity throughout the entire cup or by barriers localized to the circular ruffles. To determine if diffusion in the base of the cup resembles diffusion outside of the cup, we activated PAGFP-MEM in subregions of the cup structures and observed

fluorescence redistribution within the cup. Imaging (Figure 5.5A) and intensity linescans (Figure 5.5B, C) of ratio fluorescence revealed that the initially asymmetrical activation profiles rapidly leveled off inside the cup. Modeling simulated PAGFP-MEM redistribution by creating an initially hemispherical cohort of activated molecules which redistributed with the diffusion coefficients of flat membrane (10^{-9} cm^2/sec) or barriers (10^{-11} cm^2/sec or 0 cm^2/sec) (Figure 5.5E, F). Diffusion barriers were assigned to different regions of the cup structure: the base, the inner wall, the distal rim, and combinations of those regions. The model most resembled the experimental data when the walls and rim of circular ruffles were assigned a barrier function and the base of the cup resembled flat membrane (Figure 5.5G, I). In contrast, simulations which assigned low diffusion coefficients to the base, walls and rim yielded did not resemble the observations (Figure 5.5 H, J). This is consistent with a mechanism in which proteins diffuse freely in the membrane of the base of the cup but encounter barriers in the ruffles.

5.5 Discussion

This study demonstrates that circular ruffles create barriers to protein diffusion in membranes. Unlike the diffusion barriers previously described for cleavage furrows [15] and the leading edge of cellular protrusions [16], the diffusion barriers of circular ruffles are capable of organizing microdomains for focused signal amplification.

The molecular basis of the barrier remains unknown. Diffusion of membrane proteins or phospholipids could be restricted at the distal margins of ruffles, either by specific fence-like structures that constrain the lateral movements of membrane-associated molecules or by physical constraints imposed by the high membrane curvature at the ruffle edge. In lipid rafts, tight packing of phospholipids reduces diffusivity [17]; raft-like structures at the distal margins of the macropinocytic cups could create effective barriers. Alternatively, the underlying actin meshwork could limit diffusion in the plasma membrane. The slight slowing of PAGFP-MEM diffusion observed in linear ruffles, relative to flat membrane (Figs. 2C, E), suggests that the barrier is intrinsic to ruffle structure. Actin or actin-associated proteins in ruffles could create effective barriers simply by slowing lateral diffusion of molecules along the broad face of the ruffle.

Regardless of its physical basis, the constraint on diffusion created by actin-rich ruffles could provide a mechanism for biasing signal amplification in self-organizing systems, leading to actin-dependent amplification of signals in ruffle-rich regions of the cell.

The efficacy of the barrier for signal amplification is maximized in the circular ruffle, where diffusion is inhibited in all directions. Functionally, as a patch of plasma membrane with amplified activity of signaling proteins [4], circular ruffle represents a novel signaling domain. Activated receptors recruit and activate lipid-modifying enzymes, such as PI3K, which recruit other enzymatic proteins to the membrane domain through the formation of lipid or phospholipid species. Absent barriers, diffusion in the membrane could dissipate receptor-generated signals to subthreshold levels and the initial activation signal would be unable to reach concentrations needed to activate later signals. Barriers could allow concentrations of lipids or activated GTPases to remain high, thereby allowing the cell to recruit or activate the molecules that actuate the late stages of signaling. Accordingly, the actin-dependent amplification of Rac1 within circular ruffles indicates a positive feedback amplification mechanism in which restricted movement of diffusible signaling intermediates allows their concentration in the plasma membrane to exceed some transition threshold. Similarly, transient increases of PIP3 that follow immediately after ruffle closure could locally activate guanine nucleotide exchange factors for Rac1 or other GTPases [4]. Conversely, by stimulating actin polymerization necessary for circular ruffle formation, Rac1 could amplify PI3K activity through an actin-dependent mechanism.

This mechanism of localizing signal amplification would be distinct from processes such as chemotaxis or phagocytosis, because it is independent of external orienting factors. Moreover, this focal signal amplification through restricted diffusion could provide a mechanism for cells to respond to lower concentrations of growth factor.

5.6 Figures

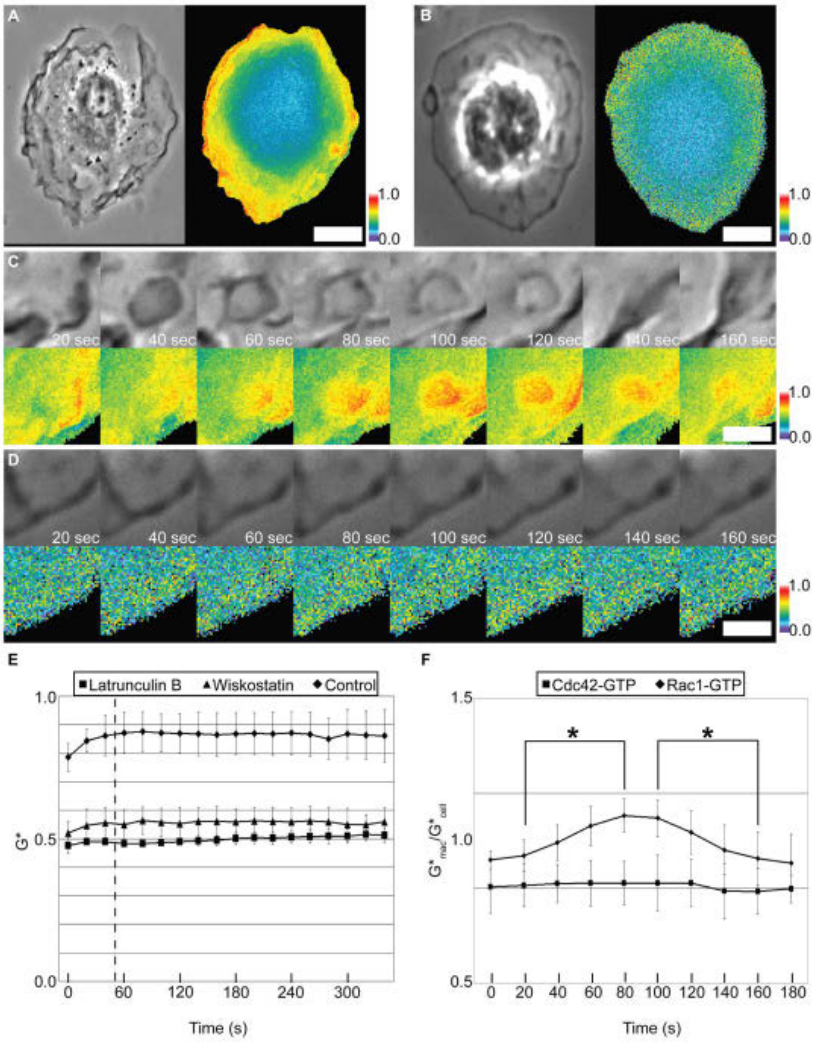

Figure 5.1 Focal activation of Rac1 during macropinocytosis

(A–D) FRET interactions of Cerulean-PBD and Citrine–Rac1 in control (A,C) and latrunculin B-treated BMM (B,D) in response to M-CSF. (A,B) Left: Phase contrast; right: *G**. Scale bars: 4 µm. (C,D) Time series for subregions of the cells shown in A and B, highlighting a forming macropinosome (C), and a comparable region of a latrunculin B-treated cell (D). Top row: Phase contrast; bottom row: *G**. Scale bars: 1 µm. All color bars indicate *G** values. (E) Quantification of total Citrine-Rac1 activity in control and latrunculin B- or wiskostatin-treated BMM (n=5 for all conditions). Dotted line indicates when M-CSF was added. (F) To quantify GTPase activation, the average *G** in a forming macropinosome was divided by the average *G** in the entire cell at each time point (n=10 for each). The resulting ratio indicates the relative change in GTPase activity in the forming macropinosomes, with numbers greater than 1.0 indicating localized increases in activity. Sequences were aligned by the timing of ruffle closure (t=60 seconds). Ratios for Rac1 were significantly higher than cytoplasm values (*P<0.001) from 80 to 100 seconds following the beginning of macropinosome formation. Ratios for Cdc42 did not significantly change during macropinosome formation. Error bars indicate s.d.

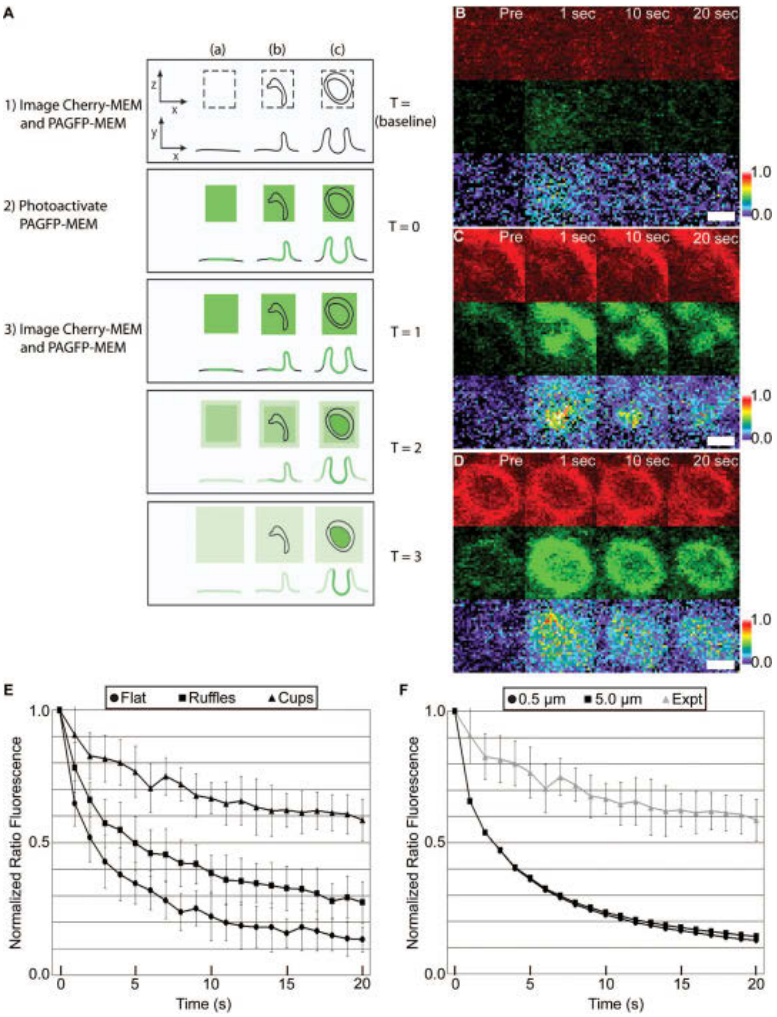

Figure 5.2 Selective photoactivation of PAGFP-MEM in plasma membranes

(A) Schematic of experimental protocol for XYT experiments. PAGFP-MEM was photoactivated in regions of flat (a), ruffled (b) or cupped membrane (c). Fluorescence intensities were collected in these activation regions over time. Loss of fluorescence indicated diffusion of activated PAGFP-MEM out of the activation region; conversely, retention of activated PAGFP-MEM indicated restricted diffusion. (B–D) Images of different macropinocytic structures. Top row, mCherry–MEM; middle row: PAGFP-MEM; bottom row, PAGFP:mCherry ratio. From left to right: 1 second pre-activation, 1 second post-activation, 10 seconds post-activation, 20 seconds post-activation. Scale bars: 1 µm. Color bars indicate relative fluorescence intensities of ratio images. (B) Photoactivation in flat membrane. (C) Photoactivation in ruffle membrane. (D) Photoactivation in a macropinocytic cup. (E) Quantification of the fluorescence decrease in plasma membrane (n=5 for each condition). Membrane ruffles and cups demonstrate significant retention of photoactivated PAGFP-MEM. (F) Modeling of the effects of cup height on probe retention. Increasing cup height without adding a barrier or decreasing the diffusion coefficient did not affect molecule retention and could not account for the experimental values. Error bars indicate s.d.

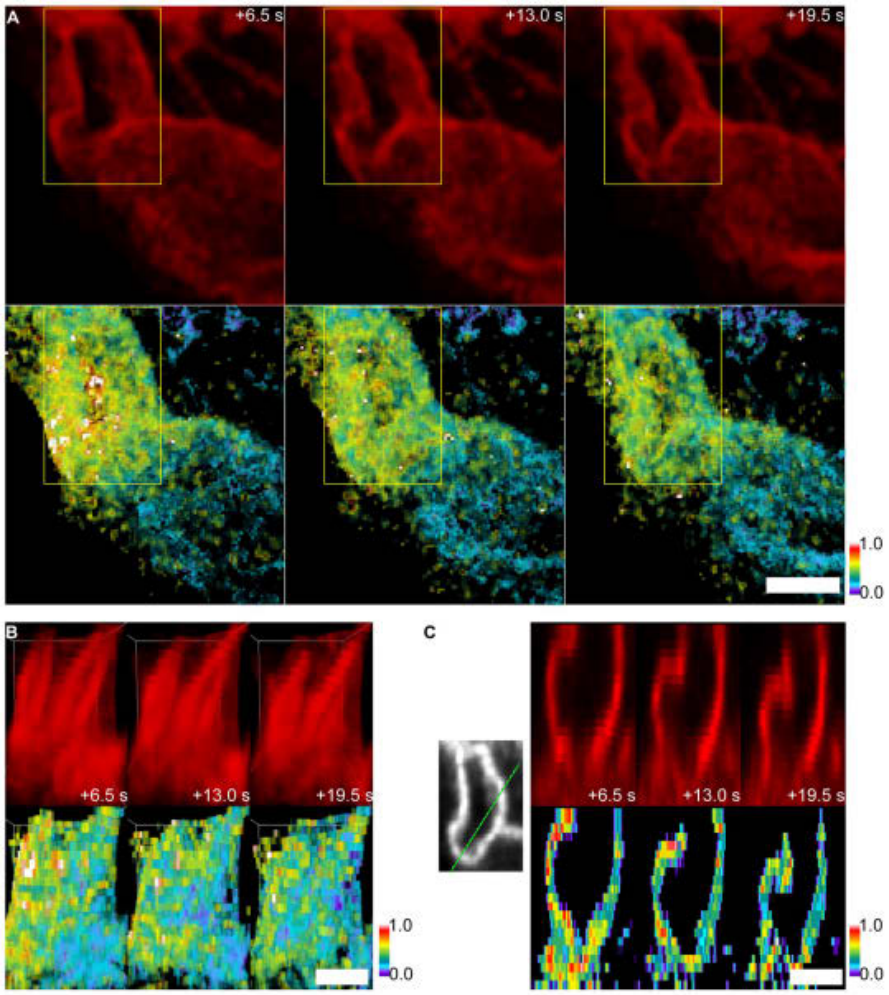

Figure 5.3 4D reconstruction of activated PAGFP-MEM in an open macropinocytic cup

Through-focus z-stacks were collected of PAGFP-MEM and mCherry at regular intervals after photoactivation of PAGFP-MEM in a cup. (A,B) Projections of a macropinocytic cup. Top row: mCherry–MEM; bottom row: PAGFP:mCherry ratio. From left to right: 6.5, 13.0 and 19.5 seconds after activation of PAGFP-MEM. (A) XY projection of a macropinocytic cup and surrounding cellular region. Yellow boxes delineate the macropinocytic cup. (B) XZ projections of the macropinocytic cup (side view). Fields correspond to the regions marked by the yellow boxes in A. (C) Cross-sections of macropinocytic cups showing distribution of mCherry–MEM (red) and PAGFP:mCherry ratio (pseudocolor) at 13 seconds after photoactivation of PAGFP-MEM. Green line shows region of cross-section. Color bars indicate relative fluorescence intensities of ratio images. Scale bars: 1.0 μm.

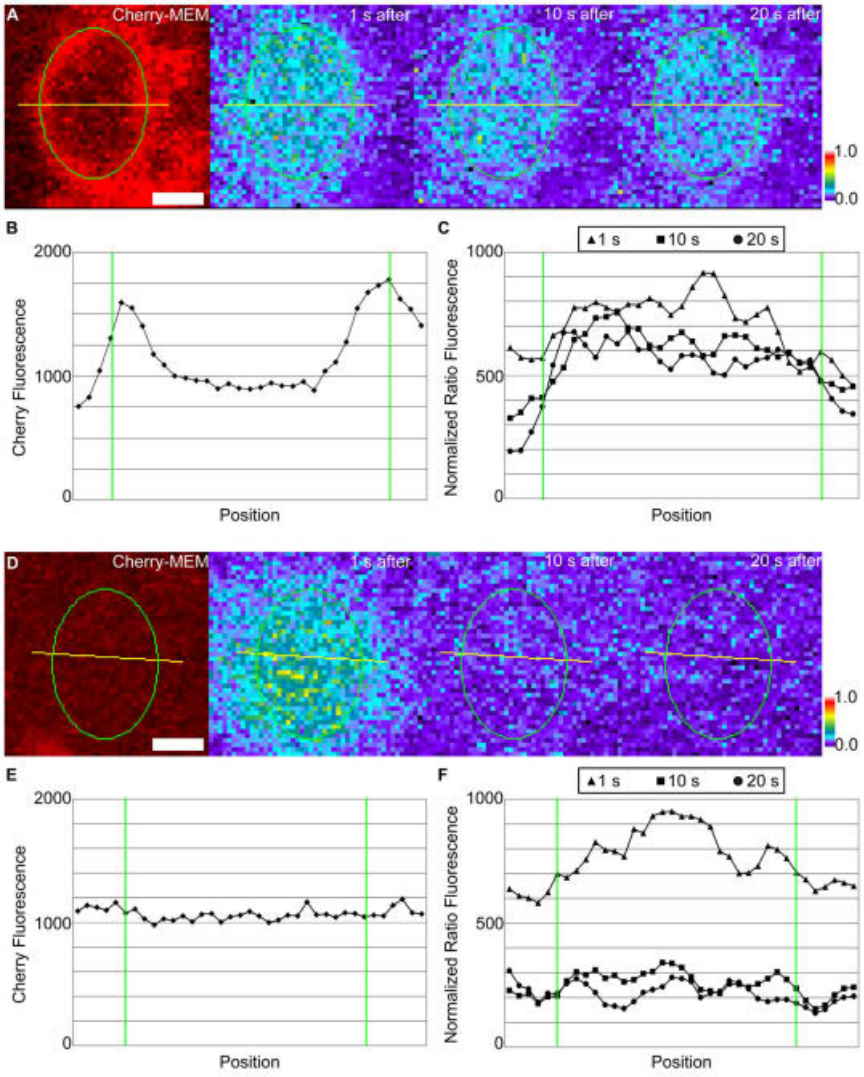

Figure 5.4 Fluorescence intensity linescans of cupped or flat membrane

(A,D) Representative linescans (yellow lines) in cupped and flat membrane, respectively. From left to right: mCherry–MEM image 1 second prior to activation, PAGFP:mCherry ratio image 1 second after activation, ratio image 10 seconds after activation, ratio image 20 seconds after activation. Scale bars: 1.0 μm. Color bars indicate relative fluorescence intensities of ratio images. (B,E) Linescans of mCherry–MEM fluorescence intensities in cupped and flat membrane, respectively. (C,F) Linescans of PAGFP/mCherry fluorescence ratios in cupped and flat membrane, respectively, at 1, 10 and 20 seconds after photoactivation. Green lines indicate the perimeter of the activation region. Similar fluorescence patterns were seen for seven macropinocytic cups and for ten regions of flat membrane.

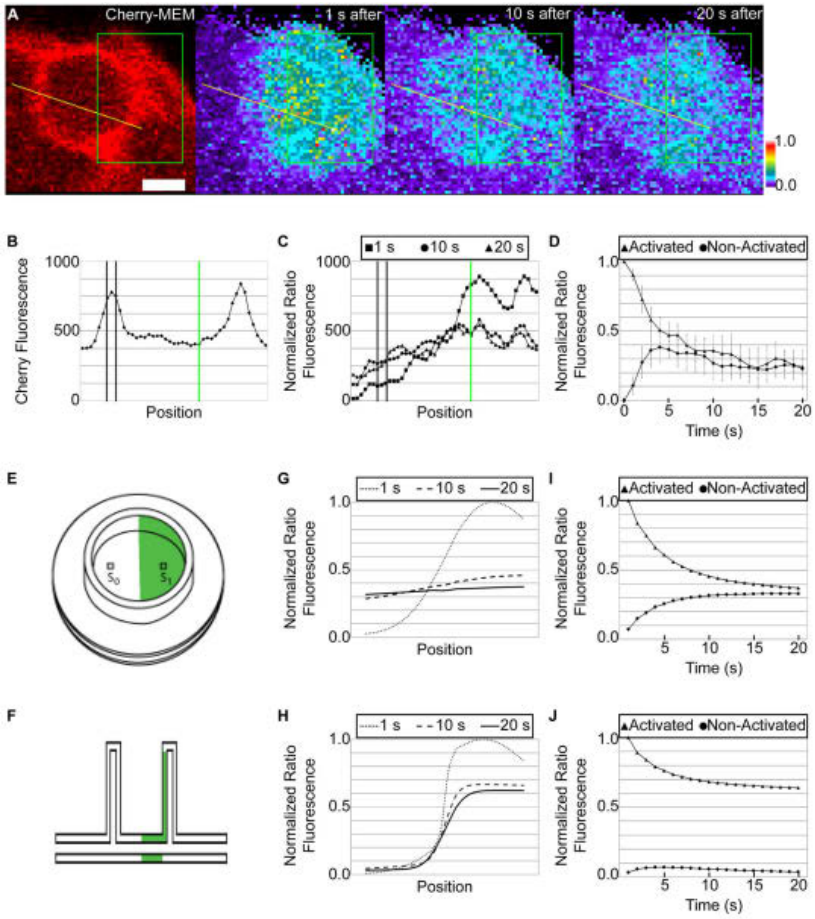

Figure 5.5 Diffusion dynamics within membrane cups indicate that the barrier localizes to the cup walls

(A–C) Fluorescence redistribution following asymmetric activation of PAGFP-MEM in macropinocytic cups. (A) Representative images. From left to right: mCherry–Mem image 1 second prior to activation, PAGFP:mCherry ratio images 1, 10 and 20 seconds after activation. Yellow lines indicate position of linescans. Green boxes indicate the perimeter of the activation region. Scale bar: 1.0 μm. Color bars indicate relative fluorescence intensities of ratio images. (B) Linescan measurements of mCherry–MEM pixel intensities. (C) Linescan measurements of PAGFP:mCherry ratio values at 1, 10, and 20 seconds after photoactivation. Similar fluorescence patterns were seen in five macropinocytic cups. Paired vertical lines indicate the location of the cup wall. Green lines indicate the edge of the activation region. (D) Fluorescence measurements of activated and non-activated regions in the base of the cup over time, n=5. (E–J) Modeling of diffusion within cups. (E,F) Diagrams of activation patterns used to model diffusion inside the cup, showing views from above (C) and in sagital section (F). (G,H) Distributions of molecules along the diameter of the base of the cup normal to the activation boundary, measured at 1, 10 and 20 seconds after activation. (G) When the diffusion coefficient in the walls is 10^{-11} cm^2/second (i.e., a barrier) and in the base of the cup is 10^{-9} cm^2/second, fluorophore redistribution resembles the experimental data in C. (H) When the diffusion coefficients of the walls and base are both set to

10^{-11} cm^2/second, fluorophore redistribution does not resemble the experimental data. (I,J) Modeling of the time course of fluorophore decrease from the activated region (triangles) and increase in the non-activated region (circles) when diffusion coefficients are set as in G (I) and H (J). The model resembles the experimental observations in D when the base of the cup has the same diffusion coefficient as membrane outside the cup (I).

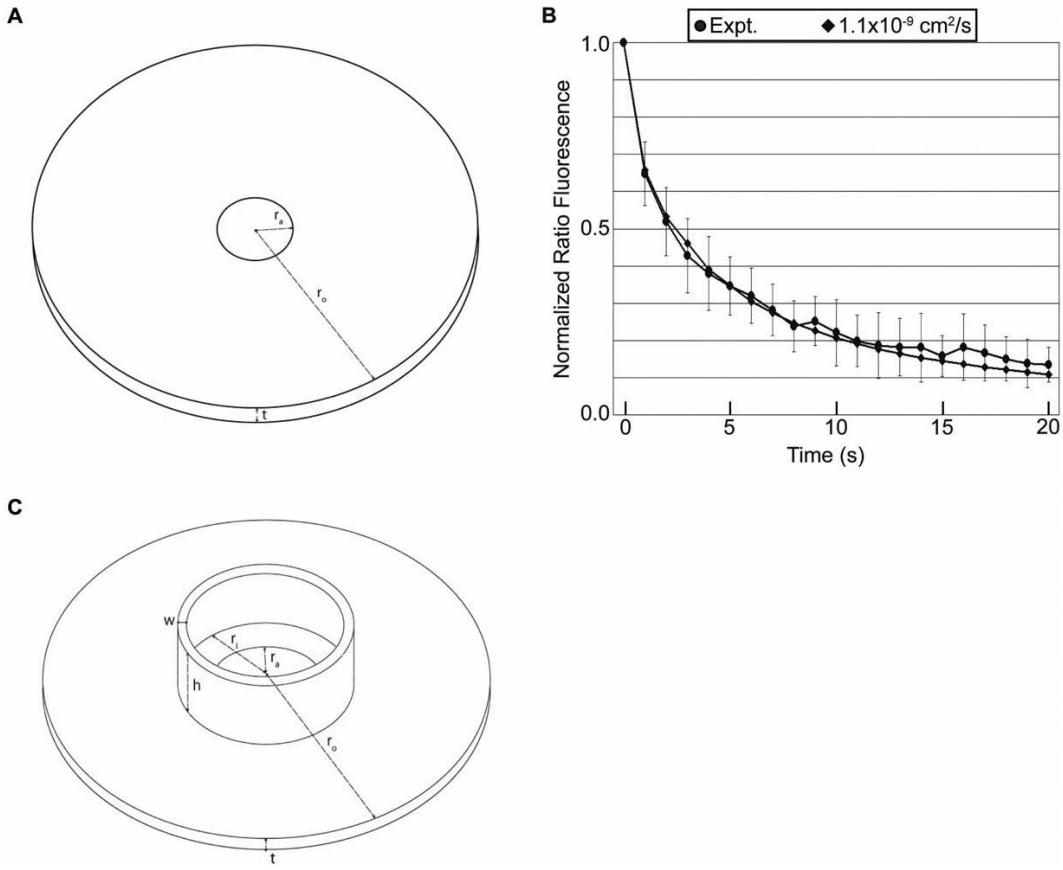

Figure 5.6 Construction of flat and cupped membrane models

(A) Flat membranes were modeled as three dimensional disks with an distinct region in the center to represent the membrane that is initially photoactivated. (B) By fitting the computational ratio to experimental flat membrane data, we determined that the diffusivity coefficient of plasma membrane-bound molecules is 1.1×10^{-9} cm^2/s. (C) Cupped membrane geometry.

5.7 References

1. Swanson JA (2008) Shaping cups into phagosomes and macropinosomes. Nat Rev Mol Cell Biol 9: 639-649.
2. Li G, D'Souza-Schorey C, Barbieri MA, Cooper JA, Stahl PD (1997) Uncoupling of membrane ruffling and pinocytosis during Ras signal transduction. J Biol Chem 272: 10337-10340.
3. Araki N, Johnson MT, Swanson JA (1996) A role for phosphoinositide 3-kinase in the completion of macropinocytosis and phagocytosis by macrophages. J Cell Biol 135: 1249-1260.
4. Yoshida S, Hoppe AD, Araki N, Swanson JA (2009) Sequential signaling in plasma-membrane domains during macropinosome formation in macrophages. J Cell Sci 122: 3250-3261.
5. Araki N, Hatae T, Furukawa A, Swanson JA (2003) Phosphoinositide-3-kinase-independent contractile activities associated with Fcgamma-receptor-mediated phagocytosis and macropinocytosis in macrophages. J Cell Sci 116: 247-257.
6. Cox D, Chang P, Zhang Q, Reddy PG, Bokoch GM, et al. (1997) Requirements for both Rac1 and Cdc42 in membrane ruffling and phagocytosis in leukocytes. J Exp Med 186: 1487-1494.
7. Wells CM, Walmsley M, Ooi S, Tybulewicz V, Ridley AJ (2004) Rac1-deficient macrophages exhibit defects in cell spreading and membrane ruffling but not migration. J Cell Sci 117: 1259-1268.
8. Swanson JA (1989) Phorbol esters stimulate macropinocytosis and solute flow through macrophages. J Cell Sci 94 (Pt 1): 135-142.
9. Moriyoshi K, Richards LJ, Akazawa C, O'Leary DD, Nakanishi S (1996) Labeling neural cells using adenoviral gene transfer of membrane-targeted GFP. Neuron 16: 255-260.
10. Hoppe A, Christensen K, Swanson JA (2002) Fluorescence resonance energy transfer-based stoichiometry in living cells. Biophysical Journal 83: 3652-3664.
11. Beemiller P, Hoppe AD, Swanson JA (2006) A phosphatidylinositol-3-kinase-dependent signal transition regulates ARF1 and ARF6 during Fcgamma receptor-mediated phagocytosis. PLoS Biol 4: e162.
12. Hoppe AD, Swanson JA (2004) Cdc42, Rac1, and Rac2 display distinct patterns of activation during phagocytosis. Mol Biol Cell 15: 3509-3519.
13. Edwards DC, Sanders LC, Bokoch GM, Gill GN (1999) Activation of LIM-kinase by Pak1 couples Rac/Cdc42 GTPase signalling to actin cytoskeletal dynamics. Nat Cell Biol 1: 253-259.
14. Patterson GH, Lippincott-Schwartz J (2002) A photoactivatable GFP for selective photolabeling of proteins and cells. Science 297: 1873-1877.
15. Schmidt K, Nichols BJ (2004) A barrier to lateral diffusion in the cleavage furrow of dividing mammalian cells. Curr Biol 14: 1002-1006.
16. Weisswange I, Bretschneider T, Anderson KI (2005) The leading edge is a lipid diffusion barrier. J Cell Sci 118: 4375-4380.
17. Simons K, Toomre D (2000) Lipid rafts and signal transduction. Nat Rev Mol Cell Biol 1: 31-39.

Chapter 6 Conclusions

6.1 Summary of research findings

The CXCL12/CXCR4 signaling axis is instrumental to the metastasis of many cancers, yet preclinical studies suggest that blocking the pathway alone is not sufficient to inhibit its malignant effects [1]. As cancer arises from a complex network of interdependent biological events, eliminating cancer cannot be understood by studying only one gene or protein at a time. In this thesis, we took three approaches to examine complexity in the CXCL12/CXCR4/CXCR7 signaling axis. In Chapters 2 and 4, we used a bioinformatics approach to study CXCL12 isoforms and to understand CXCR7 in the context of CXCR4 signaling. In Chapter 3, we built a model integrating multiple biological scales to understand how molecular level behavior influences migration in the tissue scale. In Chapter 4, we developed a mechanistic model to understand how competition within the signaling pathway affects strategies targeting these receptors. Here, we summarize key conclusions from the thesis and discuss future directions of this work.

6.1.1 CXCL12 isoforms matter in breast cancer

In Chapter 2, we performed the first study to investigate the role of all six CXCL12 isoforms in breast cancer. The Cancer Genome Atlas (TCGA) is a data platform providing free access to genomic data collected by the National Cancer Institute (cancergenome.nih.gov). Currently, all TCGA breast cancer data is available without limitations and is the only publicly available clinical database using RNAseq. This allowed us to differentiate between CXCL12 isoforms and correlate isoform expression to important clinical and survival metrics. While CXCL12-ε and -ϕ expression levels are undistinguishable from noise, four of the six isoforms; CXCL12-α, -β, -γ and -δ, are expressed at detectable levels in primary breast tumors. Lower levels of these isoforms correlate with cancer (as compared to normal tissue), higher tumor stage, and worse survival outcomes [2].

While the bioinformatics analysis (Chapter 2) demonstrated clinical relevance of CXCL12 isoforms, the multi-scale model (Chapter 3) used a mechanistic approach to understand how isoforms can result in different migration outcomes. Previous studies have shown that CXCL12-γ is more effective than the α and β isoforms at promoting CXCR4+ chemotaxis, yet, due to experimental limitations, could only hypothesize that gradient differences among isoforms could explain this phenomena [3-6]. In our model, we showed that the characteristics of high affinity to CXCR4 and to the surface upon which cells are migrating make CXCL12-γ the most potent at promoting CXCR4+ migration. Our multi-scale model incorporated ligand diffusion, degradation, receptor-mediated internalization, and surface binding to calculate gradient shape over position and time. Unlike experiments, the model was able to switch on and off individual molecular events. This allowed us to demonstrate that high affinity to surfaces results in steeper gradients and that high affinity to CXCR4 allows better directed movement of CXCR4+ cells. In addition to interpreting CXCR4+ migration in the *in vitro* microfluidic source-sink device, the model predicted that gradients will form in the disorganized cell structures representative of primary breast tumors, and that CXCL12 isoforms can also differentially regulate migration in those structures. While experimental models have focused on CXCL12 gradient formation due to the positioning of a bulk mass of CXCR7+ cells near CXCL12-secreting and CXCR4+ cells [4,7-9], our model was able to show gradient formation and consequent cell migration when cell patterns are more random in nature. In particular, we predict that CXCL12-γ is still more effective at driving CXCR4+ migration in tumor-like cell formations than CXCL12-α and –β [10].

6.1.2 Low levels of CXCL12 can result in worse cancer outcomes

A surprising result in the CXCL12 isoform bioinformatics analysis (Chapter 2) is that lower levels of CXCL12 confer worse prognosis than higher levels of CXCL12. Considering that CXCL12 was first identified as a potential malignant marker due to its expression in carcinoma-associated fibroblasts [11], we initially anticipated the opposite trend. A broad analysis of CXCL12 expression in Oncomine, a cancer microarray database that allows facile search of publicly available clinical data [12], reveals that the

majority of other publicly available breast cancer datasets correlate with lower levels of CXCL12 (Figure 6.1) [12].

The multi-scale model (Chapter 3) offers one explanation as to why higher levels of CXCL12 might correlate with better patient outcomes. The model demonstrates that high levels of CXCL12 promote significant receptor desensitization, resulting in reduced migration. In addition, at high CXCL12 levels, internalization by CXCR4 and CXCR7 are insufficient to produce steep gradients that direct migration [10]. Other studies propose ways by which low levels of CXCL12 may confer worse patient outcomes. Pre-treating CXCR4+ cells with a low concentration of CXCL12 prior to stimulation with a higher CXCL12 concentration suggests that low levels of CXCL12 pre-sensitize CXCR4+ cells to further activation [13]. Another study demonstrated that low plasma CXCL12 correlates with distant metastasis in breast cancer, proposing that low CXCL12 in the blood do not desensitize CXCR4 on circulating tumor cells and allow for extravasation to the metastatic site [14,15].

6.1.3 Targeting undesired CXCR4 activity in cancer

Blocking the CXCR4 receptor has not been a clinically successful strategy to inhibit cancer progression [1]. Our multi-scale model highlighted simultaneous targeting of CXCR4 and CXCR7 as a strategy to halt CXCL12/CXCR4-mediated cancer progression. As CXCR7 is a high affinity receptor for both CXCL12 and β-arrestin, it controls both gradient scope and magnitude. Gradients of CXCL12-γ are particularly difficult to target, as its high affinity for glycosaminoglycans promotes steep gradients. Yet we find that simultaneous blocking of CXCR4 and CXCR7 activity results in a greater reduction of migration than the sum of blocking each receptor individually. This synergistic effect suggests targeting CXCR7 together with CXCR4 can boost efficacy without resorting to toxic levels of a CXCR4 inhibitor. Others have proposed co-targeting of CXCR7 with CXCR4 as a potential method to block undesired CXCR4 signaling [16].

An alternative targeting strategy is to develop a biased therapeutic that can preserve beneficial CXCR4 function while inhibiting signaling pathways that result in pathological effects [17-20]. Biased therapeutics designed to correct the pathological signaling

pathway, rather than a complete inhibition of the receptor response, could provide improved therapy while mitigating toxicity. Also called permissive antagonists, these biased ligands may allow some agonist signaling. For example, while the CXCR7 antagonist AMD3100 competes with CXCL12 at the ligand binding site (thus affecting all pathways downstream of CXCR4), ATI-2341 is a pepducin that favors Gαi activation over Gα13 and does not result in β-arrestin recruitment [19]. Identifying which parts of the signaling network to target will allow us to more precisely treat disease.

In Chapter 4, we constructed a model to examine potential unintended consequences of inhibiting CXCR7 due to the fact that CXCR4/CXCR7 share many signaling components. CXCR7 is best known for its ability to scavenge extracellular CXCL12 and for being a seven-transmembrane receptor without G-protein activity [21-24]. Often overlooked is that CXCR7 can be co-expressed with CXCR4 on populations of tumor cells [25], which may have important implications when targeting the CXCL12/CXCR4 pathway. Our mechanistic model of CXCR4/CXCR7 receptor dynamics and signaling shows that CXCR7 scavenges both CXCL12 and β-arrestin from CXCR4. Therefore, instead of increasing G-protein signaling, CXCR7 decreases G-protein signaling while simultaneously decreasing the availability of β-arrestin. The model also identified other potential targets that can shift the direction of G-protein mediated ERK signaling. We find that depending on the rates of CXCR4 recycling and the relative rate of receptor phosphorylation compared to ligand binding, increasing β-arrestin can have a positive, negative, or no impact on G-protein signaling. This suggests that altering recycling rates (potentially by targeting endosomes) or targeting G-protein receptor kinases may also be effective strategies to alter CXCR4 signaling.

After screening 30,000 candidates, Castaldo et al. identified 41 compounds that can bind to CXCR4 [17]. These compounds belong to one of the five following classes: functional antagonists, G protein dependent antagonists, full antagonists, antagonists for both G protein and β-arrestin, and antagonists that affect internalization. As we gain more knowledge about which downstream pathways are responsible for specific cell behavior,

employing thorough screening strategies could identify currently available drugs that block specific pathways.

6.2 Limitations and future directions

6.2.1 Monomers and dimers of CXCL12, CXCR4, and CXCR7

The role of CXCL12 in cancer cell migration is made even more complicated because it can signal in its monomer or dimer form [26-28]. The two forms exist in equilibrium [27,28] and monomers and dimers signal via different pathways [28-30]. Which pathways are promoted by monomers or dimers is still unclear. Using preferentially monomeric or constitutively dimeric CXCL12 produced from bacterial cultures, Drury et al. showed that the monomeric form primarily signals via β-arrestins and leads to persistant activation of pERK and chemotaxis, whereas the dimer form signals through G proteins and does not lead to chemotaxis. These conclusions were supported with transwell migration assays using human colorectal carcinoma cells (HCT116) as well as ERK time course studies [29]. Ray et al. isolated CXCL12 monomers and dimers secreted from human embryonic kidney (HEK)-295T cells using column chromatography and employed bioluminescence complementation techniques to verify the roles of monomers and dimers. They reported the opposite: CXCL12 monomers seemed to signal through G proteins more than dimers, whereas dimers resulted in higher association with β-arrestins and chemotaxis [30]. These data suggest that monomeric and dimeric CXCL12 are biased agonists. Whether or not monomeric and dimeric CXCL12 are indeed biased agonists, and how each CXCL12 isoform may differ in favoring monomer or dimer form, have additional implications on how the CXCL12/CXCR4 pathway can be targeted. These biological effects were not taken into account in our computational model. The present level of detail in the model focused on ligand binding and internalization and was sufficient for our model show how receptor-bearing cells and CXCL12 isoforms affect gradient shape. In our ordinary differential equation models representing ligand-receptor dynamics, we assumed that CXCL12 and CXCR4 interact with a stoichiometric ratio of 1:1, which is supported by functional and computational experiments[31]. Our ODE submodel was constructed and validated on quantitative binding and internalization experimental data using many CXCL12 concentrations and

over multiple time points in the same cell types used in the source-sink device experiments [32].

CXCR4 and CXCR7 can also exist in dimer form – as homodimers, or as heterodimers with each other. Heterodimerization is not only limited to CXCR4 and CXCR7. CXCR4 can dimerize with CCR2, CCR5 and CXCR3 [33].

It is still unclear whether dimerization shifts signaling to one pathway versus another, or if it can elicit activation of pathways that either receptor cannot activate on its own [34-37]. Modeling may be able to help uncouple these effects (Figure 6.2). By building a model that provides accurate predictions of CXCR4 signaling in cells lacking CXCR7, and vice versa, the model may be able to predict what behavior is expected if dimerization simply favors one pathway over another, or if signaling is distinctly due to a unique property of a heterodimer.

6.2.2 Bioinformatics limitations

Although patient tumor databases provide a wealth of information and a link to clinical relevance, one major limitation is that gene expression analysis profiles *all* cells in the tumor environment without regard for the type of cell. Considering that the tumor microenvironment plays a strong role in cancer progression, it would be advantageous to identify which cells (ie. fibroblasts, cancer cells, and others) express which receptors, and if some receptors are expressed together or individually. One high throughput method to separate cell types is serial analysis of gene expression (SAGE). This method separates cell types by first mincing and digesting tissue, and then subjecting the digested tissue through sequential filtration or single cell suspension with specific antigens to identify cell types such as leukocytes, myofibroblasts, endothelial, epithelial, and myoepithelial cells [38].

6.2.3 Gradient directionality

We have established that CXCR4 cells can move in the disorganized structures like the tumor environment, and that movement is affected by ligand type and presence of CXCR7. However, the model does not incorporate directionality. Why do CXCL12

gradients matter in the primary tumor environment? This question is left unanswered in current literature. One hypothesis is that CXCL12-expressing stroma residing on the tumor edge may promote local invasion of cancer cells [39]. Alternatively, CXCL12 may serve to keep CXCR4+ cancer cells in protective niches within the primary tumor [40]. It has also been demonstrated in mouse models that CXCL12 gradients promote angiogenesis by recruiting endothelial progenitor cells to the primary tumor site [11]. By incorporating a more realistic tumor environment (ie. vascular sources, a boundary between normal and malignant tissue), these hypotheses may be addressed in a future version of the multi-scale agent based model.

6.3 Figures

Analysis Type by Cancer	Cancer vs. Normal	
Bladder Cancer		3
Brain and CNS Cancer		1
Breast Cancer	1	14
Cervical Cancer		1
Colorectal Cancer		7
Esophageal Cancer	1	
Gastric Cancer		3
Head and Neck Cancer		1
Kidney Cancer		4
Leukemia	1	3
Liver Cancer	1	4
Lung Cancer		3
Lymphoma	9	
Melanoma		
Myeloma		1
Other Cancer		
Ovarian Cancer		1
Pancreatic Cancer		2
Prostate Cancer		
Sarcoma	1	
Significant Unique Analyses	14	48
Total Unique Analyses	477	

Figure 6.1 Lower CXCL12 gene expression correlates with many types of cancers

We used Oncomine [12] to look at the number of cancer datasets that show a correlation between low gene expression of CXCL12 and cancer tissue. The first column shows cancer types with available data in Oncomine. The numbers in the colored boxes represent the number of clinical data sets per cancer type that have a correlation between high CXCL12 and cancer (red) or low CXCL12 and cancer (blue). Note that for breast cancer, 14 out of 15 datasets have lower CXCL12 gene expression in cancer samples than in the normal samples of the dataset. The threshold settings in Oncomine were set to the following: p-value $<10^{-4}$; fold change >2; and gene rank in top 10%.

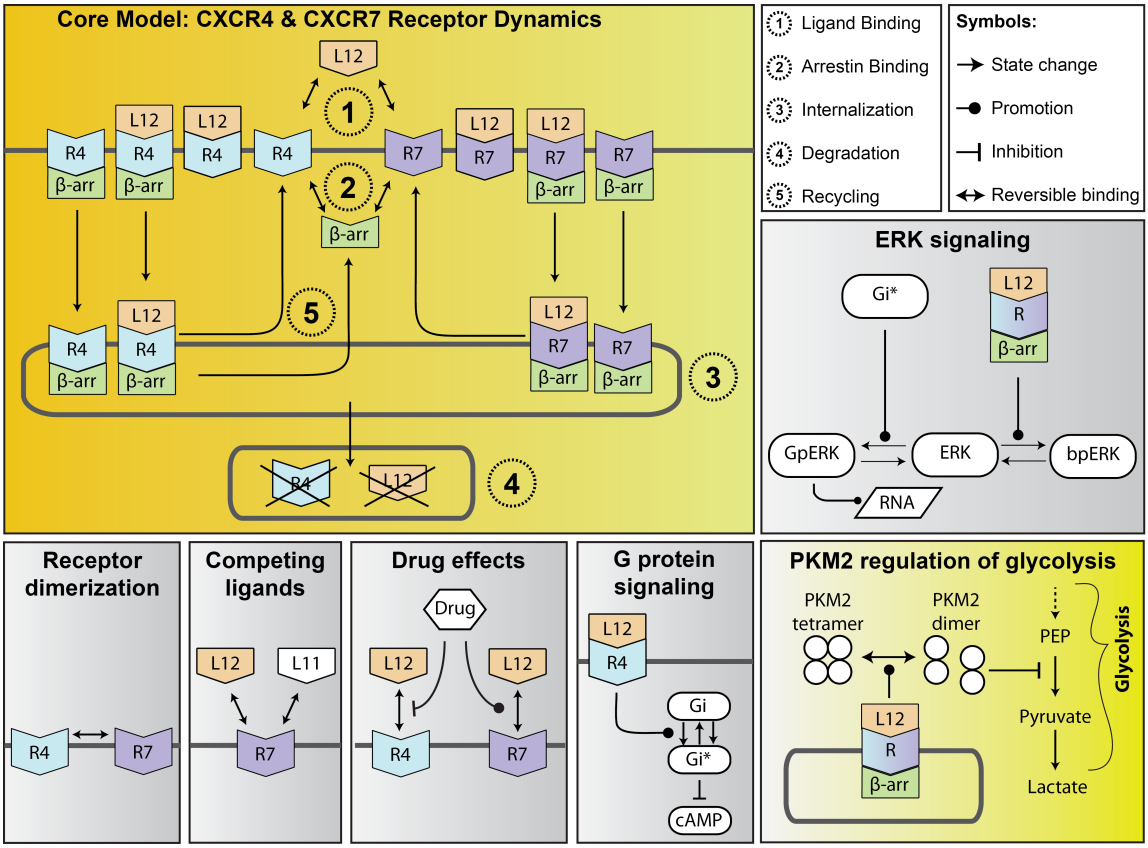

Figure 6.2 Future directions in models of CXCR4/CXCR7 signaling

Both CXCR4 and CXCR7 are implicated in cancer and they may interact with one another at many points in their signaling pathways. The two receptors not only form homodimers, but can also bind to one another, forming heterodimers. Models may be able to determine if differences in signaling in cells displaying heterodimers is due to an additive effect of both CXCL12/CXCR4 and CXCL12/CXCR7 pathways working simultaneously, or if the behavior arises from properties unique to the heterodimer structure. While CXCL12 has a monogamous relationship with CXCR4, CXCR7 may also bind CXCL11, and investigating how the presence of CXCL11 would further affect their shared signaling is of potential interest. Integrating more detailed models of G-protein, metabolic, and ERK signaling may serve to link the model to more experimental outputs and better model validation, as well as suggest other drug targets.

6.4 References

1. Duda DG, Kozin SV, Kirkpatrick ND, Xu L, Fukumura D, et al. (2011) CXCL12 (SDF1alpha)-CXCR4/CXCR7 pathway inhibition: an emerging sensitizer for anticancer therapies? Clin Cancer Res 17: 2074-2080.
2. Zhao S, Chang SL, Linderman JJ, Feng FY, Luker GD (2014) A Comprehensive Analysis of CXCL12 Isoforms in Breast Cancer. Transl Oncol.
3. Altenburg JD, Broxmeyer HE, Jin Q, Cooper S, Basu S, et al. (2007) A naturally occurring splice variant of CXCL12/stromal cell-derived factor 1 is a potent human immunodeficiency virus type 1 inhibitor with weak chemotaxis and cell survival activities. J Virol 81: 8140-8148.
4. Cavnar SP, Ray P, Moudgil P, Chang SL, Luker KE, et al. (2014) Microfluidic source-sink model reveals effects of biophysically distinct CXCL12 isoforms in breast cancer chemotaxis. Integr Biol (Camb).
5. Ray P, Stacer AC, Fenner J, Cavnar SP, Meguiar K, et al. (2014) CXCL12-gamma in primary tumors drives breast cancer metastasis. Oncogene 0.
6. Rueda P, Balabanian K, Lagane B, Staropoli I, Chow K, et al. (2008) The CXCL12gamma chemokine displays unprecedented structural and functional properties that make it a paradigm of chemoattractant proteins. PLoS One 3: e2543.
7. Venkiteswaran G, Lewellis SW, Wang J, Reynolds E, Nicholson C, et al. (2013) Generation and dynamics of an endogenous, self-generated signaling gradient across a migrating tissue. Cell 155: 674-687.
8. Dalle Nogare D, Somers K, Rao S, Matsuda M, Reichman-Fried M, et al. (2014) Leading and trailing cells cooperate in collective migration of the zebrafish posterior lateral line primordium. Development 141: 3188-3196.
9. Torisawa YS, Mosadegh B, Bersano-Begey T, Steele JM, Luker KE, et al. (2010) Microfluidic platform for chemotaxis in gradients formed by CXCL12 source-sink cells. Integr Biol (Camb) 2: 680-686.
10. Chang SL, Cavnar SP, Takayama S, Luker GD, Linderman J (2015) Cell, isoform, and environment factors shape gradients and modulate chemotaxis. PLoS One In Press.
11. Orimo A, Gupta PB, Sgroi DC, Arenzana-Seisdedos F, Delaunay T, et al. (2005) Stromal fibroblasts present in invasive human breast carcinomas promote tumor growth and angiogenesis through elevated SDF-1/CXCL12 secretion. Cell 121: 335-348.
12. Rhodes DR, Yu J, Shanker K, Deshpande N, Varambally R, et al. (2004) ONCOMINE: a cancer microarray database and integrated data-mining platform. Neoplasia 6: 1-6.
13. Luker KE, Gupta M, Luker GD (2008) Imaging CXCR4 signaling with firefly luciferase complementation. Anal Chem 80: 5565-5573.
14. Hassan S, Baccarelli A, Salvucci O, Basik M (2008) Plasma stromal cell-derived factor-1: host derived marker predictive of distant metastasis in breast cancer. Clin Cancer Res 14: 446-454.
15. Hassan S, Ferrario C, Saragovi U, Quenneville L, Gaboury L, et al. (2009) The influence of tumor-host interactions in the stromal cell-derived factor-1/CXCR4 ligand/receptor axis in determining metastatic risk in breast cancer. Am J Pathol 175: 66-73.
16. Liles WC, Broxmeyer HE, Rodger E, Wood B, Hubel K, et al. (2003) Mobilization of hematopoietic progenitor cells in healthy volunteers by AMD3100, a CXCR4 antagonist. Blood 102: 2728-2730.
17. Castaldo C, Benicchi T, Otrocka M, Mori E, Pilli E, et al. (2014) CXCR4 Antagonists: A Screening Strategy for Identification of Functionally Selective Ligands. J Biomol Screen 19: 859-869.
18. Kenakin T (2005) New concepts in drug discovery: collateral efficacy and permissive antagonism. Nat Rev Drug Discov 4: 919-927.
19. Quoyer J, Janz JM, Luo J, Ren Y, Armando S, et al. (2013) Pepducin targeting the C-X-C chemokine receptor type 4 acts as a biased agonist favoring activation of the inhibitory G protein. Proc Natl Acad Sci U S A 110: E5088-5097.
20. Zweemer AJ, Toraskar J, Heitman LH, Ijzerman AP (2014) Bias in chemokine receptor signalling. Trends Immunol.
21. Miao Z, Luker KE, Summers BC, Berahovich R, Bhojani MS, et al. (2007) CXCR7 (RDC1) promotes breast and lung tumor growth in vivo and is expressed on tumor-associated vasculature. Proc Natl Acad Sci U S A 104: 15735-15740.

22. Rajagopal S, Kim J, Ahn S, Craig S, Lam CM, et al. (2010) Beta-arrestin- but not G protein-mediated signaling by the "decoy" receptor CXCR7. Proc Natl Acad Sci U S A 107: 628-632.
23. Naumann U, Cameroni E, Pruenster M, Mahabaleshwar H, Raz E, et al. (2010) CXCR7 functions as a scavenger for CXCL12 and CXCL11. PLoS One 5: e9175.
24. Luker KE, Steele JM, Mihalko LA, Ray P, Luker GD (2010) Constitutive and chemokine-dependent internalization and recycling of CXCR7 in breast cancer cells to degrade chemokine ligands. Oncogene 29: 4599-4610.
25. Luker KE, Lewin SA, Mihalko LA, Schmidt BT, Winkler JS, et al. (2012) Scavenging of CXCL12 by CXCR7 promotes tumor growth and metastasis of CXCR4-positive breast cancer cells. Oncogene 31: 4750-4758.
26. Fermas S, Gonnet F, Sutton A, Charnaux N, Mulloy B, et al. (2008) Sulfated oligosaccharides (heparin and fucoidan) binding and dimerization of stromal cell-derived factor-1 (SDF-1/CXCL 12) are coupled as evidenced by affinity CE-MS analysis. Glycobiology 18: 1054-1064.
27. Holmes WD, Consler TG, Dallas WS, Rocque WJ, Willard DH (2001) Solution studies of recombinant human stromal-cell-derived factor-1. Protein Expr Purif 21: 367-377.
28. Veldkamp CT, Peterson FC, Pelzek AJ, Volkman BF (2005) The monomer-dimer equilibrium of stromal cell-derived factor-1 (CXCL 12) is altered by pH, phosphate, sulfate, and heparin. Protein Sci 14: 1071-1081.
29. Drury LJ, Ziarek JJ, Gravel S, Veldkamp CT, Takekoshi T, et al. (2011) Monomeric and dimeric CXCL12 inhibit metastasis through distinct CXCR4 interactions and signaling pathways. Proc Natl Acad Sci U S A 108: 17655-17660.
30. Ray P, Lewin SA, Mihalko LA, Lesher-Perez SC, Takayama S, et al. (2012) Secreted CXCL12 (SDF-1) forms dimers under physiological conditions. Biochem J 442: 433-442.
31. Kufareva I, Stephens BS, Holden LG, Qin L, Zhao C, et al. (2014) Stoichiometry and geometry of the CXC chemokine receptor 4 complex with CXC ligand 12: molecular modeling and experimental validation. Proc Natl Acad Sci U S A 111: E5363-5372.
32. Coggins NL, Trakimas D, Chang SL, Ehrlich A, Ray P, et al. (2014) CXCR7 Controls Competition for Recruitment of beta-Arrestin 2 in Cells Expressing Both CXCR4 and CXCR7. PLoS One 9: e98328.
33. Watts AO, van Lipzig MM, Jaeger WC, Seeber RM, van Zwam M, et al. (2013) Identification and profiling of CXCR3-CXCR4 chemokine receptor heteromer complexes. Br J Pharmacol 168: 1662-1674.
34. Decaillot FM, Kazmi MA, Lin Y, Ray-Saha S, Sakmar TP, et al. (2011) CXCR7/CXCR4 heterodimer constitutively recruits beta-arrestin to enhance cell migration. J Biol Chem 286: 32188-32197.
35. Levoye A, Balabanian K, Baleux F, Bachelerie F, Lagane B (2009) CXCR7 heterodimerizes with CXCR4 and regulates CXCL12-mediated G protein signaling. Blood 113: 6085-6093.
36. Luker KE, Gupta M, Luker GD (2009) Imaging chemokine receptor dimerization with firefly luciferase complementation. FASEB J 23: 823-834.
37. Zabel BA, Wang Y, Lewen S, Berahovich RD, Penfold ME, et al. (2009) Elucidation of CXCR7-mediated signaling events and inhibition of CXCR4-mediated tumor cell transendothelial migration by CXCR7 ligands. J Immunol 183: 3204-3211.
38. Allinen M, Beroukhim R, Cai L, Brennan C, Lahti-Domenici J, et al. (2004) Molecular characterization of the tumor microenvironment in breast cancer. Cancer Cell 6: 17-32.
39. Roussos ET, Condeelis JS, Patsialou A (2011) Chemotaxis in cancer. Nat Rev Cancer 11: 573-587.
40. Burger JA, Kipps TJ (2006) CXCR4: a key receptor in the crosstalk between tumor cells and their microenvironment. Blood 107: 1761-1767.

Appendix A Supporting information for Cell, isoform, and environment factors shape gradients and modulate chemotaxis

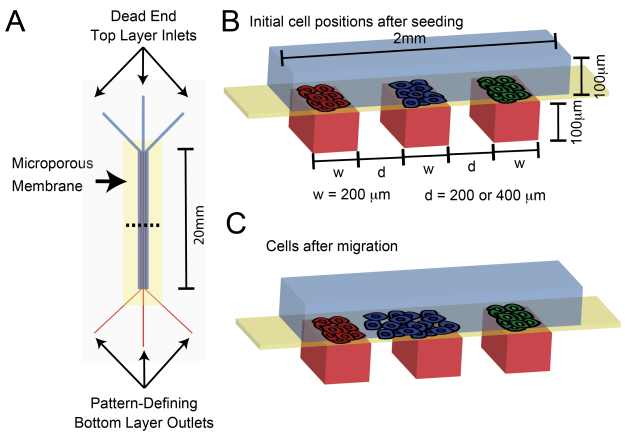

Figure A.1 Microfluidic source-sink device

(A) Bird's eye view of *in vitro* microfluidic source-sink device. Cells are patterned into stripes of 200 μm width by use of inlet and outlet ports as described in [1,2]. (B) View of CXCL12+ (red), CXCR4+ (blue), and CXCR7+ (green) cells in device after initial seeding. The spacing between the cell stripes can be 200 μm (used for fitting experiments) or 400 μm (used for validation experiments). (C) Over time, CXCR4+ cells move in the direction of the CXCL12+ cells.

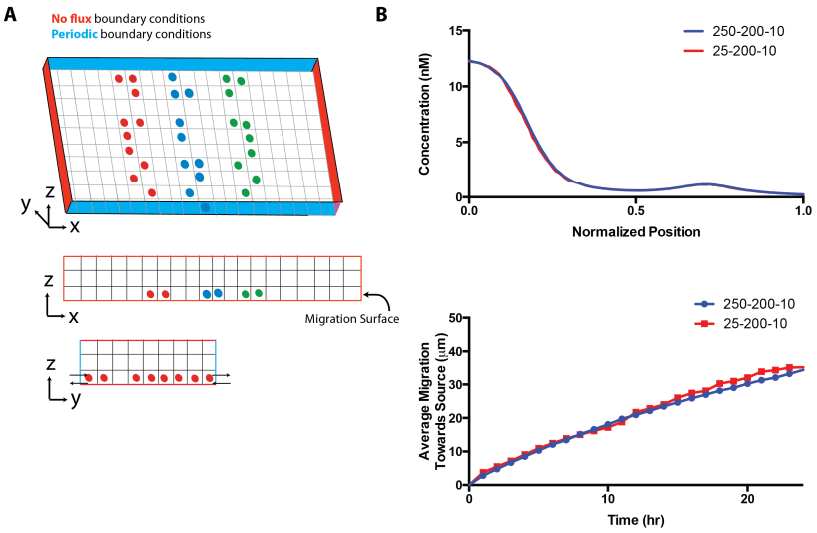

Figure A.2 Boundary conditions and validation for source-sink device setup

(A) Boundary conditions for agent movement and chemokine diffusion when modeling the source-sink device. (B) Reducing the grid to 25x200x10 gridspaces gives the same gradient calculations and average migration as a grid 10 times as large. Average is representative of 30 simulations.

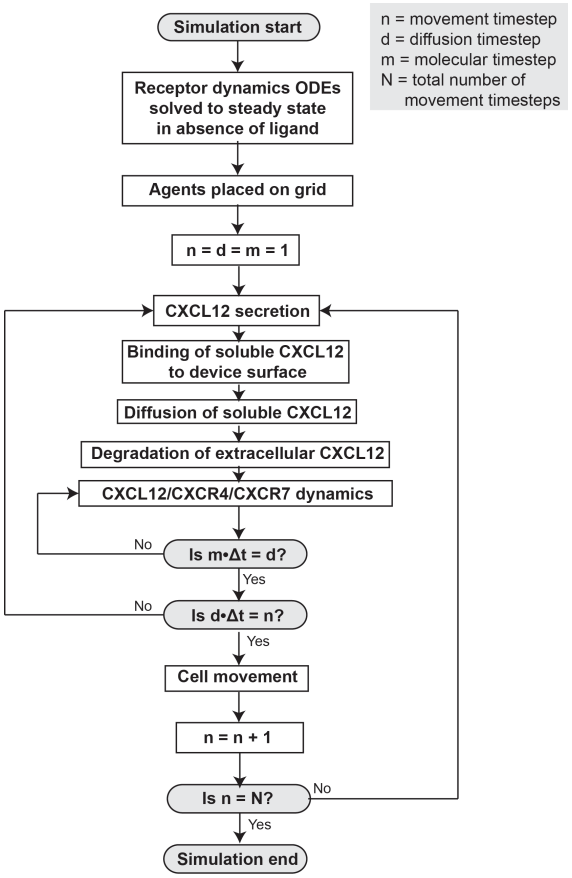

Figure A.3 Model workflow

We assume that receptors and β-arrestin within cells initially seeded in the device are at steady state. Prior to populating the agent based model with cells, we calculate the steady state values of free, surface, and internalized receptors and bound and free β-arrestin. In order to calculate multiple simultaneous events while minimizing computational requirements, we use operator splitting to decouple the equations and then employ the appropriate time step. Receptor-ligand dynamics occur on the smallest time scale and are solved using the molecular time step. Diffusion, extracellular degradation and extracellular binding events are solved using the diffusion time step. Cell behavior is calculated on a larger movement time step.

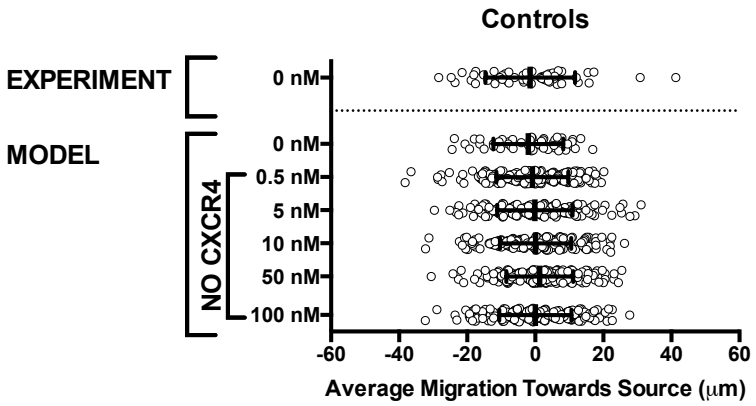

Figure A.4 Validation of movement time step

Experimental data reproduced from [1] (Figure 1, E-G at 0% secretion). Each data point (n=54) represents the average position of CXCR4 cells per view field of the device at 24 hours.

CXCR4+ cells in the absence of CXCL12 and cells that do not bear CXCR4 should move randomly (average migration = 0 μm) with a standard deviation that matches random movement within the experimental source-sink device. The model uses the same parameters as in Supporting Table 1, but with (1) an imposed linear CXCL12 gradient with a concentration on the left of the device as indicated in the y-axis, and a concentration of 0 nM on the right of the device and (2) CXCL12+ source cells and CXCR7+ sink cells replaced with cells that did not express the ligand and protein. For the simulation that lacks CXCL12, total number of CXCR4 on CXCR4+ cells is as listed in Supporting Table 1. For all other simulations, total CXCR4 was set to 0. Each data point (n=200) represents the average migration for one device simulation.

In absence of CXCL12 or CXCR4, CXCR4 cells have average migration of 0. Standard deviation is same as experimental.

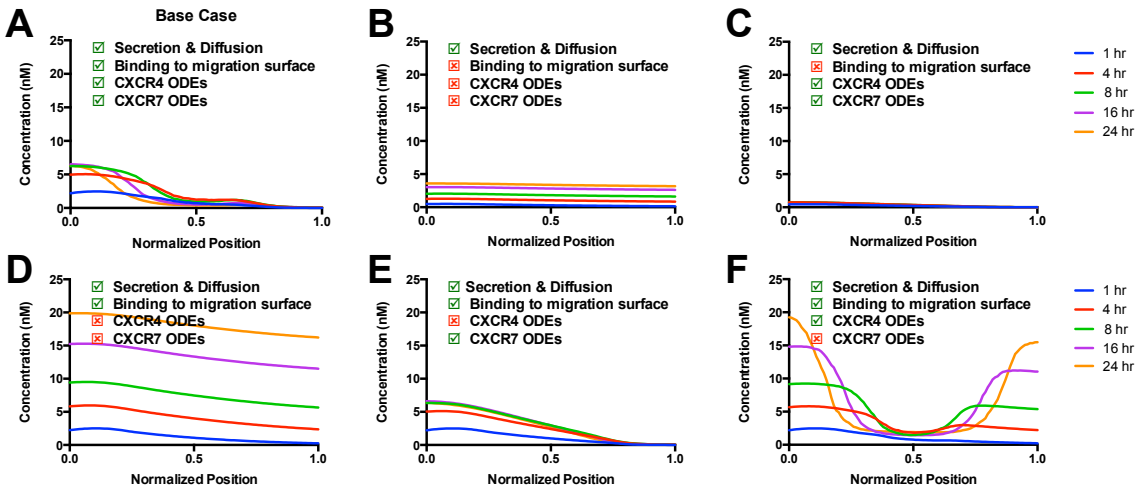

Figure A.5 Contribution of gradient-shaping events

To understand the contribution of cellular and environmental effects on gradient shape over time and position, we systematically "turned off" events from the model. All parameters are as listed in Supporting Table 1. To turn off binding to the migration surface, we set the number of binding sites to 0. To turn off receptor ODEs, we inhibited the call of the ODE functions. Note that secretion and diffusion alone result in relatively shallow, linear gradients that increase in concentration over time. Removing binding to the migration surface limits total CXCL12 concentration. Removing CXCL12-CXCR4 ODEs results in an increase in the gradient in the location of the CXCR4+ cells. Removing CXCL12-CXCR7 ODEs results in an overall increase in CXCL12 concentration across the grid, as well as a significant increase in concentration in the region of the CXCR7+ cells.

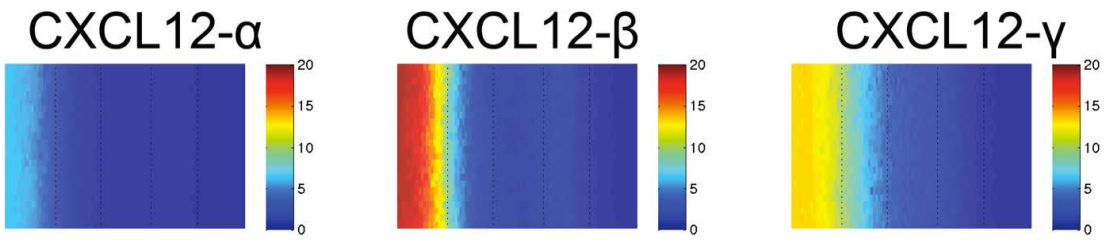

Figure A.6 Comparison of gradients within device between CXCL12-α, -β, and -γ

Gradients using parameters in Table 1 and Supporting Table 1. Colorbars indicate total CXCL12 concentration in nM. CXCL12-β has highest overall concentration and steepest gradients compared to CXCL12-α and -γ.

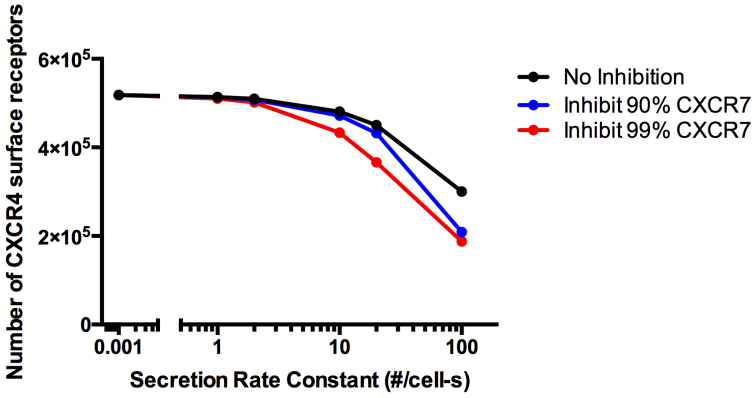

Figure A.7 Effect of CXCR7 on CXCR4 surface receptors

The average number of CXCR4 surface receptors per CXCR4+ cell across a range of CXCL12 secretion rate constants under conditions of no inhibition (all parameters same as listed in Supporting Table A), inhibition of 90% of CXCR7 receptors, and inhibition of 99% of CXCR7 receptors. Reducing the number of CXCR7 receptors results in a decrease of CXCR4 surface receptors at higher CXCL12 secretion rates, but does not affect CXCR4 surface receptor expression at lower secretion rates. Model data are expressed as mean of 30 replications +/- standard deviation. The maximum standard deviation is ~1000 receptors, thus, error bars are not visible on the plot.

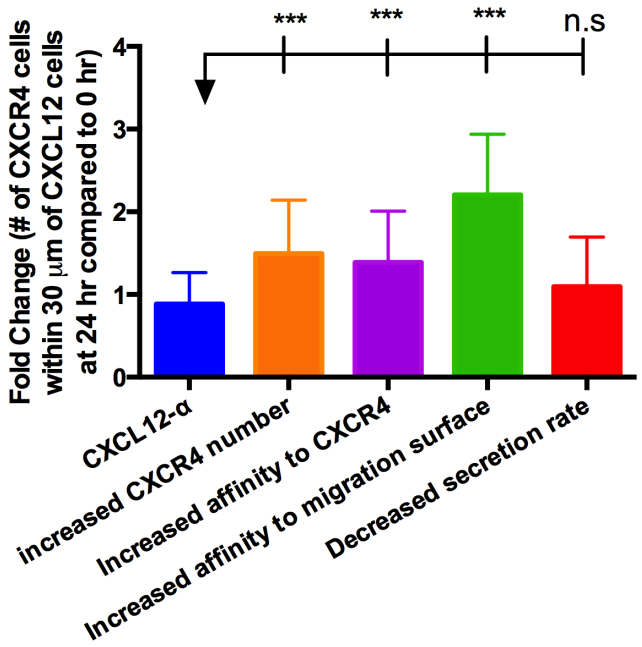

Figure A.8 CXCR4+ movement in gradients of CXCL12-α tumor simulations with adjusted parameters

To determine whether CXCL12-α-like parameters can result in CXCR4+ migration in tumor simulations, we increased total CXCR4 from $5x10^3$ to $5x10^4$ receptors/cell, which significantly enhanced CXCR4+ migration. To examine which ligand-related parameters have the largest effect on CXCR4+ migration in tumor simulations, we systemically swapped CXCL12-α parameter values with CXCL12-γ parameter values (increased affinity to CXCR4: $K_{D,R4,L12}$ = 10 nM; increased affinity to migration surface: $K_{D,L,S}$ = 5nM; decreased secretion rate constant: *CXCL12sec* = 5 molecules/cell-s). Both the increase in affinity to the migration surface and to CXCR4 significantly enhance migration. All other parameters and initial conditions were the same as those used in Figure H-J. *** $P < 0.0005$.

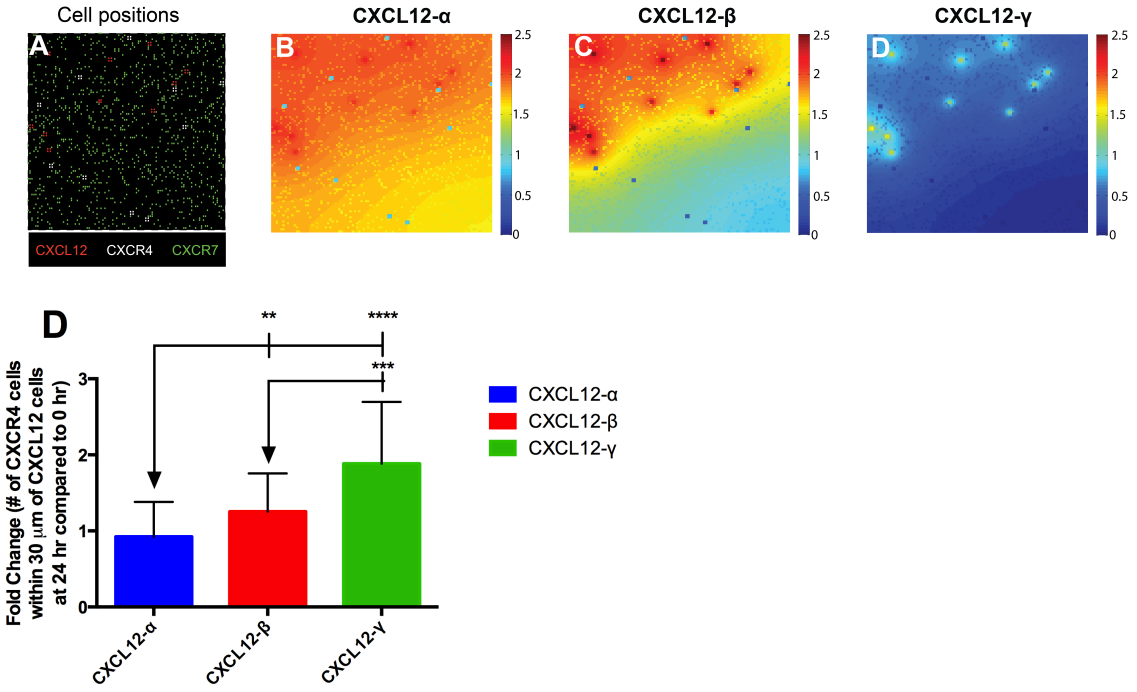

Figure A.9 Tumor simulations using an extended grid

Simulations with the same parameters and initial conditions as Figure 5H-J ($5x10^3$ total receptors/cell for both CXCR4+ and CXCR7+ cells), but with an extended grid of 100x100x5. (A) Cell positions. Gradients of (B) CXCL12-α, (C) CXCL12-β, (D) CXCL12-γ on the migration surface at 24 hours. Colorbars indicate the total CXCL12 concentration in nM. Similarly to the 2D grid, gradients of CXCL12-γ are characterized by steeper gradients and shorter maintained distances than those of CXCL12-α. (D) Consistent with the results in the 2D grid, CXCR4+ cells move significantly more towards CXCL12+ cells in gradients of CXCL12-γ than CXCL12-β or CXCL12-α. * $P < 0.05$; ** $P < 0.005$; *** $P < 0.0005$.

Table A.1: Model parameters

Table A.1a Multi-scale model parameters

Parameter	Description	Value	Literature Range	Reference
Cell density (cells/mm^2)	Density of cells patterned in microfluidic device	2500 (125 cells of each type)		[1]
CXCL12sec (molecules/cell-s)	Secretion rate of CXCL12+ cells (Also shown in Table 1)	20[*]	15-25	[1]
D_{CXCL12} (cm^2/s)	CXCL12 diffusivity coefficient	$1.5x10^{-6}$	$1.5x10^{-6}$ – $1.7x10^{-6}$	[2,3]
k_{deg} (s^{-1})	Extracellular CXCL12 degradation rate	$2x10^{-5}$	$6x10^{-5}$ – $4x10^{-3}$	[4-6]
Total number of surface sites (S+ $L \cdot S$) (#/gridspace)	Number of surface bound sites per gridspace	$5x10^5$	$2.3x10^5$-$1.2x10^6$ [#]	[7,8]
$K_{D,L,S}$ (nM)	Dissociation constant of CXCL12-α to surface site	100[*]	93	[9]
$k_{f,L,S}$ (s^{-1})	Forward rate constant of ligand to surface site	0.001[^]	0.001	[9]
Total CXCR4 (molecules/cell)	Total number of CXCR4 receptors per CXCR4+ cell	$7.1x10^5$		This work
Total CXCR7 (molecules/cell)	Total number of CXCR7 receptors per CXCR7+ cell	$2x10^6$		This work
Total β-arrestin in CXCR4+ cells (molecules/cell)	Total number of β-arrestin per CXCR4+ cell	$5x10^5$		[10]
Total β-arrestin in CXCR7+ cells (molecules/cell)	Total number of β-arrestin per CXCR7+ cell	$7x10^{5}$[&]		[10]

[*] Fit to experimental data, as shown in Figure 3

[#] Used number of cell surface heparan sulfate sites as a starting point. Sensitivity analysis (using LHS and PRCC as described in Methods) showed no dependence of average CXCR4+ at 24 hr on number of surface sites within this range.

[^] Assumed the forward rate constant for ligand binding to a surface site is the same as that for binding to heparan sulfate.

[&] Increased to reflect that the majority of cell surface receptors on CXCR7+ cells are intracellular.

Table A.1b Molecular species involved in ligand-binding and internalization dynamics of CXCR4 and CXCR7

CXCR4 Species	Description	CXCR7 Species	Description
R_4 (#/cell)	Free cell-surface CXCR4	R_7 (#/cell)	Free cell-surface CXCR7
L_{12} (nM)	Free extracellular CXCL12	L_{12} (nM)	Free extracellular CXCL12
B_e (#/cell)	Free endogenous β-arrestin 2	B_e (#/cell)	Free endogenous β-arrestin 2
R_{4Be} (#/cell)	R_4 bound to B_e	R_{7Be} (#/cell)	R_7 bound to B_e
C_4 (#/cell)	R_4 bound to L_{12}	C_7 (#/cell)	R_7 bound to L_{12}
C_{4Be} (#/cell)	R_{4Be} bound to L_{12}	C_{7Be} (#/cell)	R_{7Be} bound to L_{12}
R_{4Bei} (#/cell)	Intracellular R_{4Be}	R_{7Bei} (#/cell)	Intracellular R_{7Be}
C_{4Bei} (#/cell)	Intracellular C_{4Be}	C_{7Bei} (#/cell)	Intracellular C_{7Be}
C_{4Beii} (#/cell)	C_{4Bei} after B_e dissociation	R_{7Beii} (#/cell)	R_{7Bei} after B_e dissociation
C_{4Bpii} (#/cell)	C_{4Bpi} after B_p dissociation	C_{7Beii} (#/cell)	C_{7Bei} after trafficking to late endosomes
L_{12i} (#/cell)	Intracellular L_{12}	C_{7Bpii} (#/cell)	C_{7Bpi} after trafficking to late endosomes
		L_{12i} (#/cell)	Intracellular L_{12}

We use the same equation framework and parameters as [10]; however, we do not include any probe-labeled β-arrestin species.

Table A.1c Description and values of CXCR4 kinetic and equilibrium parameters

Parameter	Description	Value[#]	Reported Range[^]
$k_{f,L12,4}$ ($nM^{-1}s^{-1}$)	Forward rate constant of L_{12} binding R_4/R_{4Be}	2.1×10^{-3}	$2.8 - 6.7 \times 10^{-3}$
$k_{f,B,4}$ ($(\#/cell)^{-1}s^{-1}$)	Forward rate constant of B_e binding R_4/C_4	8.5×10^{-9}	$10^{-8} - 10^{-6}$
$K_{D,R4,L12}$ (nM)	Equilibrium dissociation constant of L_{12} binding R_4	40	2-27
$K_{D,R4,B}$ (#/cell)	Equilibrium dissociation constant of B_e from R_4	7.8×10^{6}	$10^{4} - 10^{6}$
$K_{D,C4,B}$ (#/cell)	Equilibrium dissociation constant of B_e from C_4	5.1×10^{6}	$10^{4} - 10^{6}$
$k_{e,R4B}$ (s^{-1})	R_{4Be} internalization rate constant	2.3×10^{-3}	$1 - 2 \times 10^{-3}$
$k_{e,C4B}$ (s^{-1})	C_{4Be} internalization rate constant	4.7×10^{-3}	3×10^{-3}
$k_{off,B,4}$ (s^{-1})	Dissociation rate constant of B_e from C_{4Bei}	7.4×10^{-4}	
$k_{rec,R4Bi}$ (s^{-1})	R_{4Bei} recycling rate constant	3×10^{-4} *	$10^{-4} - 10^{-3}$
$k_{deg,C4Bii}$ (s^{-1})	C_{4Beii} degradation rate constant	1.0×10^{-4}	$10^{-5} - 10^{-4}$
$k_{deg,L12i}$ (s^{-1})	L_{12i} degradation rate constant	1.0×10^{-4}	$10^{-4} - 10^{-3}$

[#] All CXCR4 parameter values are taken from [10] unless otherwise noted.

^ This reported range that was examined in [10] is the same used for sensitivity analysis. When the parameter value is outside the literature range (which happens because it was fit to experimental data), we extend the sensitivity analysis range to that value.

* This value was increased from 6.9×10^{-5} (value in [10]) to 3×10^{-4} (4x increase) to better capture the slow decrease in surface receptor numbers seen in long time frame experiments.

Table A.1d Description and values of CXCR7 kinetic and equilibrium parameters

Parameter	Description	Value[#]	Reported Range[^]
$k_{f,L12,7}$ ($nM^{-1}s^{-1}$)	Forward rate constant of L_{12} binding R_7/R_{7Be}	1.4×10^{-3}	$2.8 – 6.7 \times 10^{-3}$
$k_{f,B,7}$ ($(\#/cell)^{-1}s^{-1}$)	Forward rate constant of B_e binding R_7/C_7	1.4×10^{-8}	$10^{-8} – 10^{-6}$
$K_{D,R7,L12}$ (nM)	Equilibrium dissociation constant of L_{12} binding R_7	0.84	0.2 – 0.4
$K_{D,R7,B}$ (#/cell)	Equilibrium dissociation constant of B_e from R_7	2.3×10^{6}	$10^{4} – 10^{6}$
$K_{D,C7,B}$ (#/cell)	Equilibrium dissociation constant of B_e from C_7	6.5×10^{5}	$10^{4} – 10^{6}$
$k_{e,R7B}$ (s^{-1})	R_{7Be} internalization rate constant	3.9×10^{-3}	$1 – 2 \times 10^{-3}$
$k_{e,C7B}$ (s^{-1})	C_{7Be} internalization rate constant	2.1×10^{-3}	3×10^{-3}
$k_{off,B,7}$ (s^{-1})	Dissociation rate constant of B_e from R_{7Bei}	2.5×10^{-3}	
$k_{e,C7Bi}$ (s^{-1})	Rate constant of trafficking of C_{7Bei} to late endosomes	5.5×10^{-4}	
$k_{rec,R7Bii}$ (s^{-1})	R_{7Beii} recycling rate constant	1.1×10^{-3}	$10^{-4} – 10^{-3}$
$k_{rec,C7Bii}$ (s^{-1})	C_{7Beii} recycling rate constant	2.8×10^{-4}	$10^{-4} – 10^{-3}$
$k_{deg,L12i}$ (s^{-1})	L_{12i} degradation rate constant	1.0×10^{-4}	$10^{-4} – 10^{-3}$

[#] All CXCR7 parameter values are taken from [10].

^ This reported range that was examined in [10] is the same used for sensitivity analysis. When the parameter value is outside the literature range (which happens because it was fit to experimental data), we extend the sensitivity analysis range to that value.

Table A.1e Ordinary differential equations describing events of ligand binding and receptor dynamics

Cellular Event	CXCR4+ cells	CXCR7+ cells
Ligand binding to free receptors	$v_1 = k_{f,L_{12},4}([R_4][L_{12}] - K_{D,R_4,L_{12}}[C_4])$	$v_2 = k_{f,L_{12},7}([R_7][L_{12}] - K_{D,R_7,L_{12}}[C_7])$
Ligand binding to receptor-β-arrestin complexes	$v_3 = k_{f,L_{12},4}([R_{4B_e}][L_{12}] - K_{D,R_{4B},L_{12}}[C_{4B_e}])$	$v_4 = k_{f,L_{12},7}([R_{7B_e}][L_{12}] - K_{D,R_{7B},L_{12}}[C_{7B_e}])$
β-arrestin binding to free receptors	$v_7 = k_{f,B,4}([R_4][B_e] - K_{D,R_4,B}[R_{4B_e}])$	$v_8 = k_{f,B,7}([R_7][B_e] - K_{D,R_7,B}[R_{7B_e}])$
β-arrestin binding to ligand-bound receptors	$v_{11} = k_{f,B,4}([C_4][B_e] - K_{D,C_4,B}[C_{4B_e}])$	$v_{12} = k_{f,B,7}([C_7][B_e] - K_{D,C_7,B}[C_{7B_e}])$
Internalization of cell surface receptor-β-arrestin complexes	$v_{15} = k_{e,R_{4B}}[R_{4B_e}]$	$v_{16} = k_{e,R_{7B}}[R_{7B_e}]$
	$v_{19} = k_{e,C_{4B}}[C_{4B_e}]$	$v_{20} = k_{e,C_{7B}}[C_{7B_e}]$
Dissociation of β-arrestin from internalized receptor-β-arrestin complexes	$v_{23} = k_{off,B,7}[R_{7B_ei}]$	$v_{25} = k_{off,B,4}[C_{4B_ei}]$
Trafficking of internalized receptor-β-arrestin complexes to late endosomes	N/A	$v_{27} = k_{e,C_{7Bi}}[C_{7B_ei}]$
Recycling of internalized receptors	$v_{29} = k_{rec,R_{4Bi}}[R_{4B_ei}]$	$v_{30} = k_{rec,R_{7Bii}}[R_{7B_eii}]$
	N/A	$v_{33} = k_{rec,C_{7Bii}}[C_{7B_eii}]$
Degradation of internalized receptors and ligand	$v_{35} = k_{deg,C_{4Bii}}[C_{4B_eii}]$	
Degradation of L_{12i}	$v_{37} = k_{deg,L_{12i}}[L_{12i}]$	$v_{37} = k_{deg,L_{12i}}[L_{12i}]$

Numbering of equations is consistent with that used in [10].

Table A.1f Ordinary Differential Equations describing the change in the concentration of species in CXCR4+ and CXCR7+ cells over time

CXCR4 Equations (#/cell/s)	CXCR7 Equations (#/cell/s)
$\frac{d[R_4]}{dt} = -v_1 - v_7 - v_9 + v_{29} + v_{31}$	$\frac{d[R_7]}{dt} = -v_2 - v_8 - v_{10} + v_{30} + v_{32} + v_{33} + v_{34}$
$\frac{d[R_{4B_e}]}{dt} = +v_7 - v_3 - v_{15}$	$\frac{d[R_{7B_e}]}{dt} = +v_8 - v_4 - v_{16}$
$\frac{d[C_4]}{dt} = +v_1 - v_{11} - v_{13}$	$\frac{d[C_7]}{dt} = +v_2 - v_{12} - v_{14}$
$\frac{d[C_{4B_e}]}{dt} = +v_3 + v_{11} - v_{19}$	$\frac{d[C_{7B_e}]}{dt} = +v_4 + v_{12} - v_{20}$
$\frac{d[R_{4B_ei}]}{dt} = +v_{15} - v_{29}$	$\frac{d[R_{7B_ei}]}{dt} = +v_{16} - v_{23}$
$\frac{d[C_{4B_ei}]}{dt} = +v_{19} - v_{25}$	$\frac{d[C_{7B_ei}]}{dt} = +v_{20} - v_{27}$
$\frac{d[C_{4B_eii}]}{dt} = +v_{25} - v_{35}$	$\frac{d[C_{7B_eii}]}{dt} = +v_{27} - v_{33}$
$*\frac{d[L_{12}]}{dt} = (-v_1 - v_3 - v_5)\times\frac{n_4\times10^9}{V\times N_{Av}}$	$*\frac{d[L_{12}]}{dt} = (-v_2 - v_4 - v_6)\times\frac{n_7\times10^9}{V\times N_{Av}}$
$\frac{d[L_{12i}]}{dt} = +v_{19} + v_{21} - v_{37}$	$\frac{d[L_{12i}]}{dt} = +v_{20} + v_{22} - v_{37}$
$\frac{d[B_e]}{dt} = -v_7 - v_{11} + v_{15} + v_{25}$	$\frac{d[B_e]}{dt} = -v_8 - v_{12} + v_{23} + v_{33}$
	$\frac{d[R_{7B_eii}]}{dt} = +v_{23} - v_{30}$

*Units for this equation are (nM/s)

N_{AV}:Avogadro's number

Table A.2 Total receptor numbers for the MDA-MB-231 cells transfected to express CXCR4 and CXCR7 used in the device as determined by flow cytometry.

Cell Type	Total receptor number (#/cell)
CXCR4+	$7.1 \times 10^5 \pm 1.0 \times 10^5$
CXCR7+	$5.8 \times 10^6 \pm 6.5 \times 10^5$

Table A.3 Sensitivity Analysis for CXCR4 and CXCR7 molecular parameters

	CXCR4 Average Migration	Average Concentration	Surface CXCR4	Total CXCR4	Surface CXCR7
Ligand binding					
$K_{D,R4,L12}$	---	---	+++		
$K_{D,R7,L12}$		+++	---	---	
β-arrestin binding					
$K_{D,R4,B}$	+++	+++		--	
$K_{D,C4,B}$	++	---	+++	++	
$K_{D,R7,B}$	+++	---	+++	+++	+++
$K_{D,C7,B}$	---	+++	---	---	
Internalization					
$k_{e,R4B}$	---		--		
$k_{e,C4B}$		+++		+++	+
$k_{e,R7B}$		+++	---	---	---
$k_{e,C7B}$		---	+++	+++	
Recycling and Degradation					
$k_{rec,R4Bi}$	+++		+++		
$k_{deg,C4Bii}$					
$k_{off,B,4}$	---	+	---	---	--
$k_{rec,R7Bii}$	++	---	+++	+++	+++
$k_{rec,C7Bii}$					
$k_{offB,7}$		-	++	++	--

Each parameter was varied within the range reported in Supporting Table A4. Sign represents a positive or negative PRCC value. The number of signs represents the significance of the correlation:

+/- : $10^{-5} < p < 10^{-2}$

++/-- : $10^{-12} < p < 10^{-5}$

+++/--- : $p < 10^{-12}$

Appendix A References

1. Cavnar SP, Ray P, Moudgil P, Chang SL, Luker KE, et al. (2014) Microfluidic source-sink model reveals effects of biophysically distinct CXCL12 isoforms in breast cancer chemotaxis. Integr Biol (Camb) 6: 564-576.
2. Torisawa YS, Mosadegh B, Bersano-Begey T, Steele JM, Luker KE, et al. (2010) Microfluidic platform for chemotaxis in gradients formed by CXCL12 source-sink cells. Integr Biol (Camb) 2: 680-686.
3. Lin F, Butcher EC (2006) T cell chemotaxis in a simple microfluidic device. Lab Chip 6: 1462-1469.
4. Bellmann-Sickert K, Beck-Sickinger AG (2011) Palmitoylated SDF1alpha shows increased resistance against proteolytic degradation in liver homogenates. ChemMedChem 6: 193-200.
5. Lambeir AM, Proost P, Durinx C, Bal G, Senten K, et al. (2001) Kinetic investigation of chemokine truncation by CD26/dipeptidyl peptidase IV reveals a striking selectivity within the chemokine family. J Biol Chem 276: 29839-29845.
6. Ray JC, Flynn JL, Kirschner DE (2009) Synergy between individual TNF-dependent functions determines granuloma performance for controlling Mycobacterium tuberculosis infection. J Immunol 182: 3706-3717.
7. Incardona F, Calvo F, Fauvel-Lafeve F, Legrand Y, Legrand C (1993) Involvement of thrombospondin in the adherence of human breast-adenocarcinoma cells: a possible role in the metastatic process. Int J Cancer 55: 471-477.
8. Jacobs AL, Julian J, Sahin AA, Carson DD (1997) Heparin/heparan sulfate interacting protein expression and functions in human breast cancer cells and normal breast epithelia. Cancer Res 57: 5148-5154.
9. Laguri C, Sadir R, Rueda P, Baleux F, Gans P, et al. (2007) The novel CXCL12gamma isoform encodes an unstructured cationic domain which regulates bioactivity and interaction with both glycosaminoglycans and CXCR4. PLoS One 2: e1110.
10. Coggins NL, Trakimas D, Chang SL, Ehrlich A, Ray P, et al. (2014) CXCR7 Controls Competition for Recruitment of beta-Arrestin 2 in Cells Expressing Both CXCR4 and CXCR7. PLoS One 9: e98328.